Multi-sensor, multi-temporal, and ultra-high resolution environmental remote sensing from UAVs

by

Darren James Turner

BSc. Grad Dip (ASOS) (Hons)

(University of Tasmania)

A thesis submitted in fulfilment of the requirements for a Degree of Doctorate of Philosophy at the School of Land and Food, University of Tasmania (February, 2015).

Declaration of Originality

This thesis contains no material which has been accepted for a degree or diploma by the University or any other institution, except by way of background information and duly acknowledged in the thesis, and to the best of my knowledge and belief no material previously published or written by another person except where due acknowledgement is made in the text of the thesis, nor does the thesis contain any material that infringes copyright.

Signed

Darren Turner

Date 27th February 2015

Authority of Access

The publishers of the papers comprising Chapters 2 to 5 hold the copyright for that content, and access to the material should be sought from the respective journals. The remaining non published content of the thesis may be made available for loan and limited copying and communication in accordance with the Copyright Act 1968.

Publications included in this thesis

This thesis contains four manuscripts that have been published in peer reviewed literature and have been incorporated as Chapters 2-5.

Publication citation – incorporated as Chapter 2.

Turner, D., A. Lucieer, C. Watson (2012). "An Automated Technique for Generating Georectified Mosaics from Ultra-High Resolution Unmanned Aerial Vehicle (UAV) Imagery, Based on Structure from Motion (SfM) Point Clouds." Remote Sensing **4**(5): 1392-1410

Declaration of co-authorship

	Dr Arko Lucieer	**Dr Christopher Watson**
Declaration regarding specific elements	**Extent (1,2,3)**	**Extent (1,2,3)**
1. Formulation/identification of the scientific problem that need to be clarified. This includes a condensation of the problem to specific scientific questions that is judged to be answerable via experiments	2	1
2. Planning of the experiments and methodology design, including selection of	2	1
3. Involvement in the experimental work	2	0
4. Presentation, interpretation and discussion in a journal format of the obtained data	2	1
Overall Contribution	**2**	**1**

Evaluation scale:
1 – has contributed to this work (10-33%)
2 – has made substantial contribution to this work (34-66%)
3 – has made a major contribution to this work (67-100%)

Signed by Co-authors

Dr Arko Lucieer **Dr Christopher Watson**

Publication citation – incorporated as Chapter 3.

Turner, D., A. Lucieer and L. Wallace (2014). "Direct Georeferencing of Ultrahigh-Resolution UAV Imagery." IEEE Transactions on Geoscience and Remote Sensing **52**(5): 2738-2745.

Declaration of co-authorship

	Dr Arko Lucieer	**Dr Luke Wallace**
Declaration regarding specific elements	**Extent (1,2,3)**	**Extent (1,2,3)**
1. Formulation/identification of the scientific problem that need to be clarified. This includes a condensation of the problem to specific scientific questions that is judged to be answerable via experiments	1	1
2. Planning of the experiments and methodology design, including selection of	1	1
3. Involvement in the experimental work	1	1
4. Presentation, interpretation and discussion in a journal format of the obtained data	1	1
Overall Contribution	**1**	**1**

Evaluation scale:
1 – has contributed to this work (10-33%)
2 – has made substantial contribution to this work (34-66%)
3 – has made a major contribution to this work (67-100%)

Signed by Co-authors

Dr Arko Lucieer **Dr Luke Wallace**

Publication citation – incorporated as Chapter 4.

Turner, D., A. Lucieer, Z. Malenovský, D. King and S. Robinson (2014). "Spatial Co-Registration of Ultra-High Resolution Visible, Multispectral and Thermal Images Acquired with a Micro-UAV over Antarctic Moss Beds." Remote Sensing **6**(5): 4003-4024.

Declaration of co-authorship

	Dr Arko Lucieer	**Dr Zbyněk Malenovský**
Declaration regarding specific elements	**Extent (1,2,3)**	**Extent (1,2,3)**
1. Formulation/identification of the scientific problem that need to be clarified. This includes a condensation of the problem to specific scientific questions that is judged to be answerable via experiments	2	1
2. Planning of the experiments and methodology design, including selection of	1	1
3. Involvement in the experimental work	1	1
4. Presentation, interpretation and discussion in a journal format of the obtained data	1	1
Overall Contribution	**1**	**1**

	Diana H. King	**Dr Sharon A. Robinson**
Declaration regarding specific elements	**Extent (1,2,3)**	**Extent (1,2,3)**
1. Formulation/identification of the scientific problem that need to be clarified. This includes a condensation of the problem to specific scientific questions that is judged to be answerable via experiments	0	0
2. Planning of the experiments and methodology design, including selection of	0	0
3. Involvement in the experimental work	1	0
4. Presentation, interpretation and discussion in a journal format of the obtained data	1	1
Overall Contribution	**1**	**1**

Evaluation scale:
1 – has contributed to this work (10-33%)
2 – has made substantial contribution to this work (34-66%)
3 – has made a major contribution to this work (67-100%)

Signed by Co-authors

Dr Arko Lucieer **Dr Zbyněk Malenovský**

Diana H. King **Dr Sharon A. Robinson**

Publication citation – incorporated as Chapter 5.

Turner, D., A. Lucieer and S. M. de Jong (2015). "Time Series Analysis of Landslide Dynamics Using an Unmanned Aerial Vehicle (UAV)." Remote Sensing **7**(2): 1736-1757.

Declaration of co-authorship

	Dr Arko Lucieer	**Dr Steven de Jong**
Declaration regarding specific elements	**Extent (1,2,3)**	**Extent (1,2,3)**
1. Formulation/identification of the scientific problem that need to be clarified. This includes a condensation of the problem to specific scientific questions that is judged to be answerable via experiments	1	0
2. Planning of the experiments and methodology design, including selection of	1	1
3. Involvement in the experimental work	1	1
4. Presentation, interpretation and discussion in a journal format of the obtained data	1	0
Overall Contribution	**1**	**1**

Evaluation scale:
1 – has contributed to this work (10-33%)
2 – has made substantial contribution to this work (34-66%)
3 – has made a major contribution to this work (67-100%)

Signed by Co-authors

Dr Arko Lucieer **Dr Steven de Jong**

Other published material:

A number of other works were published during the preparation of this thesis, but with the exception of relevant citation, they have not been incorporated into the thesis:

Conference papers

Lucieer, A., Robinson, S., Turner, D., Harwin, S., and Kelcey, J. (2012). Using a micro-UAV for ultra-high resolution multi-sensor observations of Antarctic moss beds. ISPRS - International Archives of the Photogrammetry, Remote Sensing and Spatial Information Sciences (Vol. XXXIX-B1, pp. 429–433). doi:10.5194/isprsarchives-XXXIX-B1-429-2012

Turner, D., A. Lucieer and C. Watson (2011). Development of an Unmanned Aerial Vehicle (UAV) for hyper resolution vineyard mapping based on visible, multispectral, and thermal imagery. 34th International Symposium for Remote Sensing of the Environment (ISRSE), Sydney Australia.

Lucieer, A., S. Robinson and D. Turner (2011). Unmanned Aerial Vehicle (UAV) Remote Sensing for Hyperspatial Terrain Mapping of Antarctic Moss Beds based on Structure from Motion (SfM) point clouds. 34th International Symposium for Remote Sensing of the Environment (ISRSE), Sydney Australia.

Turner, D. and A. Lucieer (2013). Using a Micro Unmanned Aerial Vehicle (UAV) for Ultra High Resolution Mapping and Monitoring of Landslide Dynamics. IEEE International Geoscience and Remote Sensing Symposium. Melbourne, Australia.

Wallace, L., Lucieer, A., Turner, D., and Watson, C. (2011). Error assessment and mitigation for hyper-temporal UAV-borne LiDAR surveys of forest inventory. In Proceedings of Silvilaser 2011. Hobart, Australia.

Journal Articles

Lucieer, A., S. deJong and D. Turner (2013). "Mapping landslide displacements using Structure from Motion (SfM) and image correlation of multi-temporal UAV photography." Progress in Physical Geography: 1-20.

Lucieer, A., D. Turner, D. H. King and S. A. Robinson (2014). "Using an Unmanned Aerial Vehicle (UAV) to capture micro-topography of Antarctic moss beds." International Journal of Applied Earth Observation and Geoinformation **27**(April): 53-62.

Wallace, L., A. Lucieer, C. Watson, and D. Turner (2012). " Development of a UAV LiDAR System with Application to Forest Inventory. " Remote Sensing **4** (6), pp. 1519–1543.

Bemis, S. P., S. Micklethwaite, D. Turner, M. R. James, S. Akciz, S. T. Thiele and H. A. Bangash (2014). "Ground-based and UAV-Based photogrammetry: A multi-scale, high-resolution mapping tool for structural geology and paleoseismology." Journal of Structural Geology **69, Part A**(0): 163-178.

Abstract

Civilian use of Unmanned Aerial Vehicles (UAVs) has become increasingly common in recent times. Improvements in airframe design and electronics, particularly the mass production of comparatively inexpensive miniaturised inertial and positioning sensors, has enabled the application of UAVs to many and varied tasks. One area of growth in the scientific community has been the use of UAVs for Environmental Remote Sensing (ERS) where high spatial and temporal resolution, the ability to fly on-demand, and data collection from multiple sensors offers substantial advantages over traditional techniques.

For small regions, Micro-UAVs (MUAVs), typically weighing less than 5 kg with flying duration of up to 30 minutes, present an excellent option for collecting the required remotely sensed data for understanding environmental processes that require high resolution (centimetre scale), multi-sensor data. There are, however, several important issues to be considered and further developed. The high resolution images have a small footprint and in most cases, hundreds of overlapping images are required to span the region of interest. These images often contain high perspective distortions (compared to traditional nadir aerial photography) and thus can be difficult to process with conventional techniques and software. For most applications, it is important that the imagery is accurately georeferenced, which is typically undertaken using Ground Control Points (GCPs). Collection of GCPs can be a time-consuming process and detracts from one of the advantages of an MUAV, which is operational flexibility and efficiency. In addition, to acquire multi-sensor datasets, an MUAV will need to carry each of the multiple sensors on separate flights, which means the image datasets from each of these flights need to be accurately co-registered. Finally, if repeat coverage is required over time, data collection and processing methods must be robust and repeatable.

This thesis sets out to address these barriers, particularly those associated with processing high resolution imagery collected with multiple sensors. The broad aim of this study is to determine appropriate workflows to enable the efficient, timely, and accurate processing of multi-sensor data collected from an MUAV. Case studies are

used to demonstrate how specific challenges are addressed and to quantify the accuracy achieved in the context of various environmental monitoring applications.

A methodology to geometrically correct and mosaic UAV imagery using feature matching and Structure from Motion (SfM) photogrammetric techniques was developed. This technique is fully automated and can georectify and mosaic imagery based either on GCPs (achieving an accuracy of 10 – 15 cm) or via a Direct Georeferencing (DG) technique (with an accuracy of 65–120 cm when using the navigation-grade on-board GPS). The DG system, which used the location of the camera at time of exposure as the basis for georeferencing, was limited by the accuracy of the GPS used to measure airframe position (generally a navigation-grade receiver) and the accuracy of the synchronisation between time of exposure and the GPS position record. A camera-GPS module was developed that incorporated a higher accuracy GPS (single frequency carrier phase based unit with an accuracy of 10 – 20 cm) and a camera synchronisation system. Commercial software was used to process and directly georeference the imagery and achieve an absolute spatial accuracy of 11 cm, which is commensurate with the accuracy of the GPS unit used.

A case study that investigated the physiological state of Antarctic moss ecosystems was used to demonstrate that data from multiple sensors can be accurately co-registered. Imagery from each sensor was georeferenced and mosaicked with a combination of commercially available software and custom routines that were based on the Scale Invariant Feature Transform (SIFT) and SfM workflow. The spatial co-registration of the mosaics was measured and found to have a mean root mean squared error (RMSE) of 1.78 pixels. This study also demonstrated that quantitative data can be collected with specialised sensors and then related to plant traits. In particular, the Modified Triangular Vegetation Index (MTVI) was derived from the multispectral data and related to the health of moss quadrats (as measured in-situ) and a statistically significant ($R^2 = 0.64$) relationship was found.

The ability of MUAVs to be used for time series analysis was demonstrated with a case study of a highly dynamic landslide that was monitored from 2010 through to 2014 with seven separate datasets collected during the period. Software based on SfM algorithms was used to create Digital Surface Models (DSMs) of the landslide surface with an accuracy of around 4 – 5 cm in the horizontal and 3 – 4 cm in the

vertical. The accuracy of the co-registration of subsequent DSMs was checked and corrected based on comparing non-active areas of the landslide, which minimised alignment errors to a mean of 7 cm. It was discovered that the methodology could also be applied to historical aerial photography to create a baseline DSM allowing the total displacement of the landslide to be calculated (approximately 6630 $m^{3)}$. This study demonstrated that MUAVs can be used repeatedly to map the dynamics of a landslide over a period of 4 years.

Addressing the issues presented throughout this thesis demonstrates the clear potential of MUAVs for a wide range of applications within the broad discipline of Environmental Remote Sensing. It was also shown that MUAVs offer a series of benefits such as high spatial and temporal resolutions along with the ability to collect multi-sensor data. Ongoing technological developments, particularly in sensor miniaturisation, high capacity power storage, autopilot reliability, and motor design will likely continue the present upward trajectory of MUAV use across the diverse user communities.

Acknowledgments

Thanks go to my supervisors Arko Lucieer and Christopher Watson. I warned Arko at the start that my writing would need some work to bring it up to scratch, I hope that at least the latter stages were not too painful. Thanks to Chris for providing an "outside" perspective and particularly for the help to bash the Introduction and Conclusion chapters into shape. Also thanks to both supervisors for their academic guidance throughout the whole process.

Appreciation must also be given to the co-authors of the four papers presented in this thesis : Arko Lucieer, Christopher Watson, Luke Wallace, Dianne King, Sharon Robinson, Zbyněk Malenovský, and Steven de Jong. It was great to work with you and to get each of the papers published with relative ease and I believe this reflects the quality of all your valuable contributions, many thanks.

The Terraluma research team has provided an exciting and interesting group in which to work. Stephen Harwin is thanked particularly for his help with fieldwork, Luke Wallace and Josh Kelcey for their assistance with various image processing algorithms. The team is current undergoing a "changing of the guard", but I look forward to working with Terraluma into the exciting future that UAV remote sensing holds.

The team of scientists and support staff that helped out during the Antarctic research season at Casey in 2011 are also to be thanked. The data collected on this trip provided the basis for two of the papers and would not have been possible without their assistance. It was fantastic to be able to work in such an amazing place.

The owners of the Homehill vineyard are thanked for allowing access to their property on a regular basis to survey the Homehill landslide. Similarly the owners of Houstons farm are thanked for allowing access to their lettuce crops.

The staff at the former School of Geography and Environmental Studies, now the School of Land and Food, are thanked for their support. Elaine Stratford is one to be thanked in particular. At the commencement of my PhD she was Head of School and allowed me time from my job in the School to undertake a part time PhD. Without her early support I never would have been able to start this degree. Thanks also go to the professional staff in the School, not just for their normal roles in supporting a PhD student but for being understanding and "covering for me" when I had to spend time on fieldwork etc. In particular, I am indebted to Paulene Harrowby, Rob Anders, Trish McKay, Dave Green, and Phoebe Banks.

My parents are to be thanked for all their love and support over the years.

Finally and most importantly, thank you to my beautiful wife and four children. I hope this PhD has not got in the way too much, it is over now! One thing I did learn was how to write a paper with kids shouting and making noise in the background. But most importantly, without the support and encouragement of my wife Perpetua, this would never have been possible, thank you my love.

Table of Contents

Declaration of Originality iii
Authority of Access iii
Publications included in this thesis iv
Abstract xi
Acknowledgments xiv
List of Tables and Figures xx
Chapter 1 Introduction 1
1.1 Unmanned Aerial Vehicles 1
1.1.1 Background 1
1.1.2 Definition 1
1.1.3 Types, Classifications and Platforms 2
1.1.4 Recent trends in UAV utilisation 5
1.2 Advantages of MUAVs 7
1.2.1 Spatial resolution 7
1.2.2 Temporal resolution 8
1.2.3 Costs 9
1.2.4 Other advantages 10
1.3 Limitations of MUAVs 10
1.3.1 Coverage 10
1.3.2 Sensor quality 11
1.3.3 Regulations 12
1.4 Problem statement 13
1.5 Research Objectives 15
1.6 Thesis Structure 16
Chapter 2 An Automated Technique for Generating Georectified Mosaics from Ultra-High Resolution Unmanned Aerial Vehicle (UAV) Imagery, Based on Structure from Motion (SfM) Point Clouds 19
Abstract 19
2.1 Introduction 20
2.2 Methodology 26
2.2.1 UAV Platform and Photo Acquisition 26
2.2.2 Block adjustment and Point Cloud Generation 27
2.2.3 3D Point Cloud Transformation Using Direct Technique 29
2.2.4 3D Point Cloud Transformation Using GCP Technique 30

2.2.5 Rectification of the Images 32
2.2.6 Mosaicking 33
2.3 Results and Discussion 33
2.3.1 Study Area and Dataset 33
2.3.2 Helmert Transformation Parameters 36
2.3.3 Mosaics 38
2.3.4 Spatial Accuracy 39
2.4 Conclusions 42
2.5 Thesis Context 43
Chapter 3 Direct Georeferencing of Ultra-high Resolution UAV Imagery 45
Abstract 45
3.1 Introduction 46
3.2 Methodology 48
3.2.1 Platform 48
3.2.2 GPS logging system with camera sync 49
3.2.3 Automated image selection 51
3.2.4 Image processing 53
3.3 Results 55
3.3.1 Study Area used for testing 55
3.3.2 Processing time 56
3.3.3 Spatial Accuracy 58
3.3.4 Helmert transformations 60
3.4 Discussion 61
3.5 Conclusions 64
3.6 Thesis Context 64
Chapter 4 Spatial Co-Registration of Ultra-High Resolution Visible, Multispectral and Thermal Images Acquired with a Micro-UAV over Antarctic Moss Beds Co-registration 65
Abstract 65
4.1 Introduction 66
4.2 Material and Methods 69
4.2.1 Test Sites 69
4.2.2 Platform 70
4.2.3 Visible Digital Camera 71
4.2.4 Thermal Infrared Sensor 71
4.2.5 Multispectral Sensor 73

4.2.6 Mosaicking of Visible Imagery 74
4.2.7 Mosaicking of Thermal Infrared Images 75
4.2.8 Mosaicking of Multispectral Images 77
4.2.9 Calculating MTVI2 from Multispectral Data 79
4.2.10 Accuracy Assessment 81
4.3 Results 81
4.3.1 Image Mosaics 81
4.3.2 Co-Registration Accuracy 84
4.3.3 Assessing Health of Antarctic Moss from Multisprectral Imagery 85
4.3.4 Assessing Temperature of Healthy Moss from Thermal Infrared Image Mosaic 87
4.4 Discussion 88
4.5 Conclusions 90
4.6 Thesis Context 91
Chapter 5 Time series analysis of landslide dynamics using an Unmanned Aerial Vehicle (UAV) 93
Abstract 93
5.1 Introduction 94
5.2 Methods 97
5.2.1 Platform 97
5.2.2 Sensor 98
5.2.3 Field Site 98
5.2.4 Three dimensional model generation 100
5.2.5 Alignment of Digital Surface Models 101
5.2.6 Measurement of landslide area and volume change 103
5.2.7 Tracking of landslide surface movement 103
5.3 Results 104
5.3.1 Accuracy of DSMs and orthophotos 104
5.3.2 Area and slope analysis 105
5.3.3 DSM volumetric changes 107
5.3.4 Historical DSM 109
5.3.5 Surface movement 111
5.3.6 Comparison of landslide movement with rainfall 114
5.4 Discussion 115
5.5 Conclusions 117

5.6 Thesis Context 118
Chapter 6 Conclusions 119
6.1 Ortho-mosaic creation 119
6.2 Direct georeferencing of UAV imagery 120
6.3 Co-registration of multi sensor data 121
6.4 Multi-temporal studies 123
6.5 Contributions to knowledge 125
6.6 Limitations and future research directions 125
6.7 Final remarks 127
References 128

List of Tables and Figures

Table 1.1 - UAV categories as defined by UVS-international (Unmanned Vehicle Systems) (Eisenbeiss, 2004) 2

Table 1.2 - Specification of the two Oktokopters used in this study..... 5

Table 2.1 - Comparison of Bundle Block Adjustment variables. 24

Table 2.2 - Sample point pairs list..... 30

Table 2.3 - Example list of GCPs for an image..... 32

Table 2.4 - Helmert transformation parameters with formal errors (1 sigma) from least squares solution. 37

Table 2.5 - Summary of mosaics and their spatial accuracy 40

Table 3.1 - Summary of total processing time for 143 images with each method..... 57

Table 3.2 - Summary of spatial errors for each method 59

Table 3.3 - Helmert transformation parameters with formal errors (1 sigma) from least squares solution..... 61

Table 4.1 - Details of acquired image datasets collected at each test site. 82

Table 4.2 - Spatial accuracy of orthomosaics for each sensor as measured against check points. 84

Table 4.3 - Co-registration accuracy of mini-Multi Camera Array (mini-MCA) and Thermal Infrared (TIR) mosaics as compared to the visible mosaic. 84

Table 5.1 - Details of aerial surveys of Home Hill landslide 100

Table 5.2 - Evaluation of relative elevation accuracy for each pair of DSMs before and after offsets were applied, differences between the DSMs were measured over 4,578,868 pixels (1830 m^2) outside the active landslide area. 103

Table 5.3 - Summary of spatial errors for Home Hill landslide DSMs and orthophotos..... 105

Table 5.4 - Changes in area and leading edge slope of Home Hill landslide..... 107

Table 5.5 - Volumetric changes in m^3 for the small toe of Home Hill landslide, including estimated errors at one sigma, also reported is the bulking factor, the ratio of accumulated material to lost material..... 107

Figure 1.1 - The two Oktokopters used in this study : (a) Mikrokopter Oktokopter airframe, (b) Droidworx AD-Heavy Lift airframe..... 4

Figure 1.2 - Number of UAV publications per year (excluding robotics and engineering fields of research), source Scopus (2015) 7

Figure 1.3 - Structure of thesis and achievement of objectives..... 17

Figure 2.1 - Oktokopter fitted with Canon 550D 26

Figure 2.2 - Software to plan flight over Antarctic moss bed 27

Figure 2.3 - (a) The continent of Antarctica with an arrow in Eastern Antarctica indicating the location of the Windmill Islands (b) The locations of the Robinson Ridge and Red Shed study sites in the Windmill Islands 34

Figure 2.4 - Moss bed area at the Robinson Ridge site with a variety of healthy moss (green), stressed moss (red/brown), and dead moss (black). Small orange discs (~10 cm diameter) and trays (~30 cm diameter) used as GCPs for geometric correction and validation are visible in the photograph 36

Figure 2.5 - Example of 2888 of control points (shown in red—extracted from the process described in Section 2.2.5) on a single photograph 38

Figure 2.6 - Detailed section of a typical region within the image mosaic of Robinson's Ridge highlighting accuracy of seam lines (yellow box highlights seam line). 39

Figure 2.7 - Detailed section of an image mosaic of Robinson's Ridge showing typical spatial errors of direct and GCP techniques in relation to the actual GCPs (the small orange discs)..... 41

Figure 3.1 - Oktokopter in flight with Canon™ 550D fitted. 49

Figure 3.2 - Image capture and position determination system. Based on: Camera with synchronisation adapter, GPS with data logging board, battery, and GPS antenna. 50

Figure 3.3 - Mosaic of study site with location map and UAV flight path overlaid (coordinate system: GDA94 UTM55S). 56

Figure 3.4 - Close up of one GCP showing the spatial error for each method (coordinate system: GDA94 UTM55S). 59

Figure 3.5 - Estimated focal length and Z Translation residual errors for Bundler processing method..... 62

Figure 4.1 - Site location map for the three Antarctic test sites 70

Figure 4.2 - Oktokopter fitted with FLIR Photon 320 Thermal Infrared camera with Ethernet module mounted below. 71

Figure 4.3 - Comparison of two consecutive TIR frames;
(a) blurry image with blur index of 0.32, and
(b) sharp image with blur index of 0.22. 76

Figure 4.4 - Robinson Ridge study site: (a) visible mosaic of entire area, (b) RGB image subset, (c) multispectral image subset, (d) thermal infrared image subset, and (e) typical multi-spectral reflectance function of a healthy Antarctic moss turf. 83

Figure 4.5 - Statistical relationship between the ground-measured moss health and the MTVI2 index computed from mosaic of multispectral mini-MCA images obtained at Robinson Ridge test site 86

Figure 4.6 - Spatially co-registered thematic maps; (a) Overview; (b) Moss health derived from MTVI2 vegetation index and (c) Moss surface temperature at ultra-high spatial resolution (a red circle highlights thermal shadow cast by a large boulder). 87

Figure 4.7 - Statistical relationship between thermal infrared DN values from UAV imagery and ground measured surface temperature for 19 sample points at the Robinson Ridge test site. 88

Figure 5.1 - Oktokopter in flight, fitted with Canon 550D camera 98

Figure 5.2 - December 2011 ortho-mosaic of Homehill landslide area highlighting the main features. (a) location map, (b) example of GCP with actual location marked with a black cross giving a typical example of absolute spatial errors (coordinate system: GDA94 UTM55S) 99

Figure 5.3 - Transects through leading edge of the large toe 106

Figure 5.4 - 2012A to 2013A DSM change,
(a) area of scarp collapse, (b) areas of toe advance
(coordinate system: GDA94 UTM55S). 109

Figure 5.5 - 3D model of the Home Hill landslide as constructed from 1984 aerial photography. The landslide area is circled in red. 110

Figure 5.6 - Cosi-Corr surface movement maps; a) 2011B - 2012A, b) 2012A - 2013A, c) 2013A - 2013B, and d) 2013B - 2014A (coordinate system: GDA94 UTM55S). 112

Figure 5.7 - Comparison of annual rate of rainfall and annual rate of accumulation of material for the little toe area of the Home Hill landslide 114

Chapter 1 Introduction

1.1 Unmanned Aerial Vehicles

1.1.1 Background

In the past, Unmanned Aerial Vehicles, (UAVs) have primarily been used in the military domain. With the increased availability of low-cost and lightweight Global Positioning System (GPS) receivers, Inertial Measurement Units (IMUs), digital cameras, and autopilot systems, the civilian use of UAVs has increased dramatically in recent times (Nebiker *et al.*, 2008; Zhou *et al.*, 2009). In particular, the use of UAVs for photogrammetry and remote sensing presents many new and exciting opportunities (Colomina and Molina, 2014). The collection of ultra-high resolution data (~1 cm / pixel) with centimetre level accuracy is one area in which small UAVs offer the greatest potential (Colomina and Molina, 2014; Anderson and Gaston, 2013). UAVs have a high level of operational flexibility, enabling data to be collected with a high temporal resolution. For environmental applications such as monitoring vegetation change, the re-visit time of satellites is often insufficient (Berni *et al.*, 2009), providing a niche opportunity for UAVs. The development of UAV airframe technology has delivered a wider selection of miniature optical sensors (such as multispectral and thermal infrared) that can be carried by UAVs. Also, there are now many low-cost UAVs based on affordable and readily available remote controlled aircraft, thus UAV surveys can potentially be more economical than traditional field-based surveys and/or commercial airborne/satellite based acquisitions. Anderson and Gaston (2013) identified the many and varied areas of research that UAV imagery could be applied to, such as ecology, vegetation dynamics, and ecosystems.

1.1.2 Definition

The acronyms UAV (Unmanned Aerial Vehicle), UAS (Unmanned Aerial System) and RPV (Remotely Piloted Vehicle) each refer to similar but subtly different systems. An RPV implies that the vehicle is remotely piloted during flight by an appropriately skilled operator. However, a UAV is conventionally thought of as being a truly “unmanned” aircraft in that no skilled operator is required in the air or

on the ground, implying that the system is highly autonomous. The term UAS refers to the entire "system", including ground control station, sensors, and communication systems, rather than just the airborne platform.

In Australia, the legal definition of a UAV or UAS is defined in "Civil Aviation Safety Regulation 101 – Unmanned aircraft and rocket operations" (CASA, 2014). The difference between a UAV and a Radio Controlled (RC) aircraft is not defined by any characteristic of the airframe, but rather by its use. Once an unmanned aircraft is no longer used solely for recreational purposes and is operated for commercial gain, it is then legally considered by the Civil Aviation Safety Authority (CASA) to be a UAV (CASA, 2014). At the time of writing this thesis, CASA do not have a category to cover the use of UAVs for research purposes. Thus, the same rules that govern commercial operations also apply to scientific research UAV flights.

1.1.3 Types, Classifications and Platforms

UAVs vary in size from extremely small micro-UAVs usually designed to fly indoors, up to what would be considered a full-size aircraft, such as the United States' military weaponised Predator UAV that can seek out and destroy ground and air based targets. Some mid-sized UAVs such as the Aerosonde (www.aerosonde.com) can fly to high levels (e.g. 6 km) of the atmosphere with flight durations of up to 30 hours. These UAVs are known as High Altitude Long Endurance (HALE) UAVs. Based on size and function, UAVs can therefore be classified into various categories (see Table 1.1).

Table 1.1 – UAV categories as defined by UVS-international (Unmanned Vehicle Systems) (Eisenbeiss, 2004)

Category name	Mass (kg)	Range (km)	Flight Altitude (m)	Endurance (hours)
Micro	<5	<10	250	1
Mini	<25	<10	300	<2
Close Range	25-150	10-30	3000	2-4
Medium Range	50-250	30-70	3000	3-6
HALE	>250	>70	>3000	>6

Long duration flights are typically carried out at higher altitudes and designed to collect data over a large area. In this study, the focus is on the improved utilisation of UAVs for environmental remote sensing. Applications across this discipline are sometimes characterised by the requirement for sub-decimetre resolution data collected over small sample areas (< 10 ha), for which micro-UAVs are most suitable.

When choosing a UAV platform for high resolution remote sensing there are a number of considerations to be made. It is important that the UAV is relatively easy to fly and capable of flying low and slow (Hardin and Jensen, 2011). At this time there are few UAVs on the market that have been optimised for scientific purposes such as environmental mapping (Hardin and Jensen, 2011). A common problem for civilian UAV users is that many UAV manufacturers continue to primarily market UAVs that have been designed for the military sector (Rango *et al.*, 2009).

When it comes to the choice between fixed wing UAVs and Vertical Take Off and Landing (VTOL) UAVs there are more differences to be considered than just their modes of flight. A fixed wing aircraft travels faster than a VTOL aircraft and thus can cover a larger area in the same amount of time, however, to maintain a sufficient image overlap the fixed wing needs to fly higher such that the footprint and thus the overlap is larger. As a VTOL UAV can capture images at virtually any overlap, it is possible to fly very low and capture extremely high resolution data if required. Fixed wing platforms can also have issues with image overlap if wind causes the UAV to deviate too far from the desired flight path (Hardin and Jensen, 2011). Tail winds can result in excessive ground speed and hence it can become difficult for the image capture system to maintain sufficient forward overlap. In addition, motion blur can become an issue. VTOL aircraft can fly at effectively any groundspeed required regardless of wind direction (within reason) and hence do not suffer as much from overlap and motion blur issues.

It is possible to purchase conventional airframes based on RC model kits, be it fixed wing or VTOL, and then install an autopilot. This can be a time-consuming process due to difficulties in tuning autopilot parameters for stable flight behaviour (Hardin and Jensen, 2011). This study is primarily focused on mapping smaller areas

(< 10 ha) at an ultra-high resolution (~1 cm / pixel) with a high level of image overlap. Thus a VTOL Micro-UAV (MUAV) was deemed to be most suitable. Two multi-rotor "OktoKopters" (see Figure 1.1) that use autopilot systems developed by Mikrokopter (www.mikrokopter.com) were chosen (see Table 1.2 for specifications). They are relatively straightforward to operate, requiring only a small flat area from which to take off and land, and they come with their own pre-configured and reliable autopilots.

(a)

(b)

Figure 1.1 – The two Oktokopters used in this study : (a) Mikrokopter Oktokopter airframe, (b) Droidworx AD-Heavy Lift airframe

Table 1.2 – Specification of the two Oktokopters used in this study

Specification	Mikrokopter Oktokopter	Droidworx Oktokopter
Payload	1.2 kg max	2.0 kg max
Flight time	5 minutes	5 minutes
Construction	Aluminium tube	Carbon Fibre
Propeller size	10 inch diameter 2.7 inch pitch	12 inch diameter 3.8 inch pitch
Camera mount	Photoship One MKTR Professional	Photohigher AV130
Autopilot	Mikrokopter Flight-Ctrl 2.0, Navi-Ctrl 2,0, and MKGPS 2.0	Mikrokopter Flight-Ctrl 2.0, Navi-Ctrl 2,0, and MKGPS 2.0

1.1.4 Recent trends in UAV utilisation

UAVs have been in use since the dawn of aviation (Wong and Bil, 2006; Colomina and Molina, 2014). Some of the earliest civilian experiments with RC-based UAVs were undertaken in 1979 (Eisenbeiss, 2004). However, UAVs have been predominantly used by the military for such purposes as reconnaissance, target practice, and seek and destroy missions (Everaerts, 2008). This military focus has resulted in the UAV industry being driven primarily by military funding and hence the technology developments have not been focused on civilian applications such as mapping and environmental monitoring (Horcher and Visser, 2004). In addition, much of the developed military UAV technology requires stringent standards and is therefore costly (Wong, 2001). Finally, military operations are usually mission centric where safety and retrieval are not the main focus, such that the platform is often considered expendable (Marchbank, 2009a).

The potential to collect imagery from UAVs was realised as early as the 1980's, however, airframe vibrations and lack of compact and accurate GPS/INS hardware limited the development (Eisenbeiss, 2004). As recently as 1998 it was still thought that the technology was not yet sufficiently advanced for the civilian market to be developed (Wong, 2001). However, since the start of the 21st century there have been a number of developments that have enabled the viability of the civilian market. The

weight, physical size, and cost of sensors and electronic components have all decreased allowing smaller and cheaper UAV airframes to be able to carry a functional payload (Berni *et al.*, 2009; Horcher and Visser, 2004). The miniaturisation of sensors, such as accelerometers and gyroscopes as found in personal devices like smart phones, has provided the technology on which the miniature autopilots are based. Autonomous capabilities of UAV control systems (autopilots) are now mature enough and economically viable for widespread use (Wong and Bil, 2006).

Worldwide the use of civilian UAVs is increasing while the military share of the market is stabilising (Wong and Bil, 2006). In 2010, it was estimated that the civilian UAV industry in Australia was worth AUD$20 million and employed 150 people (Wilson, 2010). However, civilian activities are still limited, partly due to a lack of confidence and investment in unproven technology (Wong, 2001). Aviation regulations governing the use of UAVs are also seen by some as a hindrance to the uptake of civilian UAV use, particularly in places like the USA where obtaining a permit to fly can be difficult (Rango and Laliberte, 2010). As the potential cost savings of UAVs become apparent, the commercial push from industry is likely to pick up the pace of development (Marchbank, 2009a). There is also a growing public acceptance of UAVs and their usefulness, but this acceptance is vulnerable to activities conducted by unlicensed hobbyist operators that could affect market confidence (Marchbank, 2009b).

The last decade has seen a huge increase in the commercial production and use of UAVs for civilian purposes. For example, in Japan UAVs are widely used for application of pesticides and herbicides in rice crops, which has created an industry worth US$100 million per annum (Everaerts, 2008). In Australia, the number of licensed operators has gone from around 10 in 2009 to nearly 200 in early 2015 (CASA, 2015). One of the most common civilian commercial uses for UAVs is aerial photography of real-estate and other similar areas such as aerial inspections of building sites and proposed developments, as well as airborne videography. A simple search of a publication database reveals that since the year 2000 the use of UAVs for remote sensing type applications has become more popular within the scientific community (see Figure 1.2).

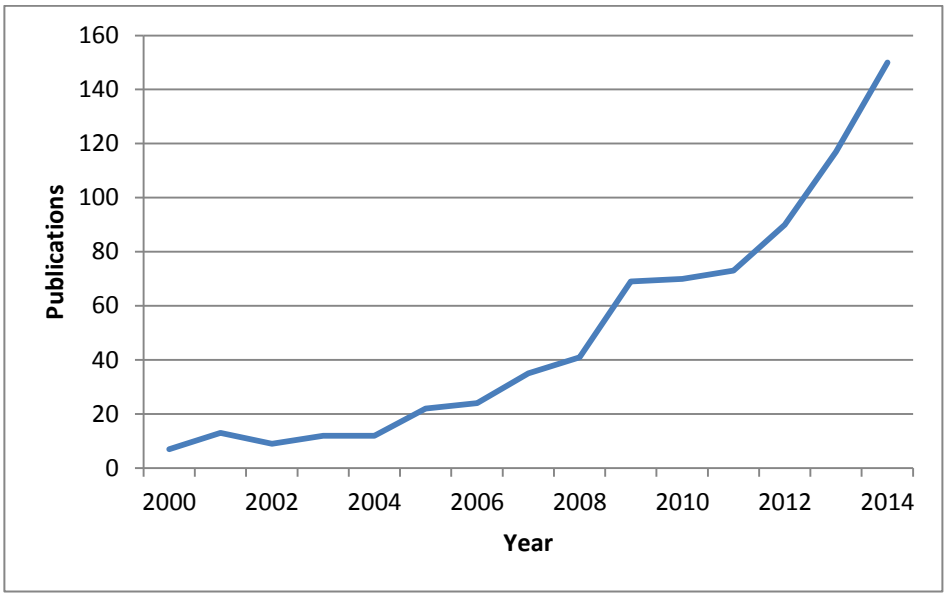

Figure 1.2 - Number of UAV publications per year (excluding robotics and engineering fields of research), source Scopus (2015)

1.2 Advantages of MUAVs

In the context of environmental remote sensing applications for which high resolution data is required, a number of clear advantages and limitations of micro UAVs emerge.

1.2.1 Spatial resolution

The spatial resolution obtainable from an MUAV is much higher compared to conventional remote sensing platforms, such as satellites and manned aircraft. Typically, the highest spatial resolution available from commercial satellite sensors is 50 - 60 cm / pixel (Digitalglobe, 2011) and from aerial photography platforms the best available resolution commonly available is 15 - 25 cm / pixel (Nebiker *et al.*, 2008). MUAVs are typically flown at lower altitudes than manned aircraft, thus increasing the spatial resolution of the data collected (Hunt *et al.*, 2010b; Scaioni *et al.*, 2009). MUAVs can collect imagery at sub-decimetre resolution, even as detailed as 1 cm / pixel. Rango *et al* (2009) proposed the term "hyperspatial" resolution for when the spatial resolution of the imagery collected is finer than the object of interest. Hyperspatial data enables the

production of maps similar detail to a ground survey but over a much larger area (Nagai *et al.*, 2009).

Conventional remote sensing platforms often have a fixed spatial resolution; MUAVs have the ability to fly at different levels to obtain datasets at various spatial resolutions enabling multi-scale data collection (Rango *et al.*, 2006). The spatial resolution of MUAV imagery fills the gap between ground-based measurements and aerial photography from manned aircraft (Hakala *et al.*, 2010). For the purposes of vegetation mapping, hyperspatial MUAV imagery allows areas that are predominately background, such as soil, to be identified and thus ignored in further image analysis (Hunt *et al.*, 2008; Sugiura *et al.*, 2005).

Whilst the typical resolution of satellite and aerial photography data is sufficient for studies undertaken at a regional scale it is insufficient to answer many of the questions asked by ecosystem modellers and agencies (Rango *et al.*, 2006; Anderson and Gaston, 2013). Coarser resolution data can result in pixels representing two different surface types. For example, at edges of vegetation, a pixel's reflectance will be made up the vegetation's reflectance and the reflectance of the neighbouring surface, such as soil. With high resolution MUAV imagery it is possible to segment the vegetation from background pixels (Hunt *et al.*, 2008), which has the potential to improve the accuracy of any vegetation indices that are calculated (e.g. Normalised Difference Vegetation Index and/or Photochemical Reflective Index) and associated derivatives, such as Leaf Area Index (LAI) (Sugiura *et al.*, 2005). In addition, high resolution MUAV imagery enables the determination of the spatial characteristics of vegetation such as canopy size and the gaps between vegetation that are associated with erosion risk and habitat condition (Rango *et al.*, 2006; Laliberte and Rango, 2009).

1.2.2 Temporal resolution

MUAVs also offer the potential for a higher temporal resolution than conventional platforms. For the purpose of monitoring dynamic vegetation, in particular the study of crop health and yield, satellite sensors have unfavourable revisit times (Berni *et al.*, 2009). Satellites and aerial photography from manned aircraft are subject to weather with cloud cover rendering them unusable. Even if a satellite

re-visits an area of interest with sufficient frequency, there is no guarantee that it will be able to collect cloud free data.

MUAVs have the advantage that they can be deployed on-demand to map an area of interest at critical times. For example, UAV imagery can be collected before and after a specific treatment has been applied to a crop, such as fertilisation or irrigation, to ascertain the effectiveness of the treatment over the immediate short term. UAVs are also suitable for "target of opportunity" events, such as mapping changes in vegetation after a storm (Rango *et al.*, 2006). The on-demand capability of UAV data acquisition gives rise to the term 'hypertemporal' resolution of the acquired data.

1.2.3 Costs

Operational costs of MUAVs are low in comparison to other platforms. Manned aerial photography has high operational costs (Berni *et al.*, 2009) and is often unavailable if the aircraft and/or operators have been deployed on another task. Purchase of high resolution satellite imagery can also be prohibitively expensive, particularly for a small agriculturalist that only requires data spanning a relatively small area (< 1000 ha), but has to purchase a satellite image at a fixed spatial extent. Conducting a ground survey is labour intensive, time-consuming and thus expensive to complete (Nagai *et al.*, 2009).

The cost of the UAV platform should be compared to the cost of manned aircraft and satellites. Some UAVs are very complex and are the product of years of extensive research and development, resulting in expensive systems that are no cheaper than the cost of conventional aircraft. In this study, however, the focus is on MUAVs, based on airframes that only cost a few thousand dollars to purchase.

The number of people required to operate a remote sensing system must also be factored in to any cost comparison. A traditional system in a manned aircraft may require one or two pilots and another one or two people to operate the equipment. A simple MUAV can be operated by as little as one person, however, two people is preferable for most operations.

1.2.4 Other advantages

UAVs are also ideally suited to particular tasks which are often described colloquially as dirty, dull and dangerous. That is, UAVs can operate in environments dangerous to humans (Everaerts, 2008). An example would be to assist with relief by producing near-real time imagery of a disaster zone. Access to dangerous areas, such as this, is of particular advantage if the imagery can be georeferenced without the need for human access to place Ground Control Points (GCPs) (Tsai *et al.*, 2010).

The low operating altitude of an MUAV has advantages other than allowing for high resolution data to be collected. An MUAV can operate on a cloudy day, whereas a conventional aircraft would have its view of the ground obscured by low cloud (Thrun *et al.*, 2003). An MUAV can fly at low altitudes at which it is illegal to fly a manned aircraft (Kaneko *et al.*, 2011), allowing it to carry out tasks such as atmospheric measurements (Marchbank, 2009a). The flexibility of an MUAV and the ability to have control over image acquisition can also be of advantage (Oleire-Oltmanns *et al.*, 2012) in order to match the scale of aerial observations to the scale of the spatial objects of interest.

1.3 Limitations of MUAVs

1.3.1 Coverage

A limitation of imagery acquired by small and lightweight MUAVs is the restricted spatial coverage. Flying low to obtain data at an ultra-high spatial resolution means that the area covered by each image is small. For example, an MUAV flying at 50 m Above Ground Level (AGL) with a 45 degree Field of View (FOV) would have a footprint of only 50 m x 40 m. A small sensor footprint implies that a longer flying time is needed to cover large areas; it also results in large datasets requiring significant processing time in order to generate a continuous spatially coherent dataset (Grenzdörffer *et al.*, 2008). VTOL MUAVs typically only have short flight durations (e.g. 10 minutes), thus are unable to cover large areas. As a consequence, MUAVs are suited to specific applications that involve a limited spatial extent such as monitoring of crops over areas in the order of 1 - 10 hectares. Whilst there are some lightweight fixed wing MUAVs that fly faster for longer durations (> 30 mins)

and cover larger areas, they do so at the price of spatial resolution. As a consequence of their higher flying speed, the fixed wing MUAV needs to fly higher to increase image footprint and hence maintain sufficient image overlap.

Collecting a large number of images to cover an area of interest can also dictate that a large number of GCPs will be required to enable accurate georectification of the imagery (Grenzdörffer *et al.*, 2008). GCPs can have a high cost of collection and in some cases may be difficult or impossible to collect (Hruska *et al.*, 2005). Long processing times and the resources required to collect a large number of GCPs can make MUAV surveys inefficient and thus detract from the other benefits of MUAV imagery. Larger areas may well be suited to a different type of UAV, more conventional aerial photography platforms, or even satellite imagery.

1.3.2 Sensor quality

A limiting factor for UAVs, and in particular MUAVs, is the payload capacity of the system. An MUAV is, at best, only capable of carrying a few kilograms, which limits the choice and often the quality of the sensors that can be carried. It is typical for uncalibrated, low-cost, compact cameras to be used for photography, which tend to have low spectral and radiometric resolutions (Laliberte and Rango, 2011) and have lenses for which the distortion is unknown (Grenzdörffer *et al.*, 2008).

The limited payload also limits the available options for a range of other sensors that maybe required for specific applications. Traditional methods of processing aerial photography can make use of high quality GPS/IMU hardware that records the payload (in this case the camera) position and orientation to assist with orthorectification of the imagery. However, accurate GPS/IMUs are typically large and heavy, and thus unsuitable for MUAVs. Miniaturisation of similar hardware often sacrifices accuracy – an inexpensive GPS/IMU small enough to be carried by an MUAV is for example, 1 to 2 orders of magnitude less precise than traditional "full-scale" hardware (Grenzdörffer *et al.*, 2008).

For the remote sensing of vegetation, be it natural or agricultural, a sensor capable of collecting Near Infrared (NIR) imagery is beneficial. Plants reflect much more light in the NIR part of the spectrum and there is much more information to be gained

about their biochemical and biophysical properties at these wavelengths (Asner, 1998). However, due to a lack of market demand and therefore a lack of research and development investment by manufacturers, there are very few lightweight sensors capable of capturing true NIR or multispectral imagery. The most common alternative at this time is to modify a consumer grade digital camera to have the NIR blocking filter removed (Dunford *et al.*, 2009), which results in the camera being capable of capturing what is known as Colour Infrared (CIR) imagery. However, the NIR signal, in this case, is mixed with the visible spectrum (particularly the red wavelengths), which makes it difficult to extract true NIR reflectance in a quantitative fashion.

1.3.3 Regulations

Airspace safety organisations around the world have widely varied approaches to governance of UAV operations within their country's airspace. However, in a large number of countries the use of UAVs is prohibited, or highly regulated. In the USA, the Federal Aviation Administration (FAA) does not permit civilian UAVs access to USA airspace on a continuing basis. Currently, these regulations are being reassessed to allow better access for UAVs (Rango *et al.*, 2006; Colomina and Molina, 2014). The FAA have been directed to develop a "comprehensive plan for integrating UAS into the national airspace by no later than September 2015" (Colomina and Molina, 2014).

In Australia, regulations have been in place since 2002 (Marchbank, 2009a; Colomina and Molina, 2014) that allow UAVs ongoing access to Australian airspace. CASA governs UAV operations in Australia as laid out in CASR Part 101 (CASA, 2014) (see www.casa.gov.au). The Australian UAV regulations are internationally recognised as leading the way (Wong, 2001) and other countries are looking to adopt the Australian model. However, to those just starting with aviation and UAVs, the regulatory requirements can appear to be quite restrictive. Initially, a UAV controller's certificate must be acquired, which requires the operator to have significant UAV operation training and to complete a number of aviation theory courses. Then, a UAV Operators Certificate (OC) must be applied for, which involves developing an extensive operation manual describing in detail the methods

for maintaining and operating the UAVs to be used and the safety systems that are to be put in place.

UAV regulations have been described by some authors as a limiting factor when it comes to the uptake of UAVs by the scientific community for research purposes (Rango *et al.*, 2009; Laliberte *et al.*, 2011b). However, with the increase in civilian use of UAVs around the world, there is increasing pressure on regulatory bodies to modify the regulations to improve access to airspace for UAVs, which in turn will result in more use of UAVs as remote sensing platforms (Everaerts, 2008). In Australia, UAVs can be operated by civilians if the prescribed conditions are met. It may seem onerous at first, but it must be remembered that the purpose of the regulations is to maintain airspace safety standards for all residents of Australia.

1.4 Problem statement

The benefits of UAVs for remote sensing applications include high spatial and temporal resolution, simplicity, and lower costs, making UAVs an ideal tool for collecting scientific data for a wide range of discipline areas. Applications that could benefit from UAVs include natural vegetation monitoring and mapping, precision agriculture, geological mapping, and surveying. Until recently, the uptake of UAVs within these disciplines has been limited. One of the primary reasons for this is a series of unique challenges associated with processing aerial imagery acquired by UAVs (Laliberte and Rango, 2011). Specific challenges associated with collecting scientific data with a UAV are:

1. Mosaicking of the (potentially hundreds of) images collected during a UAV flight in an efficient, accurate, and automated fashion.
2. Directly georeferencing of UAV imagery at a high level of accuracy, such that the need for GCPs is reduced or removed entirely.
3. Accurate co-registration of datasets from multiple flights with multiple sensors.
4. Relating end-products created from image data collected with specialised sensors, such as NIR and TIR, to real-world biophysical and biochemical measurements.

5. Accurate co-registration and quantification of change in multi-temporal datasets.

A potential solution to overcome the first challenge is to use mainstream photogrammetry software packages. However, these packages are not designed to deal with the characteristics of a typical UAV survey (Eisenbeiss, 2009). UAV imagery differs from conventional aerial photography in a number of important ways;

- Flight and camera configurations are often arbitrary (Eisenbeiss, 2009).
- Flying height is low in relation to the height of objects on the ground, resulting in significant perspective distortions (Zhang *et al.*, 2011; Wischounig-Strucl and Rinner, 2010)
- There is a greater variation in the amount of image overlap and the rotation angles between images (Zhang *et al.*, 2011).

In terms of the direct georeferencing challenge, there has been limited published work, e.g. Chiang *et al.* (2012), Eugster and Nebiker (2007), Pfeifer *et al.* (2012). These studies reported relatively low absolute spatial accuracy due to the use of navigation-grade GPS receivers. The other key to this challenge is an accurate synchronisation between the time of camera exposure and the spatial location (GPS derived) of the UAV, both derived from relatively low-cost and lightweight hardware.

For the co-registration challenge, there are several studies that have collected multi-sensor UAV datasets for application in precision agriculture and natural vegetation mapping, e.g. Berni *et al.* (2009), Bryson *et al.* (2013), and Bendig *et al.* (2012). However, there has been limited research into methodologies to co-register multi-sensor datasets and into the accuracy of the co-registration that can be achieved. It is important that such a methodology is as automated as possible and that the imagery can be used to create end-products that can be used to monitor real-world parameters such as vegetation health.

To address the challenge of co-registration of multi-temporal UAV datasets a change detection case study is presented. Structure from Motion (SfM) is a technique that

can create 3D models of a surface from overlapping photos and several studies have demonstrated the power of these algorithms for mapping and monitoring landslides and glaciers (Immerzeel *et al.*, 2014; Lucieer *et al.*, 2013; Niethammer *et al.*, 2010; Niethammer *et al.*, 2009; Niethammer *et al.*, 2011). This thesis will extend this research by demonstrating that change detection can be applied to a multi-temporal dataset that encompasses multiple years of data.

1.5 Research Objectives

The aim of this thesis is to develop image processing routines for direct georeferencing, image mosaicking, and co-registration of ultra-high resolution MUAV imagery from multiple sensors and with a high temporal resolution for environmental remote sensing and change detection applications. This study will make use of an existing multi-rotor VTOL MUAV platform that has a high level of operational flexibility. This platform can be operated in restrictive areas (i.e. does not require a runway) and has a low cost and low operational complexity. The five challenges outlined in Section 1.4 will form the basis for the key research objectives of this thesis:

Objective 1 – To assess existing methods to georectify and mosaic UAV imagery, and subsequently develop an algorithm that overcomes limitations in traditional approaches and enhances existing techniques to enable automated and accurate georectification and mosaicking of UAV imagery.

Objective 2 – To reduce or completely remove the need for GCPs when collecting a UAV image dataset. To develop a hardware and software solution to accurately synchronise camera exposure with GPS position. To assess the accuracy of direct georeferencing in several Structure from Motion (SfM) processing approaches.

Objective 3 – To develop a technique to co-register multiple datasets that have been collected during separate UAV flights with multiple sensors. To develop a co-registration workflow that is semi-automated with minimal user-input and without manual co-registration. To assess the spatial accuracy of co-registration between the separate sensors.

Objective 4 – To demonstrate that multispectral and thermal imagery can be related to real-world surface properties such as vegetation health and surface temperature.

Objective 5 – To demonstrate that the combination of high spatial and temporal resolution UAV datasets provide sufficiently accurate data such that change detection can be undertaken across the datasets. To measure the accuracy of the changes quantified, and to minimise any errors in the co-registration of the temporal datasets.

1.6 Thesis Structure

The structure of this thesis is *by publication*, and therefore Chapters 2-5 are four consecutive publications, that address the objectives. At the time of thesis publication Chapter 2 was published in *Remote Sensing* (Turner *et al.*, 2012); Chapter 3 was published in *Transactions on Geoscience and Remote Sensing* (Turner *et al.*, 2014b); Chapter 4 was published in *Remote Sensing* (Turner *et al.*, 2014a)*;* and Chapter 5 was published in *Remote Sensing* (Turner *et al.*, 2015). Each chapter addresses the relevant literature and includes detailed methodology, results, discussion, and conclusion sections. Chapter 6 provides a final conclusion that draws together the separate chapters and reports against the objectives of the thesis. The structure of the thesis is outlined in Figure 1.3.

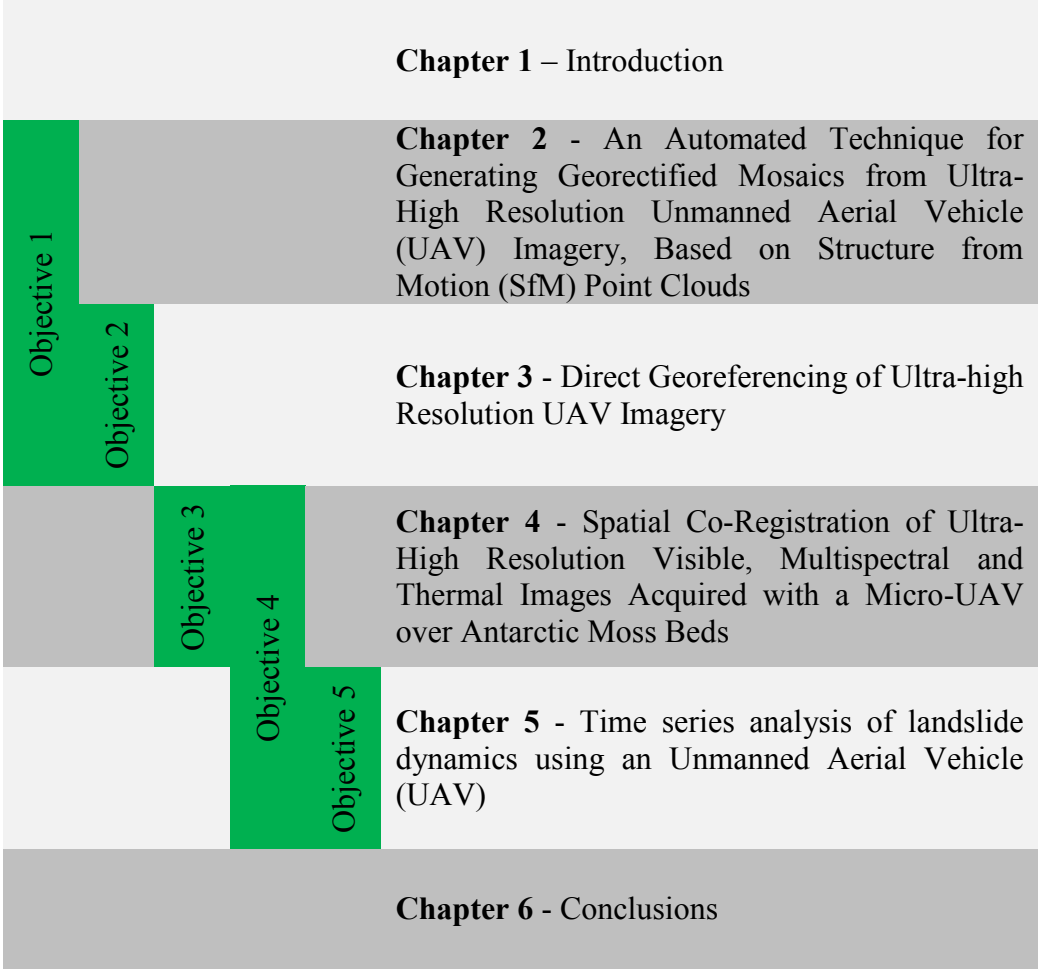

Figure 1.3 - Structure of thesis and achievement of objectives

Chapter 2

An Automated Technique for Generating Georectified Mosaics from Ultra-High Resolution Unmanned Aerial Vehicle (UAV) Imagery, Based on Structure from Motion (SfM) Point Clouds

Chapter 2 describes a novel technique to georectify UAV imagery and has been published in Remote Sensing 14th May 2012.

Turner, D., A. Lucieer and C. Watson (2012). "An Automated Technique for Generating Georectified Mosaics from Ultra-High Resolution Unmanned Aerial Vehicle (UAV) Imagery, Based on Structure from Motion (SfM) Point Clouds." Remote Sensing **4**(12): 1392-1410.

Abstract

Unmanned Aerial Vehicles (UAVs) are an exciting new remote sensing tool capable of acquiring high resolution spatial data. Remote sensing with UAVs has the potential to provide imagery at an unprecedented spatial and temporal resolution. The small footprint of UAV imagery, however, makes it necessary to develop automated techniques to geometrically rectify and mosaic the imagery such that larger areas can be monitored. In this paper, we present a technique for geometric correction and mosaicking of UAV photography using feature matching and Structure from Motion (SfM) photogrammetric techniques. Images are processed to create three dimensional point clouds, initially in an arbitrary model space. The point clouds are transformed into a real-world coordinate system using either a direct georeferencing technique that uses estimated camera positions or via a Ground Control Point (GCP) technique that uses automatically identified GCPs within the point cloud. The point cloud is then used to generate a Digital Terrain Model (DTM) required for rectification of the images. Subsequent georeferenced images are then joined together to form a mosaic of the study area. The absolute spatial accuracy of the direct technique was found to be 65–120 cm whilst the GCP technique achieves an accuracy of approximately 10–15 cm.

2.1 Introduction

Historically, Unmanned Aerial Vehicles (UAVs) have primarily been used for military applications. More recently, the use of UAVs in the civilian domain as remote sensing tools presents new and exciting opportunities. Improvements in the availability of accurate and miniature Global Positioning Systems (GPS) and Inertial Measurement Units (IMUs), along with the availability of quality off-the-shelf consumer grade digital cameras and other miniature sensors have resulted in an increased use of civilian UAVs (Nebiker *et al.*, 2008). The highest spatial resolution data available from conventional platforms, such as satellites and manned aircraft, is typically in the range of 20–50 cm/pixel. UAVs are capable of flying much lower and hence can collect imagery at a much higher resolution (Hunt *et al.*, 2010b; Scaioni *et al.*, 2009), often at a sub-decimetre resolution, even as detailed as 1 cm/pixel. The temporal resolution of conventional systems is limited by the availability of aircraft platforms and orbit characteristics of satellites. For the purpose of monitoring highly dynamic vegetation, satellite sensors are often limited due to unfavourable re-visit times (Berni *et al.*, 2009).

Many studies have successfully used UAVs to map and monitor areas of vegetation that are of an agricultural and/or an environmental interest, see for example (Dunford *et al.*, 2009; Johnson *et al.*, 2003; Lelong *et al.*, 2008; Rango *et al.*, 2009). Johnson *et al.* (2003) used a small fixed wing UAV to collect imagery over a commercial vineyard in California. The imagery had a spatial resolution of 20 cm/pixel and was processed to segment the scenes into vegetation and soil areas and to subsequently calculate percentage vegetation cover. Monitoring of small plots within wheat crops in southwest France Lelong *et al.*, (2008) is another example of UAVs assisting with agricultural processes. Lelong *et al.* (2008) used a modified digital camera to collect imagery in four bands, red, green, blue and near-infrared to enable the calculation of vegetation indices such as the Normalized Difference Vegetation Index (NDVI).

In an environmental monitoring context Rango *et al.* (2009) deployed a fixed wing UAV in the rangelands of southern New Mexico, acquiring imagery with at a 5-6 cm/pixel resolution. Laliberte *et al.* (2011a) also collected imagery of the New

Mexico rangelands, but also used a six band multispectral camera to capture high resolution data in the near infrared. Imagery of such high spatial resolution can provide a lot of information, such as detailed area of vegetation and bare soil coverage, composition by functional or structural group, spatial distribution of plants, inter canopy gaps and in some cases, vegetation type (Rango *et al.*, 2006). In another study, Dunford *et al.* (2009) used a paraglider type UAV to acquire imagery with a spatial resolution of 6-21 cm/pixel over 179 ha of riparian forest in France. An object-based classification approach was then found to be the most accurate classifier for the detection of dead wood within the forested area (Dunford *et al.*, 2009).

Despite significant evidence highlighting the value of UAVs in the fields of precision agriculture and environmental monitoring, the collection of ultra-high resolution UAV imagery presents a number of challenges. Due to the relatively low flying height (e.g., 50–120 m) of micro-UAVs (<5 kg), the images have a small footprint (e.g., 50 × 40 m when flying at 50 m above ground level with a typical camera and lens configuration). This necessitates the capture of a large number of images to achieve the spatial coverage required for many applications. For example, a single flight covering approximately 2 ha can yield around 150–200 images. To maximise the potential of the UAV technology for environmental and agricultural applications, it is essential that an automated, efficient, and accurate technique be developed to rectify and mosaic the large volume of images generated.

There are fundamental differences between imagery collected by a UAV flying at low altitude compared to that collected by a traditional aerial platform flying at higher altitudes. UAV imagery is often collected in a haphazard manner (*i.e.*, flight lines with variable overlap and cross-over points); it has large rotational and angular variations between images (Zhang *et al.*, 2011); the altitude of the platform is low in relation to the height variation within the scene, causing large perspective distortions (Zhang *et al.*, 2011) ; and the exterior orientation (EO) parameters are either unknown or, if measured, they are likely to be inaccurate. UAV imagery often has high variability in illumination, occlusions and variations in resolution (Barazzetti *et al.*, 2010a), which are characteristics more typical of those usually presented in close-range photogrammetry applications (Luhmann *et al.*, 2006). Hence, UAV photography has characteristics of both traditional aerial photography and

terrestrial photography, and there are opportunities to use image processing algorithms that are applicable to both types of imagery, as suggested by Barazzetti *et al.* (2010a).

Recently there have been advances in the realm of Computer Vision (CV), resulting in new algorithms for processing terrestrial photography. Examples are the powerful Scale Invariant Feature Transform (SIFT) (Lowe, 2005) feature detector, and the Structure from Motion (SfM) algorithms that make use of SIFT features to create 3D models from a series of overlapping photos (Snavely, 2010). SIFT is a region detector, rather than an interest point extractor that would typically be used by traditional photogrammetric software (Lingua *et al.*, 2009). As a region detector it has been demonstrated that SIFT is applicable to UAV imagery due to its robustness against changes in rotation, scale, and translation between images (Lingua *et al.*, 2009).

The standard approach in modern photogrammetry is to employ a Bundle Block Adjustment (BBA) to solve for the exterior orientation of each photograph and, if required and provided the geometry of the block of photographs allows it, to solve for additional parameters such as the interior orientation (IO). An introduction to the BBA is provided by e.g., Wolf and Dewitt (2000). Most commonly, metric mapping cameras are used for aerial photography for which the IO parameters are known. UAV imagery is typically collected with consumer grade cameras for which IO parameters are neither known nor stable. Measured values for EO parameters, typically captured at relatively low accuracy in the case of UAV photography, can be included in the BBA, and provide approximate measurements for the bundle adjustment (Barazzetti *et al.*, 2010b).

Increasingly, in the case of traditional aerial photogrammetry, the position and orientation of the camera can be derived from GPS and IMU data with sufficient accuracy to allow direct georeferencing without the need for Ground Control Points (GCPs). Often if ground control is available it is primarily used to ensure a reliable transformation from the GPS based coordinate system into the required map coordinate system. This is not the case for UAV photography because of the lower

accuracy of the GPS/IMU data and because of the very large scale of the imagery and map products.

Tie/pass points are required to complete a BBA and are typically automatically generated in the case of traditional aerial photography by an interest point extractor algorithm. For UAV imagery, a SIFT algorithm can be used and has the potential to generate a large number of features that can be used as tie/pass points, supplying more redundant observations for a BBA and thus improving the accuracy of the results (Zhang *et al.*, 2011).

Table 2.1 clearly demonstrates that with UAV imagery, the IO and EO parameters are often not well known, making the use of a traditional BBA problematic or, at least, more similar to terrestrial or close-range photogrammetry. Attempts have been made to overcome these limitations by developing techniques to specifically work with UAV imagery. Berni *et al.* (2009) used onboard IMU and GPS data to estimate the camera's approximate EO parameters which were then imported into traditional photogrammetric software along with calibrated images to create a mosaic. The images collected had a high level of overlap, allowing only the central part of the images to be used to avoid the extremities where view angle caused perspective distortions (Berni *et al.*, 2009). A minimum number of GCPs were then manually measured and an aerotriangulation performed. Berni *et al.* (2009) were then able to use an existing Digital Terrain Model (DTM) to generate an orthomosaic, however, no overall spatial accuracy for this method was reported.

Table 2.1 - Comparison of Bundle Block Adjustment variables.

Variables	Traditional Aerial Photography	UAV Imagery
IO parameters—Camera calibration e.g., focal length, principle point, lens distortion parameters	Often known as metric, calibrated, cameras are used	Not usually known and often unstable because consumer grade cameras are used
EO parameters—Camera position and orientation	Often measured by high accuracy onboard GPS/IMU	Either unknown or inaccurate due to limited accuracy of navigation grade GPS and miniature MEMs IMU
GCPs—3D ground control	Manual identification of natural or artificial targets in the imagery and surveyed in situ for accurate 3D coordinates	Manual identification of natural or artificial targets identified in the imagery and surveyed in situ for accurate 3D coordinates
Tie/Pass points—2D image points	Manually identified or automatically generated by interest point extractor algorithm	Manually identified or automatically generated by region detector such as SIFT
Object points—3D points	The coordinates of tie and pass points are computed as part of the BBA. The coordinates of terrain points are computed using image matching techniques (usually a hybrid of area and feature based) to identify conjugate points in two or more images, and then by intersection based on co-linearity condition equations.	The coordinates of all SIFT features are computed as part of the BBA (bundler software). A denser point cloud of terrain points is calculated using patch-based multi-view stereo (PMVS) techniques from three or more images.

Laliberte *et al.* (2008) developed a method that relied on an existing underlying orthorectified photo and DTM. They initially estimated camera EO parameters from onboard sensors and then iteratively matched each individual image with the existing orthophoto to improve the accuracy of the EO parameters and provide GCPs based on matched features between images. After many iterations of this process,

photogrammetric software used the EO parameters and GCPs to orthorectify the images and generate a seamless mosaic. Laliberte *et al.* (2008) identified that their methodology has a number of limitations: it requires pre-existing orthophotos that can quickly become out of date, the 10 m DEMs used for orthorectification were not detailed enough compared to the resolution of the UAV imagery, it suffered from problems finding accurate EO parameters, and achieved variable accuracy of the automatically generated tie points. The overall accuracy of the method was reported to have an RMS error of 0.48 m, (corresponding to ~10 pixels), however, it was acknowledged that the method had only been tested over relatively flat terrain and algorithm performance in areas with higher vertical variability had not been confirmed (Laliberte *et al.*, 2008).

Bryson *et al.* (2010) presented a georectification and mosaicking technique that used onboard IMU/GPS data to initially estimate camera pose and then image features were matched across the image dataset. A bundle adjustment then used the initial camera pose estimates and the matched features to refine the camera poses; subsequently the images are then rectified and mosaicked using these poses. The method described by Bryson *et al.* (2010) is similar to the method that we propose in that it uses similar processes (e.g., bundle adjustment, feature matching). However, there are significant differences in the platform used (rotary wing *versus* fixed wing) and the resolution of the imagery collected. Also, in this study we do not use onboard IMU data; we can automatically identify GCPs, and we integrate the use of multiview stereopsis algorithms into the solution.

These techniques performed well but many are based on traditional photogrammetric software designed to process imagery collected from conventional platforms. Some of these techniques have some key disadvantages: they use existing underlying DTMs and base orthophotos, they rely on complex workflows to estimate camera EO parameters, and, in some cases, require human intervention to identify GCPs.

In this study, we describe a methodology for geometric image correction that uses new CV and SfM algorithms that are more applicable to UAV photography. The technique is fully automated and can directly georeference and rectify the imagery with only low accuracy camera positions, resulting in UAV image mosaics in

real-world coordinates. Alternatively, GCPs can be automatically identified to improve the spatial accuracy of the final product. The automation and simplicity of our technique is ideally suited to UAV operations that generate large image data sets that require rectification and mosaicking prior to subsequent analysis.

2.2 Methodology

2.2.1 UAV Platform and Photo Acquisition

The UAV platform used in this study is a multi-rotor OktoKopter (Figure 2.1). This platform is purpose designed for aerial photography (Mikrokopter, 2011) and has a stabilised camera mount, to which we have fitted a small format digital camera (Canon 550D 18 Megapixel, 5,184 × 3,456 pixels, DSLR, with Canon EF-S 18-55 mm F/3.5–5.6 IS lens). Image resolution (ground pixel size) at a typical flying height above terrain of 50 m is approximately 1 cm/pixel. The OktoKopter has a payload limit of approximately one kilogram and with a full payload has a flight duration of around 5–6 min. A single flight conducted at 50 m above ground level (AGL) can cover an area of around 4–5 ha, producing approximately 200–300 images under a standard operating configuration. Larger areas are covered with multiple flights, or by increasing the flying height and lowering the spatial resolution.

Figure 2.1 - Oktokopter fitted with Canon 550D

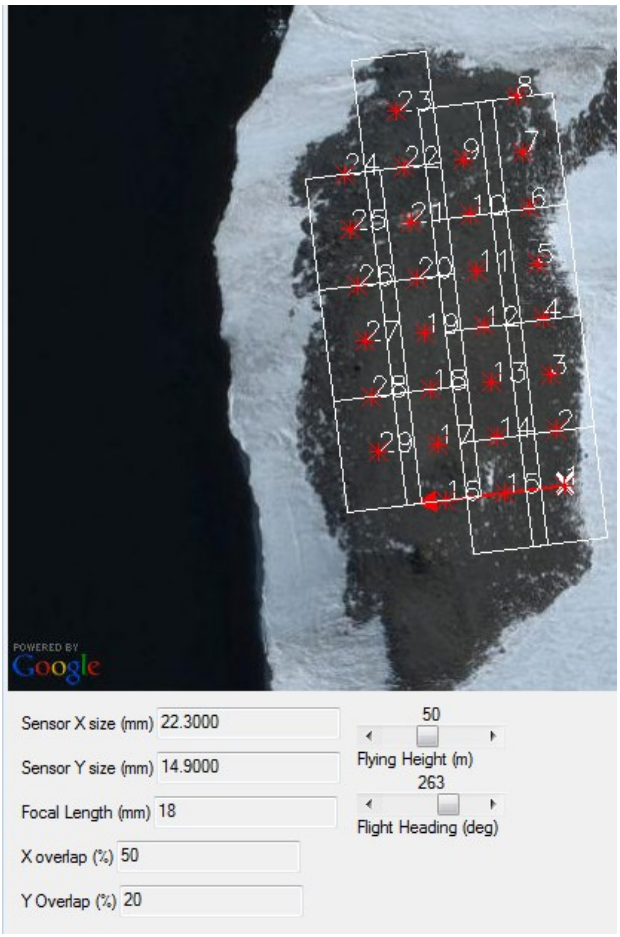

Figure 2.2 - Software to plan flight over Antarctic moss bed

The Oktokopter has an onboard navigation system based on a navigation grade GPS receiver (U-blox LEA6S) and a small Microelectromechanical System (MEMS)-based IMU (Mikrokopter Flight Controller ME V2.0) enabling it to fly autonomously through a pre-defined set of waypoints. As part of this study, we developed flight planning software that calculates the spacing and layout of waypoints to optimise the image acquisition over a region of interest at a nominated image scale (see Figure 2.2). Imagery is acquired at the maximum rate allowed by the camera (approximately 1 Hz), providing ample image overlap in addition to redundancy to account for occasional outlier acquisitions (excessive tilt or poor exposure).

2.2.2 Block adjustment and Point Cloud Generation

The automated mosaicking technique encompasses a number of stages. The first step requires the manual elimination of any images outside the study region or of limited

quality. This qualitative process is the only manual intervention required in the processing chain.

The ideal processing strategy for the imagery would be traditional photogrammetric software that uses GPS/IMU data for bundle adjustment and thus provide significant redundancy in block and photo invariant parameters. Our micro-UAV platform used for this study, however, does not carry a GPS receiver and IMU sensor that can collect data with sufficient accuracy for these techniques to work. In addition, a consumer grade digital camera is used, which means that IO calibration parameters are neither known nor stable. To overcome these problems we have applied bundle adjustment software (Bundler, http://phototour.cs.washington.edu/bundler/) specifically designed to enable automated 3D reconstruction of a scene captured by cameras with unknown internal parameters (Snavely *et al.*, 2008). Dandois and Ellis (2010) demonstrated that it has become relatively straightforward to use newly developed CV and SfM algorithms to generate 3D geometry from sets of overlapping digital photographs collected from UAV platforms.

The Bundler software (Snavely, 2010) uses SfM algorithms to compute the camera geometry and to generate a sparse 3D point cloud for the area of interest. The SfM framework initially uses the SIFT algorithm (Lowe, 2005) to detect and describe local features within each image. SIFT feature descriptors are invariant to scale, orientation, affine distortion and partial illumination changes (Lowe, 1999) and can be matched across multiple images. Using the conjugate (matched) image points as input, a bundle block adjustment is applied to compute the exterior orientation (position and orientation) of each camera exposure station. In addition, the bundle adjustment computes the interior orientation parameters (focal length and two radial distortion parameters) of each image, although if required these parameters can be implicitly defined and fixed for all images. The bundle adjustment output includes 3D coordinates for a sparse point cloud of SIFT features in an arbitrary coordinate system which we denote (p_x, p_y, p_z). The Bundler software package is fully automated, requiring only images and a few optional user definable parameters as input.

2.2.3 3D Point Cloud Transformation Using Direct Technique

A seven parameter Helmert transformation (three translations, three rotations and one scale parameter) can be used to describe the relationship between the point cloud coordinate system (model space) and a real-world (object space) coordinate system (e.g., a projected Universal Transverse Mercator (UTM) easting and northing, and height). We initially use the computed (bundle adjustment) and measured (GPS) values of the exposure station coordinates to solve for the Helmert transformation parameters. This approach, which does not rely on GCPs in the imagery, is often referred to as direct georeferencing (Nagai *et al.*, 2004), and is useful when working in unsafe or inaccessible areas where GCPs cannot be physically measured on the ground.

The GPS coordinates of the exposure station are determined using the Oktokopter's on-board GPS receiver, with pre-flight synchronisation of the camera's internal clock with GPS time so that during post-flight data analysis the GPS position at the moment of exposure can be written to the EXIF header information for each image. The height measurements from navigation-grade GPS receivers are relatively poor, hence we use height measurements provided by the OktoKopter's barometric altimeter, which is estimated to be accurate to 1 m when used over short time scales as per a typical UAV flight.

The 3D coordinates of the exposure stations are extracted from the Bundler output and denoted p_x, p_y, p_z. Image EXIF header information is read to extract the matching GPS location. The GPS latitude, longitude and altitude (relative to the WGS84 datum) are subsequently converted into the UTM projected coordinate system, resulting in easting, northing, and ellipsoidal height coordinates. Transformation to an orthometric height system is also possible through the use of a local geoid model if required. Corresponding exposure station coordinates from the bundle adjustment and the GPS are then matched (see Table 2.2 for an example) to provide a list of point pairs used to compute the parameters of a Helmert transformation. The number of point pairs available is equal to the number of images used by Bundler to generate the point cloud, this number will depend on how large an area is being mapped, but for a single flight there can be as many as 200 point pairs.

Table 2.2 - Sample point pairs list

Real World Coordinate System			Bundler Coordinate System		
Easting	**Northing**	**Height**	p_x	p_y	p_z
481,495.15	2,638,913.85	39.81	5.2142	−14.3954	−0.7744
481,494.54	2,638,915.10	40.03	5.1918	−14.0937	−0.9143
481,494.53	2,638,918.55	40.90	5.0252	−13.6941	−0.8905
481,494.10	2,638,919.18	40.80	5.2283	−13.3615	−0.9766
481,495.25	2,638,920.18	40.41	5.2167	−13.1875	−0.8768
⋮	⋮	⋮	⋮	⋮	⋮

Errors in the measured GPS coordinates, the Bundler derived exposure station coordinates, and the lever arm between the camera and the GPS antenna contribute to uncertainty in the derived transformation parameters. The camera and GPS antenna share a common vertical axis to within a few centimetres and a vertical offset of approximately 25 cm. The solution for our system, however, is dominated by GPS errors that limit the absolute accuracy to 5–15 m when using a pseudorange only navigation-grade GPS receiver (Defence, 2008) The absolute accuracy of our derived point cloud is limited primarily by the navigation grade GPS, but we find that the translation parameters typically have low formal errors (often < ±40 cm) indicating that the relative position of the GPS points, and thus the transformation model, has comparatively high precision.

2.2.4 3D Point Cloud Transformation Using GCP Technique

If GCPs are established prior to photography, then the real-world coordinates of these GCPs can be used to derive the parameters of the Helmert transformation, rather than rely on GPS data from the UAV. Accurate GCP coordinates can potentially improve the solution of the Helmert transformation and therefore result in a higher accuracy of the final point cloud and image features. For this purpose, we use circular metal targets (12 cm diameter) painted with fluorescent orange paint distributed across the region to be mapped. The coordinates of these GCPs are measured using a survey grade dual frequency differential GPS, with a typical accuracy of 2 cm in the horizontal and 4 cm in the vertical (relative to a local coordinated benchmark).

The point cloud generated by the Bundler software is relatively sparse and insufficient to reliably identify the GCPs. A novel multi-view stereopsis algorithm (Furukawa and Ponce, 2009) can be applied to the output from the Bundler software to densify the sparse point cloud. This algorithm is implemented in the Patch-based Multiview Stereo (PMVS2) software. A detailed description of the algorithm can be found in Furukawa and Ponce (2009) and Lucieer *et al.* (2011). The resulting PMVS2 point cloud has extremely dense point spacing, typically around 1–2 cm, with each of the orange GCP targets generating multiple 3D points (Lucieer *et al.*, 2011).

The coordinates of the points in the PMVS2 point cloud are still in the bundler coordinate system (p_x, p_y, p_z) but can be transformed into real-world coordinates with the Helmert transformation parameters determined from the direct georeferencing approach (Section 2.2.3). Transforming the point cloud into the same coordinate system as the GCPs enables automatic matching of the orange discs in the point cloud with their corresponding real-world GPS coordinates. A simple RGB threshold is applied as the point cloud is transformed to filter out the orange pixels. The locations of the orange points are recorded both in the original coordinate system (p_x, p_y, p_z) and the transformed real-world coordinate system: easting, northing and height.

In most cases, multiple orange points are returned for each target, using a search radius of 60 cm we group these points based on their spatial distribution. The centroid of each group of points is determined and used as the penultimate bundler based coordinate of the GCP. These centroid coordinates are then matched against the *in situ* field survey coordinates via a simple separation criterion, *i.e.*, identifying point pairs that are no more than 2 m apart thereby eliminating misidentified orange points as their location will typically not be close to a GPS coordinate.

As the original Bundler coordinates (p_x, p_y, p_z) were also recorded for the orange disc points we can now replace the calculated centroids with (p_x, p_y, p_z) and derive a new list of point pairs (similar to Table 2.2). If all GCPs were successfully identified and matched to their corresponding GPS coordinate we will typically have up to 60 point pairs from which to calculate a new set of Helmert transformation parameters that have an improved accuracy and precision compared to the direct georeferencing

technique. This improvement is due to the fact that the Helmert transformation parameters are now based on higher accuracy GCPs based on survey-grade GPS measurements rather than the on-board navigation-grade GPS coordinates. The new solution also has an improved precision which can be seen in the reduced formal errors of transformation parameters (e.g., errors reduced from ~40 cm to ~5 cm in translation parameters).

2.2.5 Rectification of the Images

The locations of the matched image features used to derive the point cloud are extracted directly from the bundle adjustment output. For every image we extract the image coordinates of each of these features ($Image_x$, $Image_y$) and their corresponding 3D bundler coordinates (p_x, p_y, p_z). The previously derived Helmert transformation parameters are then applied to the (p_x, p_y, p_z) coordinates to transform them into the real world coordinate system (easting, northing, height). We generate a table of corresponding image coordinates (2D) and real-world coordinates (planimetric only) for every feature in the dataset (Table 2.3).

Table 2.3 - Example list of GCPs for an image

Easting	Northing	$Image_x$	$Image_y$
481,497.41	2,638,927.16	4,412.62	149.99
481,497.74	2,638,926.96	4,446.58	207.21
481,497.59	2,638,927.83	4,502.50	70.89
481,497.68	2,638,926.44	4,391.27	273.48
⋮	⋮	⋮	⋮

The large amount of image overlap in our datasets allows us to only transform the central part of the images to avoid distortions at the extremities, in a similar manner to Berni *et al.* (2009). The number of matched features and thus GCPs for each image is typically quite large (2,000–10,000) and a Delaunay triangulation uses these GCPs to rectify each individual image. The density of the GCPs gives us the equivalent of a high resolution Digital Terrain Model (DTM) of the area of the image allowing the triangulation to produce accurate results.

2.2.6 Mosaicking

The final stage of the process is to join the images into a single mosaic that covers the study area. Colour balancing can initially be used to remove differences in exposure and lighting conditions between the images resulting in an improvement of the visual integrity of the final mosaic. Colour balancing can be performed with standard image/photo processing packages, or within mosaicking software. However, to maintain visual integrity of the imagery, we chose not to use any colour balancing or seam blending, allowing the final product to be quantitatively assessed without bias.

As all images are now rectified and georeferenced, it is a straightforward process to mosaic them with a georeferenced mosaicking algorithm, which is for example available in ENVI (ITTVIS, 2011). As there is a large amount of overlap between the images in the dataset, only about one third of the images are required to create a mosaic of the study area. Selection of the images at this time is a simple manual process that involves adding images to the mosaic until sufficient coverage is achieved. This is a processing step that could be easily automated and this will be the subject of further research.

2.3 Results and Discussion

2.3.1 Study Area and Dataset

To illustrate the effectiveness of our georeferencing and mosaicking technique we present a case study of UAV remote sensing in Antarctica. The Windmill Islands region near Casey (Australia's largest station) has the most extensive and well-developed vegetation in Eastern Antarctica (see Figure 2.3). Mosses are the most dominant plants in Antarctica. These mosses preserve a record of past climate along their shoots, which make them a valuable proxy for climate change at remote sites. Climate change is now recognised as occurring in the high latitudes rendering Antarctica one of the most significant baseline environments for the study of global climate change. Temperature, UV-B, and changes in water availability have been identified as the three key factors that will change in the Antarctic regions with climate change. Despite this,

there have been few long-term studies of the response of Antarctic vegetation to climate (Convey *et al.*, 2009; Robinson *et al.*, 2003).

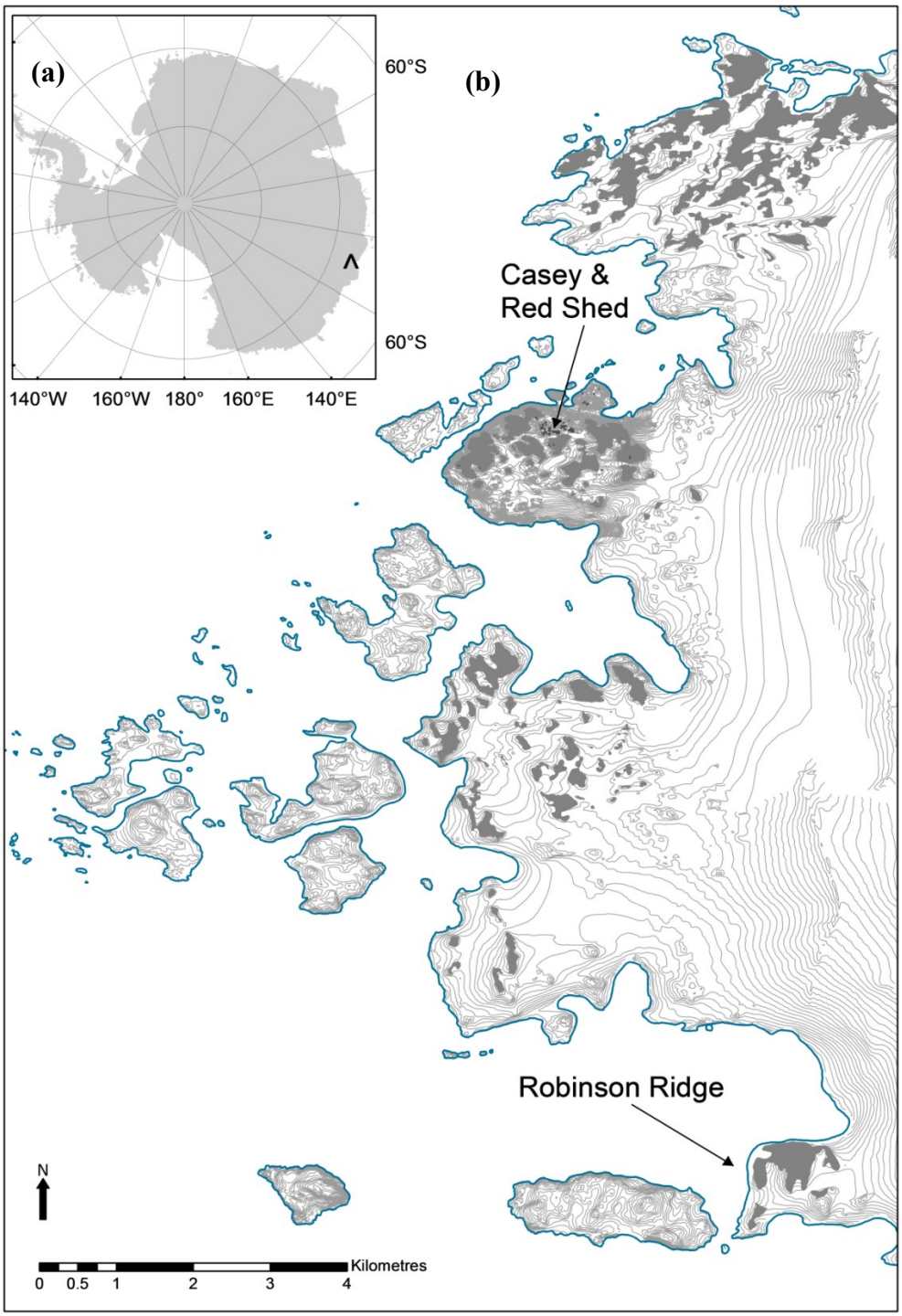

Figure 2.3 - (a) The continent of Antarctica with an arrow in Eastern Antarctica indicating the location of the Windmill Islands (b) The locations of the Robinson Ridge and Red Shed study sites in the Windmill Islands

The spatial scale of the moss beds (tens of m^2) makes satellite imagery (even recent very high resolution imagery of 0.5 m resolution) unsuitable for mapping their extent in sufficient detail. Due to logistical constraints aerial photography is impractical and also does not provide the required spatial resolution. Recent developments in the use of UAVs provide exciting new opportunities for ultra-high resolution mapping and monitoring of this unique Antarctic environment. The aim of this case study is to create ultra-high resolution and geometrically accurate image mosaics of two field sites near Casey: Robinson Ridge and Red Shed. Robinson Ridge is approximately 10 km south of Casey. These mosses grow near small melt streams on a ~100 m high ridge on the coastline (Figure 2.4). Two hundred photographs were selected from a UAV flight on 25 February 2011 flying at approximately 50 m AGL. The Red Shed site is a small bowl-shaped catchment fed by a snow melt lake right behind the main accommodation building at Casey. The mosses are concentrated around few main drainage channels. Sixty nine photos were selected from a UAV flight on 20 February 2011 at 50 m AGL.

Figure 2.4 - Moss bed area at the Robinson Ridge site with a variety of healthy moss (green), stressed moss (red/brown), and dead moss (black). Small orange discs (~10 cm diameter) and trays (~30 cm diameter) used as GCPs for geometric correction and validation are visible in the photograph

2.3.2 Helmert Transformation Parameters

For both datasets, Helmert transformation parameters were calculated initially via the direct technique (see Section 2.2.3) and then with the use of the GCP-based technique (see Section 2.2.4). A summary of the Helmert parameters obtained can be found in Table 2.4, in which the formal errors of each parameter are listed. These errors, which are the mean residual error from the least squares solution, represent the precision of the Helmert transform. It can be seen that the precision of the GCP technique for both datasets is better than the direct technique due to the error in the onboard GPS position. The precision of the direct technique for the Robinson's Ridge Helmert parameters (around 16–17 cm for the translations) is better than for the Red Shed site (around 36–45 cm for the translations). This difference in precision is most likely explained by a number of factors such as differences in flying height and the presence of outliers in the dataset used to calculate the Helmert transform. Another contributing factor is that there is more variation in the flying height for the Robinson Ridge dataset, improving the geometry of the solution and thus the precision of the transformation parameters. However, it is important to note that the precision of the Helmert transform is not a good indication of the geometric accuracy

of the resulting point clouds and image mosaics. It is thus necessary to measure the absolute spatial accuracy of the final mosaic using GCPs (see Section 2.3.4).

Table 2.4 - Helmert transformation parameters with formal errors (1 sigma) from least squares solution.

Dataset	Method	Calculated Helmert Transform Parameters						
		Translation X (m)	Translation Y (m)	Translation Z (m)	Scale Factor	Rotation X (º)	Rotation Y (º)	Rotation Z (º)
Robinson's ridge	200 camera locations (Direct)	4,814,747.58 **± 0.160**	2,638,997.85 **± 0.160**	39.06 **± 0.167**	12.658 **± 0.046**	0.615 **± 0.286**	1.204 **± 0.702**	9.977 **± 0.207**
Robinson's ridge	25 GCPs	4,814,727.54 **± 0.066**	2,638,997.77 **± 0.039**	40.30 **± 0.038**	12.774 **± 0.009**	0.994 **± 0.05**	3.158 **± 0.113**	9.810 **± 0.043**
Red shed	69 camera locations (Direct)	478,776.001 **± 0.371**	2,648,411.55 **± 0.368**	63.31 **± 0.457**	13.840 **± 0.068**	2.945 **± 0.04**	−10.277 **± 0.407**	249.122 **± 0.286**
Red shed	19 GCPs	478,777.397 **± 0.042**	2,648,409.88 **± 0.059**	54.23 **± 0.074**	13.736 **± 0.008**	−186.2325 **± 0.04**	187.737 **± 0.057**	−290.3135 **± 0.034**

For each dataset the images were rectified (see Section 2.2.5) using both the direct and the GCP techniques. The number and density of the points used for the triangulation for individual images is very high (Figure 2.5). The homogenous areas such as the snow have poor point coverage, this is due to the poor performance of the SIFT algorithm over smooth surfaces. This study was not concerned with the snow areas so this limitation does not affect the results.

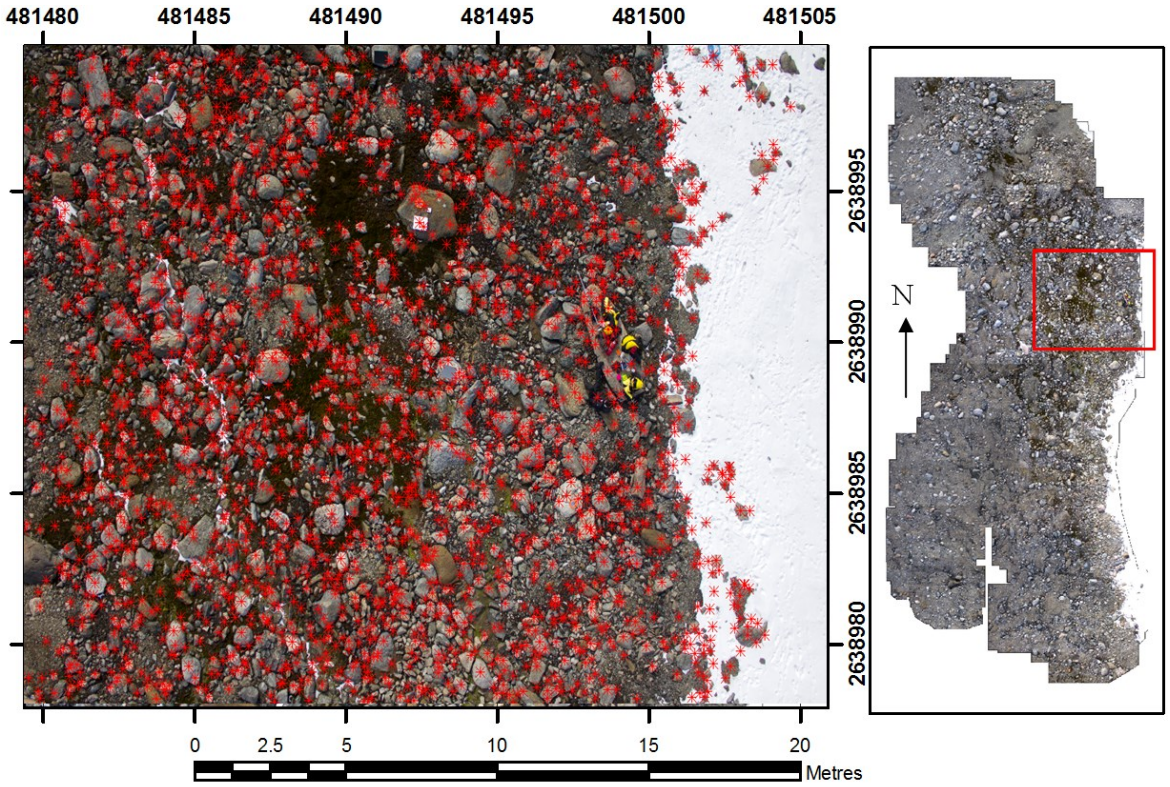

Figure 2.5 - Example of 2888 of control points (shown in red—extracted from the process described in Section 2.2.5) on a single photograph

2.3.3 Mosaics

To show how well our technique works, we do not apply any colour balancing or blend the seam lines in the production of our mosaics. A detailed section of a typical seam within the mosaic for the Robinson's Ridge site can be seen in Figure 2.6. Here the seam line running across the middle of the image is barely visible indicating a high level of accuracy in the image alignment. A qualitative analysis of the visual integrity of the mosaic reveals that there are no obvious distortions around the seam lines and the colour balancing between the neighbouring images is even, despite only relying on automated colour balancing on the camera at the time of exposure.

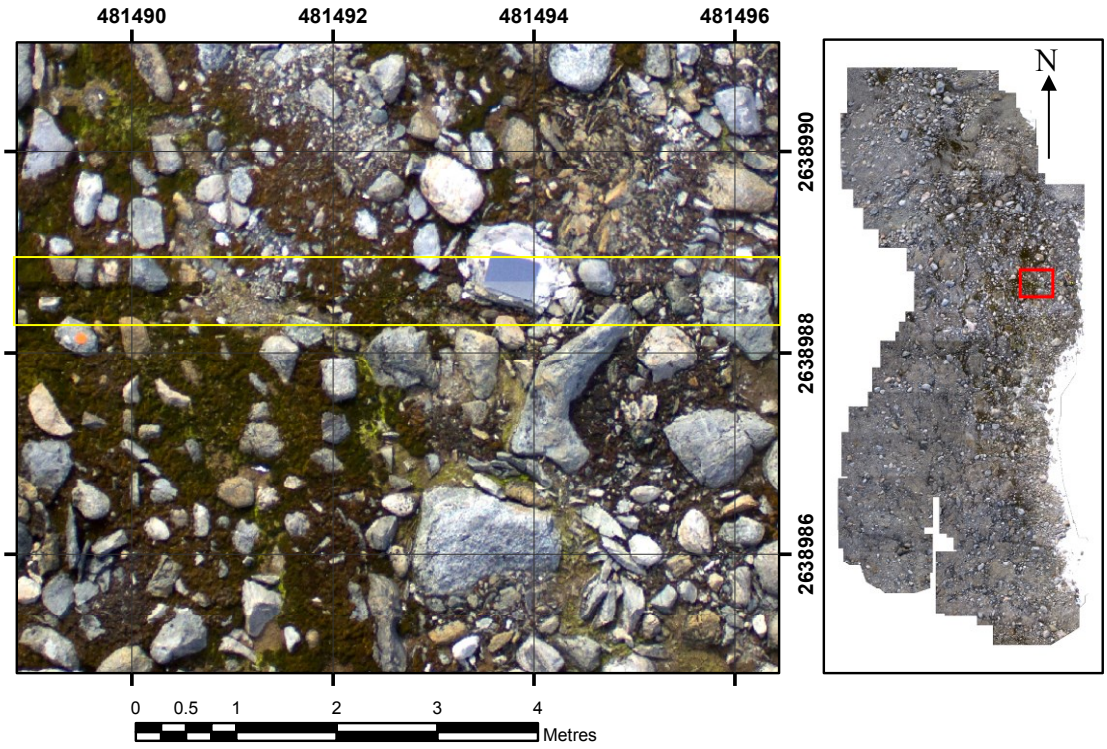

Figure 2.6 - Detailed section of a typical region within the image mosaic of Robinson's Ridge highlighting accuracy of seam lines (yellow box highlights seam line).

2.3.4 Spatial Accuracy

To quantify the absolute spatial accuracy for each image mosaic we measured the distance between the orange GCP markers in the image and their corresponding GPS coordinates. A summary of the absolute accuracy of each mosaic is presented in Table 2.5. These accuracy values highlight that the GCP technique has a superior spatial accuracy to the direct georeferencing technique, which is also visualised in Figure 2.7. The systematic nature of the errors from the direct georeferencing technique are also shown in Figure 2.7, this is typical of navigation grade GPS data collected over short time periods, where errors based on atmospheric and orbits effects are typically highly temporally correlated. The absolute spatial accuracy achieved with the GCP technique of around 10–15 cm is considered to be very good, especially when you bear in mind it is being compared to differential GPS measurements that have an error of ±2–4 cm themselves. The absolute accuracy of the direct georeferencing technique is similar for both field sites.

Table 2.5 - Summary of mosaics and their spatial accuracy

Dataset	Method	Area (ha)	Number of Check Points	Topographic Variation (m)	Mean Absolute Easting Error (m)	Mean Absolute Northing Error (m)	Mean Absolute Total Error (m)	Standard Deviation of Mean Error (m)
Robinson's Ridge	200 camera locations	0.5	43	4–24	1.076	0.571	1.247	0.184
Robinson's Ridge	25 GCPs	0.5	44	4–24	0.087	0.103	0.129	0.061
Red Shed	69 camera locations	1.1	61	13–19	0.449	0.447	0.665	0.459
Red Shed	20 GCPs	1.1	63	13–19	0.086	0.042	0.103	0.064

When we compare the absolute accuracy of the GCP technique between the two study sites, we see an insignificant difference between the two (0.10 ± 0.06 m *versus* 0.13 ± 0.06 m). Topographic influences (there is a much larger variation in height in the Robinson's Ridge dataset compared to the Red Shed dataset—Table 2.5) will drive some of the differences observed in accuracy between the datasets. Further investigation of the absolute spatial error in the Robinson's ridge dataset, the largest errors are at the GCPs at the extremities of the mosaic, e.g., in the south at the top of the hill and in the north at the bottom of the hill. If we do not incorporate these points in the accuracy assessment the mean total error is reduced to 0.112 m (with a standard deviation of ±0.042) which is comparable to the Red Shed dataset. Another source of error in the mosaics may be the fact that for the sake of efficiency and automation, we used a dense triangulation to rectify the images rather than a rigorous orthorectification that would typically be undertaken in a traditional aerial photogrammetric treatment of such imagery.

An experiment was undertaken to test the robustness of the GCP technique against a reduction in the number of GCPs available. From the 20 GCPs that were automatically detected in the Red Shed dataset, 10 were randomly selected such that they were evenly distributed throughout the study area. New Helmert transform parameters were then calculated based on only these 10 GCPs followed by image rectification and mosaicking. An accuracy assessment based on 63 GCPs gave a mean spatial error of 0.108 m (with a standard deviation of ± 0.063) which is similar to the error when using all 20 GCPs for the Helmert transformation.

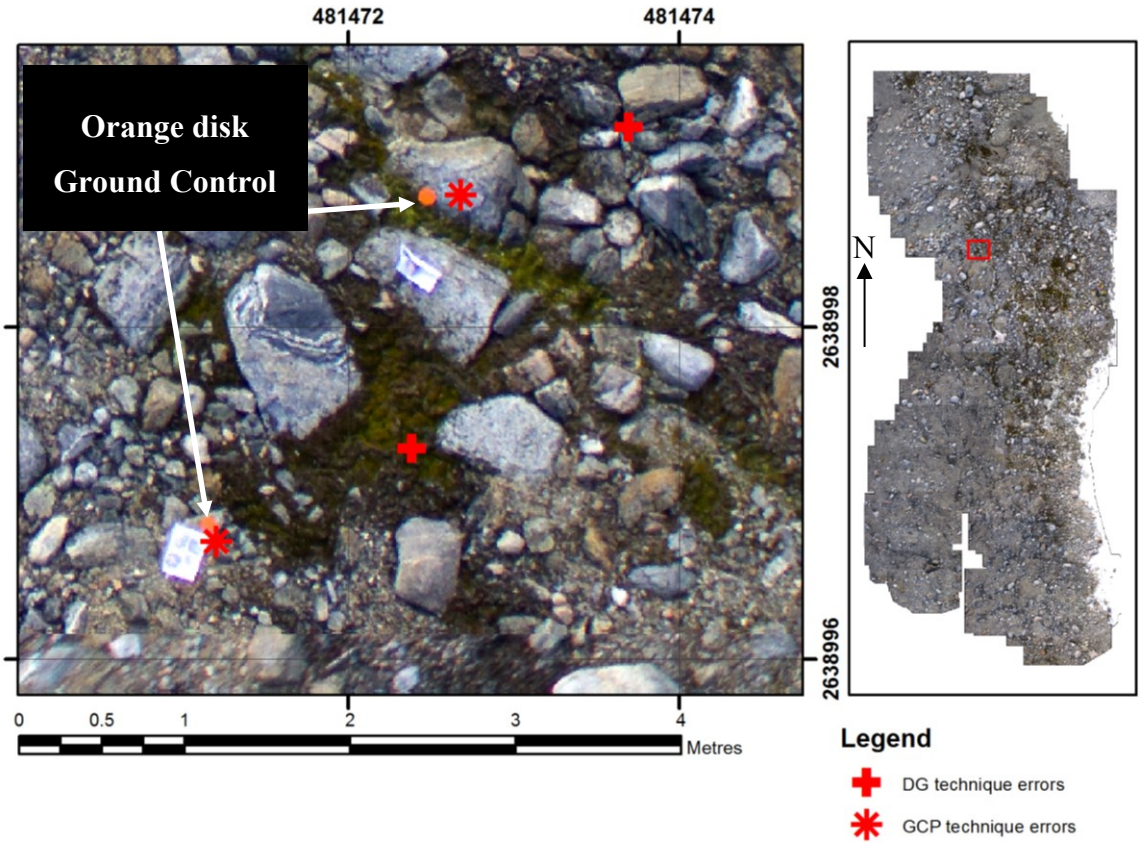

Figure 2.7 - Detailed section of an image mosaic of Robinson's Ridge showing typical spatial errors of direct and GCP techniques in relation to the actual GCPs (the small orange discs)

With the direct technique, a significant portion of this error is explained by the lack of precision in the measurements that it uses to generate the Helmert transform parameters. These camera location measurements were collected by a navigation-grade (single frequency) on-board GPS unit with no differential corrections and inaccurate time synchronisation between GPS and camera. The Robinson's Ridge dataset Helmert transform parameters had a higher precision than the Red Shed parameters but this was not reflected in the absolute spatial accuracy that was achieved for the two areas.

The absolute spatial accuracy of mosaics produced by our system is comparable to or exceeds the results achieved by others such as Laliberte *et al.* (2008) and Berni *et al.* (2009). However, our technique is fully automated, requiring no user intervention and is thus very time-efficient.

2.4 Conclusions

Unmanned Aerial Vehicles (UAVs) are increasingly used for environmental remote sensing applications. A large number of UAV aerial photographs are required to cover even relatively small study areas. The characteristics of UAV-based aerial photography has necessitated the development of new geometric image correction and mosaicking techniques. Our approach applies modern Computer Vision (CV) algorithms to ultra-high resolution UAV imagery so that 3D point clouds can be generated and subsequently used to georeference the imagery. The combination of a micro-UAV platform with our novel image processing techniques provides an inexpensive, automated, and accurate system for producing ultra-high resolution mosaics of a study area that by far exceeds the resolutions typically available from conventional platforms.

Imagery of moss beds in Antarctica was used to validate the spatial accuracy of our technique which can directly georeference the imagery or use Ground Control Points (GCPs) if they are available. Two datasets (one containing 200 images, the other 69 images) were processed with both techniques producing four mosaics. The directly georeferenced mosaics had a spatial accuracy of 65–120 cm with whilst the GCP technique achieved a spatial accuracy of 10–15 cm.

The primary source of error for the direct georeferencing technique is the fact that it relies on an inaccurate navigation grade GPS to record the camera position. A significant portion of this error could be removed with the addition of an on-board single/dual frequency carrier phase differential GPS. This could potentially eliminate the need for GCPs and greatly improve the efficiency of field surveys. A further improvement to the spatial accuracy of the mosaics could be achieved by applying a rigorous orthorectification rather than a Delaunay triangulation which is currently used. Investigation into the potential of these two improvements will be the subject of further research.

The technique presented in this study is applicable to other UAV surveys conducted over alternate surface types and terrains. The automated nature of our technique allows a large collection of ultra-high resolution UAV images to be quickly and efficiently transformed into a usable product for a range of subsequent analyses.

2.5 Thesis Context

This chapter addresses the first objective of the thesis focusing on georectifying and mosaicking the multiple images collected during an MUAV survey in an efficient, automated, and accurate manner. Chapter 2 also provided the background and context into why new techniques were required to achieve this task, demonstrating that existing photogrammetry software designed to process conventional aerial photography is not suitable for processing low altitude MUAV imagery. At the time of publication, commercial Structure from Motion (SfM) software, such as Agisoft Photoscan or Pix4D, was not available (or still under development) and there was a need to develop an image processing workflow for georectification and mosaicking of hundreds of images acquired during a typical MUAV survey.

Chapter 3

Direct Georeferencing of Ultra-high Resolution UAV Imagery

Chapter 3 describes a technique we developed to directly georeference UAV imagery and has been published in Transactions on Geoscience and remote sensing May 2014.

Turner, D., A. Lucieer and L. Wallace (2013). "Direct Georeferencing of Ultrahigh-Resolution UAV Imagery." IEEE Transactions on Geoscience and Remote Sensing **52**(5): 2738-2745.

Abstract

Micro Unmanned Aerial Vehicles (UAVs) often collect a large amount of images when mapping an area at an ultra-high resolution. A direct georeferencing technique potentially eliminates the need for ground control points. In this study, we developed a camera-GPS module to allow synchronisation of camera exposure with the airframe's position as recorded by a GPS with 10 – 20 cm accuracy. Lever arm corrections were applied to the camera positions to account for the positional difference between the GPS antenna and the camera centre. Image selection algorithms were implemented to eliminate blurry images and images with excessive overlap. This study compared three different software methods (Photoscan, Pix4D web service, and an in-house Bundler method). We evaluated each based on processing time, ease of use, and the spatial accuracy of final mosaic produced. Photoscan showed the best performance as it was the fastest, was easy to use, and had the best spatial accuracy (average error of 0.11 m with a standard deviation of 0.02 m). This accuracy is limited by the accuracy of the differential GPS unit (10 - 20 cm) used to record camera position. Pix4D achieved a mean spatial error of 0.24 m with a standard deviation of 0.03 m whilst the Bundler method had the worst mean spatial accuracy of 0.76 m with a standard deviation of 0.15 m. The lower performance of the Bundler method was due to its poor performance in estimating camera focal length, which in turn introduced large errors in the Z-axis for the translation equations.

3.1 Introduction

In recent years the use of civilian Unmanned Aerial Vehicles (UAVs) as remote sensing platforms (also known as Unmanned Aircraft Systems or UAS) has been increasing, primarily due to improvements in the availability of accurate and miniature Global Positioning Systems (GPS) and Inertial Measurement Units (IMUs), along with the availability of quality off-the-shelf consumer grade digital cameras (Nebiker *et al.*, 2008; Zhou *et al.*, 2009). In the realm of scientific research, the use of micro-UAVs, such as multi-rotor helicopters and small fixed-wing planes (typically below 5 kg total weight) is becoming more commonplace. This is the type of UAV on which this study is based. The ability of UAVs to acquire useful data for environmental remote sensing applications has been successfully demonstrated by Dunford *et al.*, (2009) who looked at riparian forests and Rango *et al.*, (2009) who mapped rangelands in New Mexico. In an agricultural context the applicability of UAVs has been demonstrated by authors such as Johnson *et al.*, (2003) who collected imagery over vineyards and Lelong *et al.*, (2008) who mapped the health of wheat crops.

The temporal resolution of UAV imagery is superior to imagery collected by satellite and conventional aerial photography platforms which are restricted due to limitations in the availability of aircraft, weather, and satellite orbits (Berni *et al.*, 2009). Flying at low altitudes (50 – 120 m AGL), UAV imagery also provides a superior spatial resolution (in the order of 1 cm/pixel) when compared to the resolution typically available from digital aerial photography platforms (25 cm/pixel) (Hunt *et al.*, 2010b).

Despite its advantages, the footprint of a micro-UAV system collecting imagery at 1 cm/pixel spatial resolution is of limited extent. To map a large area (greater than 2 ha for example) many images need to be collected and processed to create a useable product, such as a georectified image mosaic. Micro-UAVs are typically used as a cost-effective alternative to full-scale airborne surveys and it is therefore essential that the image processing routines are automated as much as possible such that image processing costs are also kept to a minimum whilst maintaining a suitable level of accuracy (Sauerbier *et al.*, 2011).

In recent years, there have been several methods developed to georectify and mosaic UAV imagery in a semi-automated fashion (Berni *et al.*, 2009; Bryson *et al.*, 2010; Laliberte *et al.*, 2010; Turner *et al.*, 2012). Many of these techniques, however, rely upon Ground Control Points (GCPs) or orientation measurements from an IMU to enable accurate georeferencing of the imagery. The collection of GCPs and the purchase of accurate miniature IMUs can be costly, not to mention they are often too heavy for micro-UAVs. Typically, low-cost UAVs only carry cost-effective sensors and thus the accuracy of position and orientation data is often limited (Bláha *et al.*, 2011).

Direct georeferencing is a technique that enables imagery to be georectified without the need for GCPs (Nagai *et al.*, 2004). This has advantages in terms of costs and the expertise required for accurate collection of GCPs (Verhoeven *et al.*, 2012). It also removes the need for human interaction to identify GCPs within the imagery, thus allowing a fully automatic processing chain to be implemented. Eugster and Nebiker (2007) presented a method to directly georeference a video stream collected from a UAV. Their method used on-board, low accuracy IMU/GPS data and projected the frames onto a pre-existing terrain model of the landscape. They reported a planimetric spatial accuracy of 0.7 m when flying at an altitude 50 m above ground level. Chiang *et al.* (2012) also implemented a direct georeferencing technique and achieved a planimetric accuracy of around 5 m when flying at 300 m. They proposed that this sort of system and accuracy would be suitable for near real-time disaster relief operations. Pfeifer *et al.* (2012) developed a system that processed raw, low quality data from gyros, accelerometers, and magnetometers to estimate camera position with a calculated planimetric accuracy of around 1 m when flying at 25 m. Turner *et al.* (2012) implemented a direct georeferencing technique that could achieve a planimetric accuracy of around 0.65-1.2 m when flying at 50 m. The limited accuracy of each of these techniques is primarily due to the low accuracy of the navigation grade GPS units used to record camera (airframe) position at the time of image capture. A second contributing factor to the relatively low accuracies is the imprecise time synchronisation between the camera acquisition and GPS receiver.

Another area of difficulty is identifying an appropriate software package to process ultra-high resolution UAV imagery. Traditional aerial photography image processing packages can have difficulty with UAV imagery given the different acquisition geometry parameters. In many cases, image blocks acquired from UAV imagery are more similar to close-range terrestrial image blocks (Remondino *et al.*, 2011; Turner *et al.*, 2012). Several authors (Barazzetti *et al.*, 2010a; Turner *et al.*, 2012) have demonstrated that modern Computer Vision (CV) and Structure from Motion (SfM) algorithms are well suited to processing of low altitude (below 300 m above ground level) UAV imagery. A discussion about the differences between traditional photogrammetry and low altitude ultra-high resolution UAV imagery can be found in Turner *et al.*, (2012) along with an explanation as to why modern CV and SfM algorithms work well with UAV imagery.

In this paper, we describe a UAV image collection system and processing workflow for efficient direct georeferencing in a fully automated fashion with high accuracy. We compare the direct georeferencing accuracy for three different methods: a) Photoscan (Agisoft, 2012), a commercial off the shelf (COTS) software package; b) a method developed in-house based on the Bundler SfM algorithms (Turner *et al.*, 2012); and c) the Pix4D web-based image processing service (Pix4D, 2012). We also discuss the limitations and advantages of each technique, explaining why they achieve different levels of accuracy.

3.2 Methodology

3.2.1 Platform

This study used a multi-rotor UAV made up of a Droidworx AD8 heavy lift airframe (www.droidworx.com.au) fitted with Mikrokopter (www.mikrokopter.com) electronics (see Figure 3.1). The UAV has eight rotors (an OktoKopter) and can lift a payload of up to 2 kg for a flight duration of 5 – 10 mins. The OktoKopter has a Photohigher AV130 stabilised camera mount (photohigher.co.nz) to which we have fitted a small format digital camera (Canon™ 550D DSLR, 18 Megapixel, 5184 x 3456 pixels, with Canon™ EF-S 18-55 mm F/3.5-5.6 IS lens). The Mikrokopter on-board electronics consist of a pressure sensor, accelerometers, gyroscopes, and magnetometers for attitude determination along with a navigation grade GPS (U-blox

LEA6S) for position determination. The on-board electronics are used to maintain level flight, control the altitude of the UAV, fly the UAV through a series of predefined three dimensional waypoints, and to log system information during the flight.

Figure 3.1 – Oktokopter in flight with Canon™ 550D fitted.

3.2.2 GPS logging system with camera sync

To accurately log airframe position information, a single frequency carrier phase Differential GPS (DGPS) unit (Novatel™ Flexpak-G2L with an OEMV-2 board) was modified such that it could be mounted to the OktoKopter. The GPS board was removed from its housing to reduce weight and a power management system was built. A single board computer (Gumstix™ Verdex Pro XM4-BT with netCF and console expansion cards) was used to log the GPS data during the flight (see Figure 3.2). Python scripts were implemented on the Gumstix™ computer that initialised the Novatel™ GPS, checked for sufficient satellite coverage, and configured the Novatel™ to log the required data streams: carrier phase range data at a rate of 20 Hz, camera exposure events, and updates to the ephemeris as they occur. During

the flight a Leica™ 1200 base station also collected static observations over a known point at 20 Hz. Combining the two data streams allows post processing to be carried out with the WayPoint Grafnav software (Novatel, 2012), calculating aircraft position every 0.05 seconds, with an accuracy of 10 – 20cm.

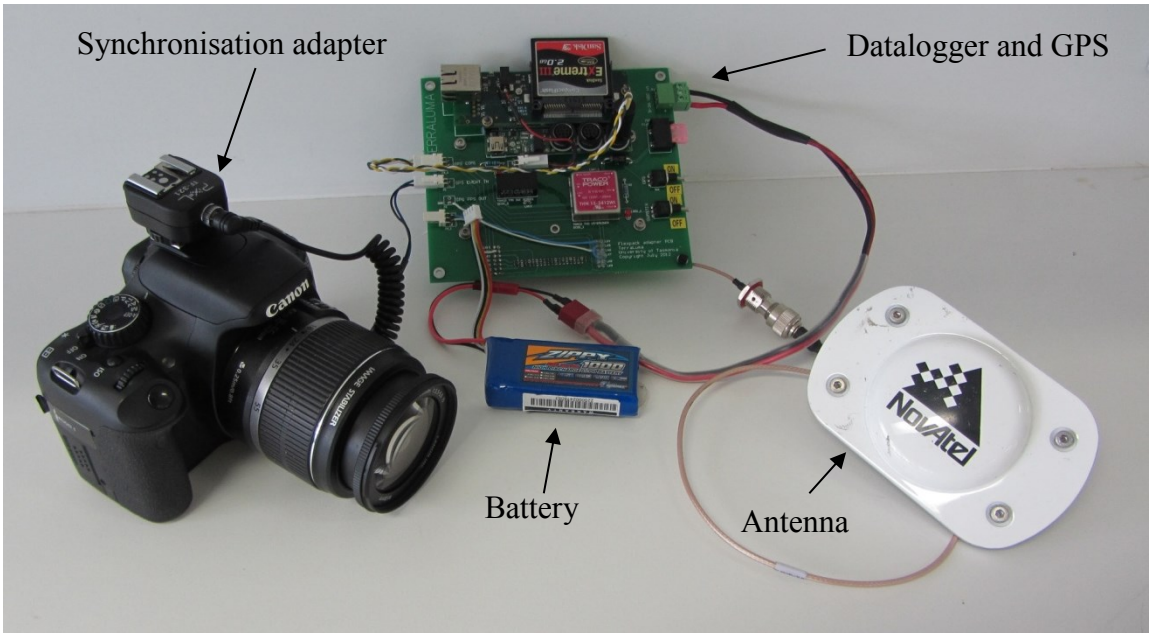

Figure 3.2 – Image capture and position determination system. Based on: Camera with synchronisation adapter, GPS with data logging board, battery, and GPS antenna.

The camera positions are then synchronised with the images collected and written to the appropriate image EXIF header such that they can be read by other software in later parts of the processing chain. To enable this synchronisation it is essential to accurately record the time of image capture. To achieve this we fitted a flash sync unit to the camera's hotshoe adapter which was then connected to the GPS unit (see Figure 3.2). When the camera shutter is opened, a pulse (normally requesting the flash to be fired) is sent to the GPS unit and subsequently time stamped in the GPS log file to a precision of 0.001 seconds. This allows the camera position to be interpolated between the 20 Hz post-processed positions from the data recorded in the log file.

The accuracy of this system is dependent on the delay between the shutter release request and the flash trigger pulse. The specifications of the Canon™ 550D state that the maximum (fastest) shutter speed allowable with flash is 1/200th second. This

means the longest that the delay between shutter and flash pulse can be is 0.005 second. At a maximum airframe speed of approximately 5 m/s we have a worst case scenario movement of 2.5 cm during the 0.005 second delay. This is far below the measurement accuracy of the GPS system (10 – 20 cm). As this is the worst case scenario with flying speeds typically only 2-3 m/s and the actual delay between shutter and pulse likely to be less than 0.005 second, the positional error caused by time synchronisation delays are insignificant when compared to the accuracy of the GPS measurements.

Once camera position has been determined from the GPS data we need to correct it to account for the lever arm between the camera centre (the centre of the CCD in this case) and the location of the GPS antenna. The location of the GPS antenna in relation to the camera is fixed, this meant we were able to simply measure the distances between the two locations in pitch, roll and yaw axes defined by the UAV's on-board low accuracy IMU. The approximate roll, pitch and yaw of the OktoKopter at each exposure time was then read from the on-board log file (recorded at 1 Hz and time stamped with GPS time) and used to determine the lever arm correction to be applied to the GPS position observation at each exposure station. As the IMU outputs are the result of the combination of measurements made by several sensors (gyros, accelerometers, and magnetometers) that are then Kalman filtered (with proprietary software), it is difficult to know the true accuracy of the IMU readings. We pessimistically assumed an error of ± 5 degrees and modelled the error. We found that the use of low accuracy orientation estimates to correct for the lever arm offset introduce errors of up to 4 cm. This is mainly due to the small physical offsets (x : 9 cm, y : 4 cm, z : 22 cm) between the camera and IMU, however, this correction still provides a significant improvement in the position estimate, which is reflected in the results (see Section 3.3.3).

3.2.3 Automated image selection

Imagery is collected at a rate of approximately one image every 1.5 seconds by the means of an automatic trigger that sends an alternating auto focus and shutter release command. A five minute flight can yield around 200 images and cover 1-2 ha of the earth's surface. To improve processing efficiency it is necessary to remove some of these images from the dataset. We have developed a series of algorithms that do this in an intelligent and automated fashion by applying a set of rules to the image set.

When examining the images captured during a flight we find there is generally a small amount (< 5%) of the images that have an unacceptable amount of motion blur. Blurry images have the potential to negatively affect the SfM process. We collect imagery with a high level of redundancy (approximated 90% overlap), so it is possible to exclude the blurry images from the dataset. To achieve this, we implemented an algorithm that calculates a blur metric for each image based on the method described by (Crete *et al.*, 2007). This method compares the magnitude of intensity variations between neighbouring pixels within an original image and this same image which has been deliberately blurred using a low-pass filter to evaluate blur annoyance in the form of a metric. By manually checking several test datasets we discovered that a threshold of 0.35 for the blur metric worked well to exclude the blurry, and thus unusable, images.

The automatic camera trigger commences operation as soon as the OktoKopter's motors are started. This means that there are a series of images captured whilst the UAV is climbing to operational altitude that do not need to be processed. Similarly, once the main part of the flight is complete the OktoKopter has to descend and land, during which time the camera continues to collect images until the motors are switched off. These unwanted images are removed from the dataset based on the flying height at time of capture as recorded in the image EXIF data.

During a flight over an area of interest the OktoKopter will move from one waypoint to the next, pausing briefly so that at least one image is collected at each waypoint. The waypoints are spaced such that the required overlap and sidelap between the images is achieved. However, as the camera has an automatic trigger, many images are captured during the transit between waypoints giving a high level of image redundancy. This necessitates the need to remove some of these overlapping images to improve processing efficiency, which is achieved by reading the image location information from image EXIF headers. Through experimentation and comparison with other research, such as Rosnell and Honkavaara (2012), we found that an image overlap of around 80% yields the best results for SfM based image processing algorithms. Image subsetting is achieved by computing the distance between consecutive images and if this distance is below a predefined threshold (i.e. the OktoKopter is relatively stationary) then this image is skipped and we move on to the

next image until the spacing between exposures achieves the desired level of overlap (80%).

3.2.4 Image processing

3.2.4.1 Photoscan

For this study we compared the performance of the Photoscan Professional (Agisoft, 2012) image processing software with the Pix4D (2012) web-based image processing service, and with an in-house technique we previously developed, based on Bundler, as detailed in Turner *et al.* (2012). To maintain the efficiency and cost effectiveness of our micro-UAV system it was essential that all the evaluated image processing workflows maximise automation capacity, thus reducing human intervention to enable creation of the desired products such as orthomosaics and Digital Surface Models (DSMs). Photoscan is a CV and SfM based software package that does not include some of the specific functionality that is available in professional photogrammetric software and is thus a more cost effective solution for processing low altitude UAV imagery.

After image selection, the Photoscan workflow starts with an image alignment stage that uses SfM techniques to reconstruct the three dimensional scene geometry based on feature points (based on SIFT) that have been detected within and matched across the images (Verhoeven, 2011). The image alignment step also estimates the camera positions and refines the seven camera calibration parameters (focal length, principal point, three radial and two tangential distortion coefficients). A high accuracy setting was used for the image alignment stage and image pair pre-selection was based on ground control. Photoscan has the ability to select photo pairs for feature matching based on potential overlap given approximate photo locations. Photoscan also allows the input of custom lens distortion parameters that can then be used to constrain the bundle adjustment.

The second processing stage is to build the scene geometry by applying a dense, multiview stereo reconstruction to the aligned images (Verhoeven, 2011). Detailed surface geometry is built from images that have been undistorted using the camera calibration parameters obtained during the alignment stage of processing. Photoscan

has a number of settings that the user needs to define for the geometry build phase. Through experimentation we found the optimal settings for geometry build to be a high target quality, object type was set to a height field, and geometry was set to smooth. Once the scene geometry has been built an orthophoto and a DSM of the area can be exported. All stages of the processing (except the initial selection of the images) can be run as a batch process, requiring no human interaction, thus in effect is a fully automated process.

Georeferencing of the images and 3D model is achieved by using on-board GPS coordinates attached to each image in the JPEG EXIF header. Generally, these on-board GPS coordinates have a low accuracy (2 – 5 m) due to the use of navigation-grade GPS receiver, and therefore more accurate Ground Control Points (GCPs) are used to optimise the bundle adjustment. In this study, GCPs are only used for accuracy assessment, instead the coordinates of the camera stations based on high accuracy GPS observations are used for georeferencing. Photoscan can use these coordinates in the bundle adjustment to produce accurately positioned orthomosaics and DSMs.

3.2.4.2 Bundler method

We have previously described a technique to georectify and mosaic ultra-high resolution UAV imagery in Turner *et al.* (2012). This technique is based on the Bundler SfM software package developed by Snavely (2010) to align the photos and estimate camera positions in a similar fashion to the first stage of the Photoscan process. In this study we developed an algorithm that uses the output of the Bundler process to georectify the individual images in a fully automated fashion. The final stage is to select the images to be merged into the final image mosaic.

3.2.4.3 Pix4D web service

The Pix4D service processes UAV imagery in a similar way to the already described software packages (Kung *et al.*, 2011), initially it searches for and matches points using the Scale Invariant Feature Transform (SIFT) algorithm (Lowe, 2005). The matches and the approximate locations of the cameras (as supplied by the user, typically in the image EXIF header) are used in a bundle block adjustment to

reconstruct the position and orientation of each camera (Kung *et al.*, 2011). The matched points can then have their 3D coordinate calculated and used to obtain a DSM which is in turn used to project every image pixel thus allowing a georeferenced orthomosaic to be generated (Kung *et al.*, 2011). However, as it is a web-based service, none of these steps are visible to the user who is only required to upload the images to be processed, await an initial processing evaluation accuracy report, select the products required, await final processing to complete, and download the results.

3.3 Results

3.3.1 Study Area used for testing

We tested our direct georeferencing system at Houston's lettuce farm in southeast Tasmania, Australia (see Figure 3.3) as part of a project to test the feasibility of using micro-UAVs to map and monitor the health of lettuce crops. Lettuce is a high value crop (worth ~AU$25,000 / hectare) that could greatly benefit from a micro-UAV's ability to rapidly monitor the crop's health, which can then inform management decisions on irrigation, fertilisation, and pest control. Our trial mapped a 0.8 hectare section of harvest-ready lettuce plants, the site slopes gently from an elevation of 65 m in the south-east to 55 m in the north-west. Before the images were collected, 22 GCPs were distributed in the central area of the study area. For the GCPs we used aluminium discs, 30 cm in diameter, with the outer rims painted with orange fluorescent paint. The centre location of each disc was then measured using a survey grade dual frequency differential GPS, with a typical accuracy of 2 cm in the horizontal and 4 cm in the vertical (relative to a local coordinated benchmark).

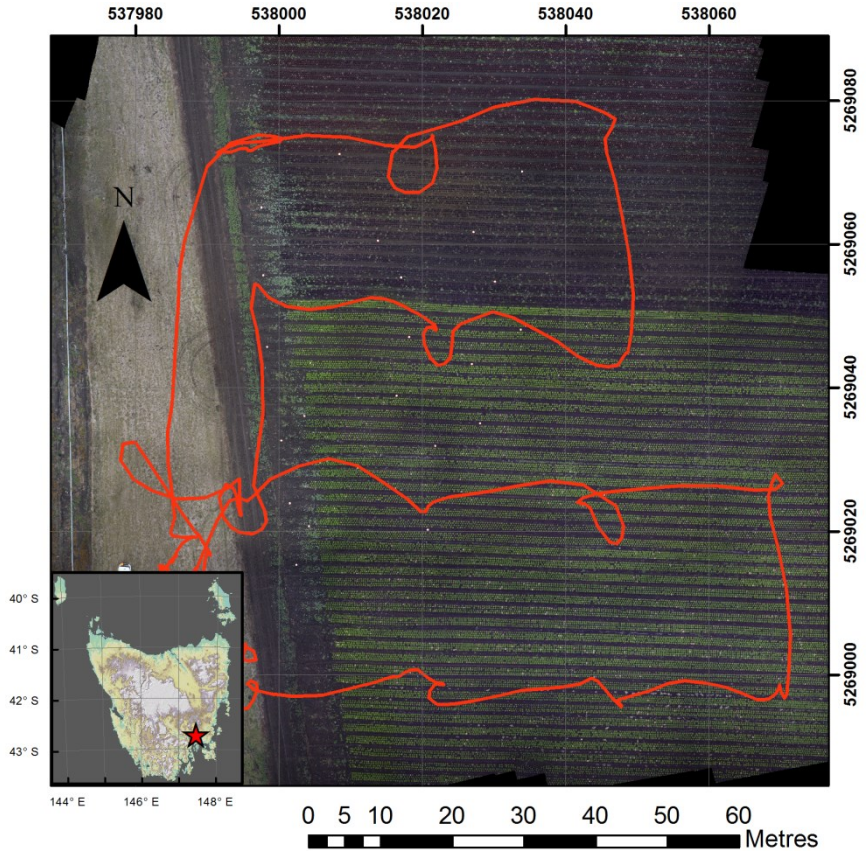

Figure 3.3 – Mosaic of study site with location map and UAV flight path overlaid (coordinate system: GDA94 UTM55S).

The flight was carried out on the 20th April 2012 in windy (10 – 15 knots) and overcast conditions and yielded 297 photos. The wind affected the flight and navigation stability of the OktoKopter resulting in the UAV circling around a waypoint before attaining it and moving on to the next (see Figure 3.3). This was a good test for automated image selection routines to remove some of the redundant photos captured during the circling. Of the 297 images that were captured by the platform, 143 were selected for processing by the image selection algorithms (see section 2.3), i.e. blurry images, images captured during ascent/descent, and images collected too close together were removed.

3.3.2 Processing time

Table 3.1 presents a comparison between the methods tested and the processing time required for the test dataset. Photoscan is faster than the Bundler technique, as it has been developed to make use of the Graphic Processing Units (GPUs) found on the

high-end graphics card installed in the desktop PC used for processing. In comparison, the Bundler technique only uses as single processor core at any one time, and runs considerably slower. The Pix4D software seems slower than Photoscan at first glance, however, when we take note that a majority of the time taken by Pix4D is during the image upload (7 hours) we can see that the actual processing times are quite similar. The data upload was carried out over a very fast (shared 10 Gigabit/second) connection, so there is nothing that can be done to improve this part of the process except perhaps reduce the quality of the images and thus reduce their file size and upload time. This may, however, have a negative impact on the quality of the final products. It should also be noted that if the user was in a remote area (e.g. carrying out fieldwork) with no, or limited, internet access, it would be very difficult to make use of the Pix4D service.

Table 3.1 – Summary of total processing time for 143 images with each method

Method	Photoscan	Bundler technique	Pix4D
Processing time	4.3 hours	41 hours	11 hours
Comments	Alignment 1.8 hr Geometry 1.8 hr Orthophoto 0.7 hr	Optimised technique reduced processing time to 16 hours	7 hours of total is time to upload image dataset
Hardware	Windows based, Quad core desktop PC (Intel i7 – 8 cores) with NVIDIA GTX590 graphics card and 32GB of RAM	Linux server with 256GB of RAM and 32 processor cores	Web-based cloud computing service

To address the long time taken by the Bundler technique (due to its single processor usage), some modifications to the processing chain were made. The first stage of the Bundler processing chain is to detect image features with the SIFT algorithm (Lowe, 2005) and then to match the features amongst the images. Neither of these processes, as they stand, makes use of the multiple processor cores. Siftfast (libsift, 2012) is an implementation of the SIFT algorithm that does use multiple cores and can also run SIFT on full resolution images whereas the conventional SIFT used by the Bundler software requires image resolution be reduced to a maximum of 2000 x 1500 pixels. The matching stage can take a long time as it has to match the

thousands of features (sometimes in the hundreds of thousands per image) found in each image with the features found in all the other images.

As we have prior knowledge of the camera positions, we can determine which images are likely to have a spatial overlap and thus likely to yield matches. There would be 10153 image pairs to be processed if all images were matched exhaustively, however, by removing the pairs that are unlikely to have any overlap this number was reduced to 1107 matches. These optimisations greatly speed up the feature detection and matching stages of the Bundler algorithm, reducing the total processing time by more than 50% in this example (see Table 3.1), however, the final stage of processing is a bundle adjustment that still only uses a single processor core and is therefore a processing speed constraint. Of the 15 hours taken to process the dataset with the optimised Bundler algorithm, 14 hours was spent on the bundle adjustment (single core) stage of processing.

As Pix4D is a cloud-based web service, processing times may vary depending on current demand on the system. However, with each of the methods, they are all really "set and forget" systems where the user will initiate processing and return to review the results the next day.

To assess the benefit of reducing the number of images to be processed by use of the automated image selection algorithm, the entire set of images was also processed. The Photoscan processing time increased to 8.6 hours, a doubling in processing time from a 63% increase in number of images. The Bundler method processing time increased to 115.5 hours, a 180% increase. A test with the full image set was not carried out with the Pix4D service as its major overhead is the data upload time required for the cloud computing. The increase in image processing time would not be significant in comparison to this increase in upload time (estimated at 10 hours).

3.3.3 Spatial Accuracy

The primary objective of this study is to produce spatially accurate, georeferenced mosaics of the area covered by a UAV flight. To assess the accuracy of each method we measured the offset between the mosaic and recorded locations of the GCPs (see Section 3.3.1 for description of GCPs). A summary of the errors for each

method is presented in Table 3.2 and a typical example of the error for each method is illustrated in Figure 3.4.

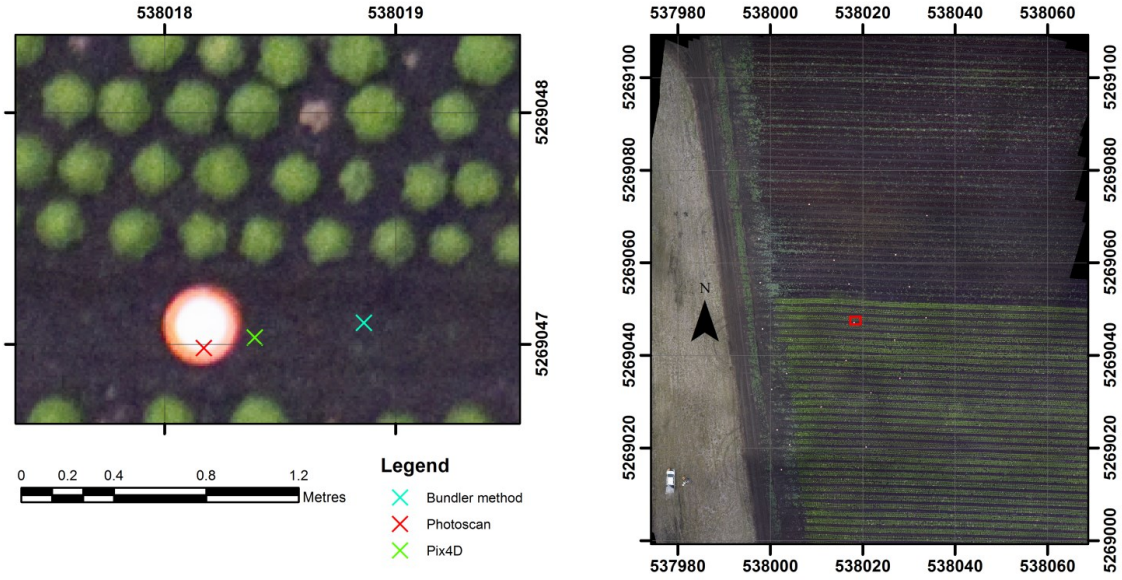

Figure 3.4 – Close up of one GCP showing the spatial error for each method (coordinate system: GDA94 UTM55S).

Table 3.2 – Summary of spatial errors for each method

Software	Mean absolute Easting error (m)	Mean absolute Northing error (m)	Mean absolute Total error (m)	Standard deviation of mean error (m)
Photoscan	0.0299	0.108	**0.1149**	0.0214
Pix4D web service	0.2371	0.0598	**0.2471**	0.0277
Bundler method	0.7381	0.1372	**0.7574**	0.1481

As discussed earlier, not all images were used for processing. It may be the case that using fewer images reduces the accuracy of the final image mosaic. To test this, we also ran all the images (excluding the ascent/descent images which were manually removed) through both the Photoscan and the Bundler software. The accuracy results for Photoscan were worse, with a mean absolute error of 0.2037 m (standard deviation 0.0285 m). The Bundler method was slightly better with a mean absolute

error of 0.68 m (standard deviation 0.16 m). However, the slight improvement achieved by the Bundler method was at great expense in terms of processing time (115.5 hours vs 16 hours previously, see Section 3.3.2).

The spatial accuracy achieved by these methods is proportional to the absolute accuracy of the GPS measurements of camera position at time of exposure. The on-board flight computer logs navigation-grade GPS positions during the flight. Post flight, it is possible to use this data to geotag the images with their position from the navigation log. Verhoeven *et al.* (2012) suggest that this type of GPS data can be used to georeference a Photoscan model, but they did not recommend it due to the inaccuracies in the GPS measurements. We processed the dataset using only these low quality GPS positions and found that both Photoscan and the Bundler method could only achieve a mean absolute error of 2.3 m (with standard deviation 0.22 m). This experiment validates that the quality of the GPS position data drives the spatial accuracy of the image mosaics and that a direct georeferencing technique based on high accuracy GPS observations with precise camera synchronisation is a valid endeavour.

It is also important to note the improvement to the results that the application of lever arm corrections yielded. To quantify this, we ran the same set of photos through Photoscan but we did not apply the lever arm correction to the camera positions. The mean error of this method was 0.19 m with a standard deviation of 0.024 m. This is a significant reduction in the accuracy compared to the results that included lever arm correction (around 42%). The lever arm correction is therefore an important part of the image processing workflow.

3.3.4 Helmert transformations

The Bundler method performs its bundle adjustment in an arbitrary coordinate system. We therefore rely on a seven parameter Helmert transformation (three translations, three rotations and one scale parameter) to transform the output into a real-world coordinate system (e.g. a projected Universal Transverse Mercator (UTM) easting and northing, and height). The Helmert transformation parameters and their associated uncertainties are estimated using a least squares approach, see Turner *et al.* (2012) for discussion on Helmert transformation in this context. It is also possible

to have Photoscan run in an arbitrary coordinate system by not supplying it with camera positions before processing commences, allowing us to compare how well each method was able to estimate the camera positions with no initial position input to the bundle adjustment. Table 3.3 shows that the formal errors for the Photoscan transformation are much smaller than the Bundler method, indicating that the Photoscan software has estimated the camera positions more accurately than the Bundler method.

Table 3.3 – Helmert transformation parameters with formal errors (1 sigma) from least squares solution

	Calculated Helmert transform parameters						
Software	**Translation X (m)**	**Translation Y (m)**	**Translation Z (m)**	**Scale Factor**	**Rotation X (º)**	**Rotation Y (º)**	**Rotation Z (º)**
Bundler	537994.538 ± 0.132	5269004.837 ± 0.128	92.807 ± 0.167	23.305 ± 0.055	169.805 ± 0.201	187.603 ± 0.187	269.554 ± 0.139
Photoscan	537999.43 ± 0.024	5269075.448 ± 0.024	92.016 ± 0.028	4.492 ± 0.002	357.555 ± 0.0326	187.9824 ± 0.032	282.8508 ± 0.023

3.4 Discussion

When considering processing time and spatial accuracy as metrics, it is clear that Photoscan is the best performer of the software methods tested in this study. Photoscan's spatial accuracy is comparable to the accuracy of the DGPS measurements used in the processing chain to georeference the imagery. The processing time was the fastest of the methods, although Pix4D would be comparable without the delay caused by image upload.

The spatial accuracy obtained by the Pix4D is good and would be sufficient for most purposes. As Pix4D is a web-based system we do not have intimate knowledge of the computing resources and processing algorithms used, and thus it is difficult to comment as to why the accuracy achieved is lower than that obtained by Photoscan. It could be hypothesised that the Pix4D processing chain has been developed around the user also supplying GCPs and has not been optimised for direct georeferencing.

The Bundler method did not perform well in either spatial accuracy or processing time, despite optimisations that were applied to the process. The difference in the

formal errors of the respective Helmert transformations (see Table 3.3) indicates where the greatest source of error may be found. The residuals of the Helmert transform for each of the x, y, and z translations indicate that the z translation residuals for the Bundler Helmert transform are very high in relation to all the other formal errors (average z residual for Bundler 1.27 m whilst only 0.07 m for Photoscan). Further analysis reveals that the errors in the z translation are related to the focal length that has been estimated by the Bundler method (see Figure 3.5).

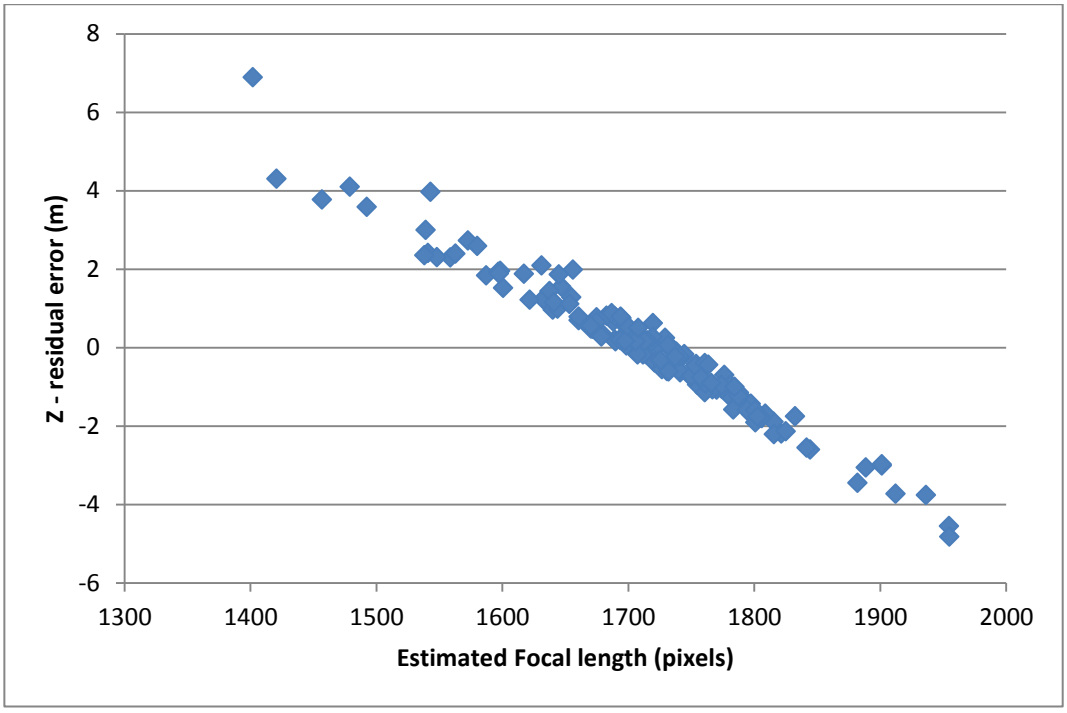

Figure 3.5 – Estimated focal length and Z Translation residual errors for Bundler processing method

A similar problem with Bundler was found by Rosnell and Honkavaara (2012) who discovered it was hard to get consistent camera calibration parameters when using Microsoft Photosynth™ (which is the web-based implementation of Bundler). In particular, Rosnell and Honkavaara (2012) found the focal lengths estimated by Photosynth™ (Bundler) to be highly variable and suggested that this was because Photosynth™ was designed to process each image as if it were from a different camera. Thus, Photosynth™ is more suited to photo tourism (Snavely *et al.*, 2008) and not ideal for applications using a single camera with a fixed focal length such as a UAV conducting an aerial mapping survey.

In comparison to Bundler, Photoscan estimates seven camera calibration parameters (see Section 3.2.4.1) as opposed to the three parameters estimated by Bundler (focal length and 2 radial distortion parameters). It would appear that Photoscan performs better than Bundler in this scenario as it is expecting images from the same camera and is thus better able to model the camera parameters. Bundler has some user-definable parameters to constrain or fix the focal estimates for the cameras. We carried out experiments to see if fixing or constraining the focal length could improve results, however, these tests were unsuccessful, generally resulting in the algorithm falling over or the resulting point cloud showing significant artefacts.

Although the Bundler method has the poorest spatial accuracy there is one advantage to this method in that it is possible to georeference each of the individual images. Photoscan is also able to georeference individual images. The output of the Pix4D software is a mosaic of all the images. There may be scenarios in which rectified individual images may be of use. It should also be noted that each of the three methods also produces a DSM as an additional product with the same spatial accuracy as the mosaics.

The bundler method suffers from poor processing speed due lack of parallelisation of the processing algorithms. Other implementations of the Bundler software are freely available and use multiple CPU cores to speed up processing times, namely SfM Toolkit (Astre, 2012) and VisualSfM (Wu, 2012). Trials with both of these programs revealed that they did not achieve any better results than the original Bundler, in fact the results were usually poorer. This may be due to the difference in implementation of the parallel SIFT and bundle adjustment algorithms and optimal settings of processing parameters. For this study we therefore decided to use the original Bundler implementation that we used in Turner *et al.* (2012).

There is also the option to process the data with professional photogrammetric software packages such as Leica™ Photogrammetry Suite (LPS) (Intergraph, 2012) or SOCET SET™ (BAE_SYSTEMS, 2012). Rosnell and Honkavaara (2012) processed low altitude UAV imagery with SOCET SET™, but discovered that it was not able to deal with the strong perspective distortions in the multi-view photography. Our tests with LPS revealed the same issues; it would seem that

traditional aerial photography software is not suited to processing low altitude aerial photography that has significant perspective distortions and very high overlap (Rosnell and Honkavaara, 2012). Verhoeven *et al.* (2012) highlighted some other limitations of LPS and similar packages, in that they require significant photogrammetric skills to operate, calibrated cameras, and high resolution DSMs.

3.5 Conclusions

Our study has demonstrated that it is possible to integrate an accurate direct georeferencing system onto a micro-UAV. The developed hardware components combined with current software, based on computer vision algorithms allows generation of accurate, directly georeferenced, ultra-high resolution orthophotos. The elimination of the need for GCPs simplifies the data collection process, making the use of UAVs more cost-effective and time-efficient. The absolute spatial accuracy of the mosaics created in this study (~0.11 m) was limited by the accuracy of the on-board DGPS measurement. The integration of a dual frequency (L1/L2) on-board GPS unit that should be able to measure the camera position with a higher accuracy (in the order of 2 – 5 cm) will be the subject of further research.

3.6 Thesis Context

This chapter addressed the second objective focusing on the reduction or removal of the need for GCPs for generation of orthophoto mosaics from MUAV surveys whilst retaining accuracy. It was demonstrated that it is possible to maintain accuracy without GCPs if the position of the camera at time of exposure can be accurately determined by way of DGPS and a system that allowed for accurate synchronisation between the camera exposure time and the DGPS position log.

Chapter 4

Spatial Co-Registration of Ultra-High Resolution Visible, Multispectral and Thermal Images Acquired with a Micro-UAV over Antarctic Moss Beds Co-registration

Chapter 4 describes a technique we developed to co-register UAV imagery datasets from three different sensors and has been published in Remote Sensing 2nd May 2014.

Turner, D., A. Lucieer, Z. Malenovský, D. King and S. Robinson (2014). "Spatial Co-Registration of Ultra-High Resolution Visible, Multispectral and Thermal Images Acquired with a Micro-UAV over Antarctic Moss Beds." Remote Sensing **6**(5): 4003-4024.

Abstract

In recent times, the use of Unmanned Aerial Vehicles (UAVs) as tools for environmental remote sensing has become more commonplace. Compared to traditional airborne remote sensing, UAVs can provide finer spatial resolution data (up to 1 cm/pixel) and higher temporal resolution data. For the purposes of vegetation monitoring, the use of multiple sensors such as near infrared and thermal infrared cameras are of benefit. Collecting data with multiple sensors, however, requires an accurate spatial co-registration of the various UAV image datasets. In this study, we used an Oktokopter UAV to investigate the physiological state of Antarctic moss ecosystems using three sensors: (i) a visible camera (1 cm/pixel), (ii) a 6 band multispectral camera (3 cm/pixel), and (iii) a thermal infrared camera (10 cm/pixel). Imagery from each sensor was georeferenced and mosaicked with a combination of commercially available software and our own algorithms based on the Scale Invariant Feature Transform (SIFT). The validation of the mosaic's spatial co-registration revealed a mean root mean squared error (RMSE) of 1.78 pixels. A thematic map of moss health, derived from the multispectral mosaic using a Modified Triangular Vegetation Index (MTVI2), and an indicative map of moss

surface temperature were then combined to demonstrate sufficient accuracy of our co-registration methodology for UAV-based monitoring of Antarctic moss beds.

4.1 Introduction

In recent times, the increased development and availability of micro and small-sized Unmanned Aerial Vehicle (UAV) platforms in combination with lightweight and low-cost Inertial Measurement Units (IMUs), GPS receivers, and scientific imaging sensors has driven a proliferation in the civilian use of UAVs. Small fixed wings, helicopters, and multi-rotor UAVs with a total weight of 5 kg or less (typically known as Micro-UAVs or MUAVs) are increasingly being used for scientific purposes, in areas such as photogrammetry and environmental remote sensing (Zhou *et al.*, 2009; Watts *et al.*, 2012). The use of UAVs for vegetation monitoring has been demonstrated by Dunford *et al.* (2009), who mapped riparian forests, and by Rango *et al.* (2009), who mapped rangelands in New Mexico. UAVs have also been proven to be useful for mapping agricultural crops, for example, mapping of vineyards (Johnson *et al.*, 2003), monitoring of wheat trials (Lelong *et al.*, 2008), and quantitative remote sensing of orchards and vineyards (Zarco-Tejada *et al.*, 2013; Berni *et al.*, 2009). However, research on the use of multiple sensors, which are expanding the remote sensing capabilities of UAV platforms, is rather limited. The use of multiple sensors presents unique challenges related, in particular, to the co-registration of the different image sensors.

UAVs offer particular advantages over other remote sensing platforms, especially if a fine spatial resolution (<10 cm/pixel) is required. In terms of agricultural crop monitoring or mapping of natural vegetation such as Antarctic moss, satellite imagery acquired at very high spatial resolution (e.g., pixel size ~0.5 m provided by sensors on-board platforms such as WorldView or GeoEye), often provide insufficient detail to monitor vegetation structure (Rufino and Moccia, 2005) and to extract detailed biophysical information, such as leaf size (Nebiker *et al.*, 2008) Although imaging systems carried by manned airborne platforms can provide high spatial and temporal resolution imagery, they are limited by high operational complexity and costs, particular in Antarctica and polar regions. UAVs can offer a cost-effective alternative to traditional airborne remote sensing, but it is essential that

techniques used to process the large amount of high spatial resolution data collected by a UAV are accurate and efficient.

Adequate spectral resolution is another key factor, particularly when monitoring vegetation, which exhibits great variability in magnitude of the near-infrared (NIR) reflectance. The lack of NIR reflectance information imposes limitations on vegetation characterization and thus a multispectral sensor that can capture data over several, preferably narrow, spectral bands is required (Laliberte *et al.*, 2011a). However, few lightweight multi-/hyper-spectral sensors suitable for UAV operations are currently available (Nebiker *et al.*, 2008), which limits research progress in this area. A typical approach to acquire NIR data from a small UAV is to modify a conventional digital camera by removing the infrared filter. As demonstrated by several studies (Hunt *et al.*, 2010a; Hunt *et al.*, 2008; Knoth *et al.*, 2013; Bryson *et al.*, 2013), a consumer-modified camera can collect useful Color Infrared (CIR) imagery. However, for detailed analysis of vegetation structural and biochemical parameters, narrow band multi- or hyper-spectral sensors are required. Kelcey and Lucieer (2012) described a correction workflow for reducing noise and optical distortion of the 6-band Tetracam multispectral sensor UAV image data, also used in this study. Berni *et al.* (2009) mapped olive orchards with a radiometrically calibrated multispectral sensor. They used images corrected for atmospheric effects to retrieve per-pixel leaf chlorophyll content and Leaf Area Index (LAI). Laliberte *et al.* (2011a) classified land cover types from atmospherically corrected multispectral imagery of rangelands in New Mexico using Object Based Image Analysis (OBIA) techniques. More recently, Zarco-Tejada *et al.* (2013) used calibrated and fully corrected multispectral imagery to estimate content of leaf carotenoid pigments of Spanish vineyards.

Satellite thermal imaging is currently limited to low spatial resolutions, for example 90 m per pixel from the TERRA-ASTER instrument (Yamaguchi *et al.*, 1998), a high spatial resolution assessment of vegetation moisture can be obtained from Thermal Infrared (TIR) imagery acquired from a UAV platform (Knoth *et al.*, 2013). Uncooled TIR sensors, based on microbolometer technology, are generally used on MUAVs, because they are smaller and have lower power consumption (Hu *et al.*, 2010). Unfortunately, uncooled sensors are less sensitive and have a lower

spectral resolution than their cooled counterparts (Hu *et al.*, 2010). They also require a specific spectral calibration and geometric characterization to retrieve the "true" ground surface temperature (Berni *et al.*, 2009). Despite these challenges, several studies have successfully used uncooled TIR sensors to map plant surface temperature for the purposes of crop monitoring (Bendig *et al.*, 2012; Hu *et al.*, 2010; Berni *et al.*, 2009).

As demonstrated by many studies cited above, there is a significant potential for UAV-based remote sensing of vegetation in the visible, near infrared, and thermal infrared region of the electromagnetic spectrum. A typical limitation in using current MUAVs for this purpose is, however, the ability to carry only one sensor at a time, due to the current lack of lightweight sensors, in particular sensors capable of measuring reflectance in the NIR. Imagery of visible, NIR and TIR wavelengths are, therefore, collected on separate flights (Hunt *et al.*, 2010a), which results in a requirement to spatially co-register the separate datasets. Berni *et al.* (2009), Bryson *et al.* (2013), and Bendig *et al.*, (2012) conducted their research using various multispectral and TIR sensors, but they did not discuss co-registration accuracy of their datasets. Although, Nagai *et al.* (2009) developed a method to co-register laser scanner data with data from visible and NIR cameras, most other UAV studies have focused on sensor calibration and correction (Berni *et al.*, 2009), correlation of multi-sensor data with biophysical properties of the vegetation (Zarco-Tejada *et al.*, 2013), or on object based classification of vegetation types (Laliberte and Rango, 2009)]. Therefore, the objective of this study is to present a workflow for spatial co-registration of visible, multispectral, and TIR imagery acquired at different ultra-high spatial resolutions during separate UAV flights. We describe technical specifications of the sensors used in this study, their image recording systems, and the multiple-image georectification and co-registration workflows.

To demonstrate the applicability and accuracy of our methodology we will present multi-sensor datasets collected over three moss study sites in Antarctica. Moss is the dominant form of vegetation in Antarctica, capable of preserving in their shoots up to a hundred-year long record of Antarctic climatic conditions (Clarke *et al.*, 2012). Despite Antarctica's sensitivity to climate change, there have only been few studies investigating the response of Antarctic vegetation to dynamic climatic conditions

(Convey *et al.*, 2009; Robinson *et al.*, 2003). There is, therefore, a need for mapping methods allowing detailed inventory and subsequent spatial monitoring of the changes in these vulnerable ecosystems. These Antarctic moss beds are spatially highly fragmented and cover only small areas (<1 ha). It is, therefore, practically impossible to map their extent with even the highest spatial resolution satellite imagery currently available (0.5 m/pixel). Moreover, local logistical obstacles limit the acquisition of conventional aerial photography in Antarctica, which may not provide the required spatial resolution (<10 cm/pixel). UAVs are an ideal platform from which image data of moss beds can be collected with sufficient spatial detail (Lucieer *et al.*, 2014).

4.2 Material and Methods

4.2.1 Test Sites

In Turner *et al.* (2012) we introduced a technique to georeference and mosaic multiple visible images collected by an MUAV. In the present study we are using two additional datasets of thermal and multispectral images, to demonstrate our multi-sensor spatial co-registration methodology. Input data were collected at three study sites in the Windmill Islands region, Antarctica (near the Australian base, Casey), where some of the most well-developed continental Antarctic vegetation is located.

The three study sites were named: Robinson Ridge, Red Shed, and Antarctic Specially Protected Area 135 (ASPA 135) (see Figure 4.1 for location overview). Robinson Ridge is located approximately 10 km south of Casey station, the Red Shed site is beside a melt lake behind the main accommodation building at Casey, and ASPA135 lies approximately 500 m east of Casey. Further description of all three test sites can be found in Turner *et al.* (2012) and in Lucieer *et al.* (2014).

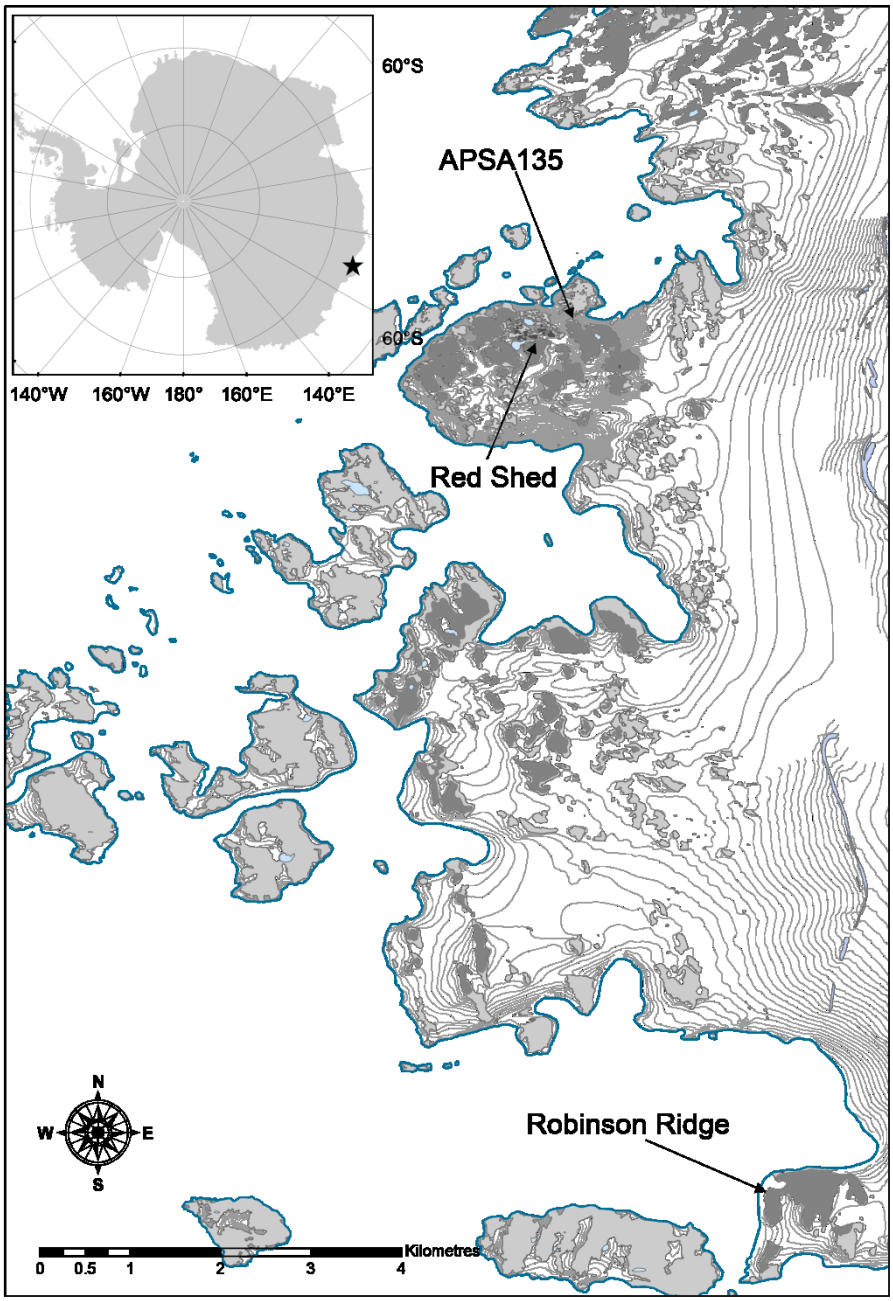

Figure 4.1 - Site location map for the three Antarctic test sites

4.2.2 Platform

Multi-rotor UAVs are becoming more commonplace and are frequently used for commercial and recreational aerial photography. For this study we used an eight rotor Mikrokopter Micro-UAV called an "Oktokopter" supplied by HiSystems (GmbH, www.mikrokopter.com, Germany) (see Figure 4.2). The Oktokopter had a payload capacity of around 1 kg, a flight duration of 5 min (with a typical payload),

and was equipped with a gimballed camera mount (*i.e.*, self-levelled during flight based on on-board gyroscopes that measure the roll and pitch of the airframe), to which we individually fitted each of the three sensors. The Mikrokopter flight electronic systems can be used to automatically maintain level flight, control the altitude, log system data, and to fly the UAV through a series of predefined, three-dimensional waypoints.

Figure 4.2 - Oktokopter fitted with FLIR Photon 320 Thermal Infrared camera with Ethernet module mounted below.

4.2.3 Visible Digital Camera

To collect visible imagery we used a Canon 550D Digital Single Lens Reflex (DSLR) camera (18 Megapixel, 5184 × 3456 pixels, with Canon EF-S 18-55 mm F/3.5-5.6 IS lens). The image capture rate was controlled by the UAV's flight control board, which was programmed to emit a pulse at a desired frequency. The flight control board was connected to a custom-made cable that triggered the remote shutter release of the camera. The Canon camera was operated in shutter priority mode (a fast shutter speed was required to minimize motion blur), in which the desired shutter speed (typically 1/1250–1/1600 sec) was set before flight and the exposure was adjusted automatically by varying the camera's aperture. Images were captured in RAW format and stored on the memory card in the camera for post-flight download.

4.2.4 Thermal Infrared Sensor

To collect TIR imagery we used a FLIR Photon 320 (FLIR Systems, Inc. the USA, www.flir.com) uncooled thermal sensor (see Figure 4.2). The Photon 320 had a 14 mm lens providing a 46° field of view and acquired image frames of

324 × 256 pixels as raw 14-bit Digital Numbers (DNs) at the rate of 9 Hz. Image frames from the camera were converted into ethernet data packets by the FLIR Ethernet module and this data was then stored on a Single Board Computer (SBC), a Gumstix Verdex Pro XM4-BT, equipped with netCF and console expansion cards. System time of the Gumstix SBC was set to GPS time prior to flight, so that the thermal data files could be synchronized with UAV GPS log files. The 9 Hz data rate was too fast for the data buses of the Gumstix SBC and thus images could only be collected at a rate of around 1 Hz, which was fast enough for our purposes and retained sufficient image overlap on ground.

After the flight, the raw image data was downloaded from the SBC memory card and processed with code written in the IDL/ENVI image-processing environment (Exelis Visual Information Solutions, Inc. USA, www.exelisvis.com) to extract the image frames from the captured data packets. Extracted images were stored as 16-bit ENVI single band files containing the original 14-bit raw DNs as collected by the TIR sensor. A set of JPEG quick look images were simultaneously generated allowing a visual check of image quality. As the DNs typically do not cover the full 14-bit dynamic range, a contrast stretch to the data had to be applied, so that subsequent image processing software was able to identify features within the images. To identify an appropriate stretch, we created a histogram of the DNs of all pixels in all images, chose an upper and lower threshold such that the full dynamic range of the scene was covered, and applied a linear stretch based on these minimum and maximum thresholds. The images were then stored as 16-bit TIFF files, keeping note of the thresholds used such that the pixel values could later be converted back to the original DNs. The DN-values in the thermal imagery represent at-sensor radiance. After mosaicking and co-registration the DN-values were converted to absolute temperature in °C based on an empirical line correction. Nineteen targets with similar emissivity (0.97 assumed for moss and dark rock) were marked with shiny aluminium disks. Due to the very low emissivity of shiny aluminium these targets were clearly visible in the thermal imagery. A temperature observation was collected with a thermal radiance gun (Digitech QM7226) in between two aluminium disks. A GPS coordinate was also recorded for these observations. Matching pixels were extracted from the thermal imagery and based on the matching reference temperatures a linear regression was calculated. With this empirical relationship we

converted the whole thermal mosaic into absolute temperature, assuming a constant emissivity of 0.97 (which is justifiable given our interest in the moss bed).

4.2.5 Multispectral Sensor

The multispectral sensor used in our study was a Tetracam (Tetracam, Inc. the USA) mini-MCA (Multiple Camera Array) with an array of six individual image channels. Each channel has its own Complementary Metal Oxide Semiconductor (CMOS) sensor that could acquire 10-bit image data at an image size of 1280 × 1024 pixels. It was possible to fit customized waveband pass filters to each lens, allowing the user to define the desirable spectral band configuration. The data sets collected for this study had 530, 550, 570, 670, 700 and 800 nm optical filters fitted, with a Full-Width at Half Maximum (FWHM) of 10 nm.

The mini-MCA could be set to a "burst" mode in which it captured images continually from the time the shutter release was first pressed, we used the maximum rate of 0.5 Hz. Each of the six arrays stored the images in a proprietary raw format onto individual compact flash memory cards. After the flight the image data was downloaded from the cards resulting in six files for each camera exposure. As with the TIR data, we designed processing code in the IDL/ENVI environment to read the raw format files and to merge the layers into a single six band, 16-bit (to store the 10-bit data) ENVI image file format. The next stage was to correct mini-MCA imagery for sensor noise and other image distortions. Detailed description of these corrections can be found in Kelcey and Lucieer (2012). In short, the following three corrections were applied: (i) noise reduction using dark current imagery, (ii) lens vignetting correction based on spatially dependent correction factors, and (iii) a Brown-Conrady model removed lens distortion (Kelcey and Lucieer, 2012).

Finally, the image bands had to be aligned, as the six mini-MCA camera lenses were spatially offset. Tetracam Inc. provides software and alignment equations to correct for these offsets, but similar to Laliberte *et al.* (2011a) we found this alignment correction inaccurate at our typical UAV flying heights. To improve the band misalignment, we developed our own technique based on detecting geometric features within the imagery with the Scale Invariant Feature Transform (SIFT) keypoint detector (Lowe, 2005). The alignment process considered the first spectral

band (Band 1) of each image to be the master and aligned the other bands to it by matching key points between the bands. SIFT was run on each band of an image to create a set of key files and a key matching algorithm was then run between Band 1 and each of the other bands. Extracting the *x*, *y* locations of the matching features allowed us to create a control point file that aligned a given band with Band 1, *i.e.*, there were five control point files for bands 2 to 6. The control points were applied to each band with a Delaunay triangulation combined with a nearest neighbor resampling in order to perform a non-linear local transformation for alignment with the first band. The band alignment was highly dependent on the distance between the camera and the imaged surface. Provided that this distance remained relatively constant (within ±5 m), the technique would create a set of alignment parameters applicable to the current dataset. Final inspection of the band alignment for objects with sharp edges in the images was found to be satisfactory. Moreover, the method had the added advantage of being fully automated.

4.2.6 Mosaicking of Visible Imagery

During a typical flight of our UAV the Canon camera collected around 200 images. It was therefore necessary to join the images into a single mosaic of the whole study area. The image mosaic also needed to be georeferenced, such that the imagery from the different sensors could be co-registered. There are various methods for mosaicking UAV imagery; e.g., Berni *et al.* (2009), Bryson *et al.* (2010), Laliberte *et al.* (2008), Turner *et al.* (2012), and Turner *et al.* (2014b). Recently, new commercial software packages for automatically georectifing UAV imagery have become available (a review of some of these packages can be found in Turner *et al.* (2014b). Based on our previous research results we selected Photoscan Professional by Agisoft (Agisoft LLC, Russia) to georectify and mosaic the visible UAV imagery.

An overview of the Structure-from-Motion (SfM) workflow in Photoscan software can be found in Lucieer *et al.* (2014). Prior to processing, the images were geotagged with their approximate location as recorded by the UAV's on-board navigation-grade GPS. The internal time of the camera was set to GPS time prior to flight to ensure that the images could be easily synchronized with the position data in the UAV GPS log file. The blurry images were then detected with an algorithm that calculates an

image blur metric according to Crete *et al.* (2007). A more detailed description of this image processing stage can be found in Turner *et al.* (2014b). In the final step images with excessive overlap are removed (Turner *et al.*, 2014b).

Once the set of images to be processed was finalized, they were imported into Photoscan, which then detected and matched thousands of features between the images. Using these matches it performed a bundle adjustment to estimate the camera positions, orientations, and lens calibration parameters. Based on this information, the geometry of the scene (in the form of a 3D model) was created by applying a dense, multiview stereo reconstruction to the aligned images. Once the 3D geometry of the scene was constructed, a Digital Surface Model (DSM) and an orthophoto mosaic could be exported (Lucieer *et al.*, 2014).

To improve the absolute spatial accuracy of the mosaics, we manually located Ground Control Points (GCPs) distributed within the imagery. The GCPs were 30 cm diameter metal disks with a bright orange rim that were laid out in the study area prior to flight and measured with Differential RTK GPS (DGPS) with a typical accuracy of 2 cm in the horizontal and 4 cm in the vertical direction (relative to a local coordinated benchmark). Similar to the large GCPs, between 20 and 45 smaller (10 cm diameter) orange metal disks were randomly laid out across the study area and also coordinated with a DGPS. These small GCPs were used later as check points to verify the accuracy of the georeferenced mosaics.

Photoscan provided a simple interface to mark the location of a GCP on the 3D model and its location was then automatically marked on all the images that covered that part of the model. The user then needed to manually verify and, if necessary, adjust the location of the GCP in each image. Although this process was time-consuming, taking from 2 to 4 h to mark about 20 GCPs in a dataset of 200 photographs, the significant improvement in spatial accuracy justified the work required.

4.2.7 Mosaicking of Thermal Infrared Images

Similarly to the visible camera, the TIR sensor could collect hundreds of images in a single flight and it also required selection of the best images from the acquired

dataset. The response time of the microbolometer in the FLIR Photon 320 is approximately 10 milliseconds (see www.flir.com), giving it an effective shutter speed of 1/100th of a second, resulting in motion blur in around 40% of the images. Blurriness was assessed with the algorithm described in Section 2.6 and images with a blur metric greater than 0.3 were automatically removed from the dataset (see Figure 4.3). TIR images were subsequently processed with Photoscan in a manner similar to the visible imagery.

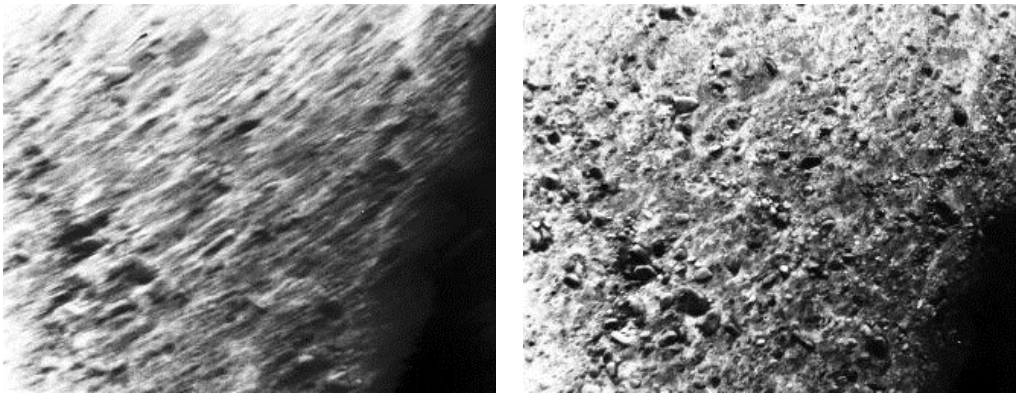

(**a**) (**b**)

Figure 4.3 - Comparison of two consecutive TIR frames; (a) blurry image with blur index of 0.32, and (b) sharp image with blur index of 0.22.

Photoscan was provided with initial estimations of camera position based on the time stamp of the image and the position as recorded in the on-board GPS log file. The TIR imagery was stored as a single band 16-bit file. Features in the images were enhanced with a linear contrast stretch, which was based on the minimum and maximum temperature DNs detected in the full scene (see Section 4.2.4). Once Photoscan had aligned the images, the GCPs needed to be identified within the imagery to allow accurate co-registration. It should be noted that only large aluminium trays (30 cm diameter) with an unpainted central part (see Figure 4.4b) were detectable in the lower resolution TIR imagery (10 cm/pixel for a typical UAV flight). The metallic aluminium surface of the trays with a low emissivity appeared as very cold (dark) pixels, which made the GCPs easy to visually identify. After the GCPs were marked, the scene's geometry was constructed, and an orthophoto was generated following the same approach as described in Section 4.2.6.

4.2.8 Mosaicking of Multispectral Images

Unlike the TIR and the visible imagery it was not possible to process the multispectral imagery with Photoscan. Although multi-band 16-bit images could be imported into Photoscan, it was not feasible to reliably align the images of different spectral bands, no matter what parameters were selected. The CMOS sensors in the mini-MCA have a rolling shutter, which built up each image as a scan from top to bottom rather than a whole-frame snapshot as in the case of a global shutter. Given the movements of the sensor during image acquisition the rolling shutter leads to geometric distortions in each image, which were unpredictable. The SfM algorithm in Photoscan expects images to be acquired by a global shutter. Thus, the distorted image geometry of the mini-MCA leads to very poor and false image matching results. Laliberte *et al.* (2010) developed a method for rectifying, georeferencing, and mosaicking UAV visible imagery by matching the individual images with a pre-existing orthophoto of the study area using image correlation techniques. This method served as the basis for our approach, however, we have implemented the SIFT algorithm as we did with the mini-MCA band alignment workflow (see Section 4.2.5). Instead of using a low-resolution orthophoto we matched each mini-MCA frame to the ultra-high spatial resolution visible orthophotomap (Section 4.2.6). This allowed SIFT to select thousands of features per image to be used as control points, providing a denser transformation matrix.

The mini-MCA collected a large number of overlapping images during flight. High overlap (80%–90%) is essential for the SfM algorithm, but for the mini-MCA imagery we only needed overlap of about 25%–30% to form a continuous mosaic. Therefore, the first processing step of the multispectral mosaicking workflow was determining an optimal subset of input images. The position of the airframe at the time of each image exposure, logged by the on-board GPS unit, is used to select the mini-MCA images based on their spatial distribution. Through process optimization we determined that a threshold of 7 m between the image positions achieved a mosaic with full coverage, but minimal seam lines. This selection reduced the number of images in a test dataset from 142 to 41, greatly reducing the number of seam lines within the final mosaic, whilst maintaining sufficient image overlap of around 25% (as determined via experimentation across all datasets). The blurriness

of mini-MCA images was verified in the same manner as the other two datasets. However, the blur factor of the mini-MCA images was, in general, so low that no images were excluded from the datasets.

Before we matched features in a mini-MCA image, we had to identify all the features in the visible orthophoto. To overcome limitations of the conventional SIFT algorithm implementation that usually runs only on low-resolution images, we implemented a SIFT distribution called "libsiftfast" (libsift, 2012), which uses multiple CPU cores and can process large images. As result, SIFT was able to detect 3,643,780 features in one of our 8690 × 17,215 pixels large visible mosaics. Since the SIFT algorithm runs per single image band, the six mini-MCA spectral bands supply more geometrical features for the matching process than the standard RGB imagery. From the millions of matches, there are often many false matches, which were removed with a Random Sample Consensus (RANSAC) algorithm developed by Fischler and Bolles (1981). In the application of the RANSAC algorithm we made the assumption that we were working with a projective model and that the epipolar constraints would hold despite the possibility of rolling shutter distortions within the imagery. To ensure these distortions did not affect the results we applied a low distance threshold (0.01 in normalized space), which reduced the number of resultant matches, whilst ensuring there were no false positives. We did not require a large number of matches as the remaining feature matches (post RANSAC) were not going to be used in an SfM context but were instead used to create control point files.

Using the feature matches, and the feature key files containing the locations of each feature in each image, we automatically created a series of dense GCP files for each mini-MCA image. This was facilitated by matching the known x, y coordinates of mini-MCA image features with their corresponding x, y coordinates in the RGB orthophoto, which were converted to easting and northing coordinates as the RGB mosaic was already georeferenced. The GCPs were then used in a Delaunay triangulation, which transformed a mini-MCA image using a nearest neighbour resampling algorithm into the same coordinate system as the visible and TIR mosaics. The pixel size of the resulting georeferenced image was set based on the flying height during the image acquisition (3 cm/pixel for our test datasets). Finally, all the images were merged into a georeferenced mosaic with the IDL/ENVI

mosaicking routine using a feathering of the seam lines to smooth the original image edges.

4.2.9 Calculating MTVI2 from Multispectral Data

Raw images of the mini-MCA, recorded as 10-bit digital counts with maximal signal strength equal to 1024 DNs, were transformed into the physically meaningful relative reflectance by applying an empirical line correction (Smith and Milton, 1999). Three spectrally flat calibration panels (40 × 40 cm) of white, grey, and black colour with reflectance intensities ranging from 2 up to 80% were placed within the UAV flight path and captured in the mini-MCA imagery. The target's actual DN values (approx. 130–140 pixels per panel) were extracted from the airborne image and empirically related to their reflectance functions measured with a spectrally calibrated ASD HandHeld2 (HH2) spectroradiometer (Analytical Spectral Devices, PANalytical Boulder USA) on the ground immediately after completion of the mini-MCA acquisition. The absolute reflectance of the calibration targets measured with the ASD-HH2 between 325 and 1075 nm (751 spectral bands of 1 nm bandwidth) were spectrally convolved to resemble the six broader spectral bands of the mini-MCA instrument with FWHM of 10 nm. The empirical line correction coefficients established between the convoluted ASD-HH2 and the six acquired mini-MCA spectral bands were then applied per pixel to the mini-MCA image mosaic to remove optical attenuation caused by scattering and absorption processes of atmospheric gases and aerosols between the sensor and observed surfaces and to standardize the multispectral signal as the relative reflectance function.

An efficient way of detecting photosynthetically active vegetation in multispectral imagery and assessing its actual physiological state is to transform the relative reflectance function into an optical vegetation index. The Modified Triangular Vegetation Index 2 (MTVI2) was originally introduced by Haboudane *et al.* (2004) to estimate green biomass density of spatially homogeneous agricultural crops. It is computed as:

$$MTVI2 = \frac{1.5(1.2(\rho_{800} - \rho_{550}) - 2.5(\rho_{670} - \rho_{550}))}{\sqrt{(2\rho_{800} + 1)^2 - \left(6\rho_{800} - 5\sqrt{\rho_{670}}\right) - 0.5}} \quad (1)$$

where ρ_{550}, ρ_{670} and ρ_{800} are the reflectance values at 550, 670 and 800 nm. As a successor of the Triangular Vegetation Index (Broge and Leblanc, 2000), MTVI2 integrates an area delineated by the reflectance at 550, 670 and 800 nm, which is influenced by the changes in leaf and canopy structure, normalized by a soil adjustment factor that reduces the contamination effect of the bare soil background.

Being stressed by insufficient water supply and high photosynthetically active and ultraviolet irradiation, Antarctic moss turf can, within few days, change in compactness and pigmentation. Over days to weeks it changes from a healthy, green open-leaved form to a stress-resisting denser, yellow-brown or red closed packed turf. If dry periods persist over longer periods (months to years) the turf will lose photosynthetic pigments, forming grey-black mounds of moribund (dormant/dead) moss. Since these physiological stress reactions systematically alter the moss reflectance at the wavelengths of 550, 670 and 800 nm, we could apply MTVI2 to separate photosynthetically active moss (health > 60%) from moribund moss, lichens, and the rocky surroundings.

For assessment of the ability of the MTVI2 index to determine moss health, the Robinson Ridge MTVI2 results were compared with field samples from the 2012 field season collected as part of a long term monitoring system for Australian State of the Environment Indicator 72 (SoE 72). Established in 2003, this monitoring system comprises a set of 30 permanent quadrat locations, across 10 transects spanning a water gradient across three community types: from the wettest community dominated by mosses (Bryophyte community) to the driest community dominated by moribund moss encrusted with lichens (Lichen community), with a Transitional community between (Wasley *et al.*, 2012). For each quadrat, the percentage of live bryophytes was evaluated from 9 small samples, each containing approximately 20–50 moss shoots, at 9 intersections within a 20 × 20 cm grid. For a more detailed description of moss ground monitoring see Wasley *et al.* (2012) and Lucieer *et al.* (2014) and for a description of spectral properites of Antarctic moss see Lovelock and Robinson (2002). To replicate the ground based sampling scheme, a grid of 3 × 3 pixels was extracted from the MTVI2 map and averaged per sampled quadrat.

4.2.10 Accuracy Assessment

To achieve the best possible co-registration of the three different datasets, it was essential that each of the mosaics was georeferenced with the highest spatial accuracy possible. For the RGB orthomosaics we, therefore, measured the positional error of all small orange disk check points that were measured with DGPS, but not used by Photoscan to georeference the mosaics. These disks were, unfortunately, too small to be visible in the TIR imagery and to be accurately identified in the mini-MCA imagery. For these two datasets the larger GCPs were used as check points. The Root Mean Square Error (RMSE) was computed between check point coordinates measured in the field with DGPS and coordinates retrieved from georeferenced image mosaics to assess the overall spatial accuracy of each dataset.

4.3 Results

4.3.1 Image Mosaics

The three tests sites were flown with our manually navigated Micro-UAV on three separate days. Manual navigation was required due to failure of autopilot navigation, which was caused by the extreme magnetic declination of Eastern Antarctica (~100° West). A basic description of the acquired datasets is provided in Table 4.1. Flights were all carried out in good solar illumination conditions, light winds, and at an altitude of approximately 50 m Above Ground Level (AGL). Despite flying at the same height AGL during each UAV mission, the resulting image mosaics have different spatial extents and different spatial resolutions caused by differences in the technical parameters of each sensor.

Table 4.1 - Details of acquired image datasets collected at each test site.

Site	Type	Date and Time Collected (Local: UTC+10)	Number of Images Collected	Spatial Resolution	GCPs
Robinson Ridge	RGB	24-FEB-2011, 2:45 pm	200	1 cm/pixel	62
Red Shed	RGB	20-FEB-2011, 1:33 pm	240	1 cm/pixel	57
ASPA 135	RGB	21-FEB-2011, 2:52 pm	256	1 cm/pixel	65
Robinson Ridge	mini-MCA	24-FEB-2011, 3:48 pm	148	3 cm/pixel	62
Red Shed	mini-MCA	20-FEB-2011, 3:00 pm	168	3 cm/pixel	57
ASPA 135	mini-MCA	21-FEB-2011, 4:13 pm	158	3 cm/pixel	65
Robinson Ridge	TIR	24-FEB-2011, 5:40 pm	424	10 cm/pixel	62
Red Shed	TIR	20-FEB-2011, 3:42 pm	571	10 cm/pixel	57
ASPA 135	TIR	21-FEB-2011, 5:20 pm	508	10 cm/pixel	65

Applying the methods described in Section 4.2, we created georeferenced mosaics for each of the nine flights. An example of a visible mosaic from the Robinson Ridge site is shown in Figure 4.4a. Figure 4.4b illustrates the detail that can be seen in this RGB imagery with a pixel size of 1 cm. The same spatial subsets of the lower resolution thermal infrared mosaic (10 cm/pixel) and of the false colour multispectral mosaic (3 cm/pixel) are shown in Figure 4.4c,d, and finally Figure 4.4e gives an example of a typical spectral signature for the healthy moss.

Using the methods described in Section 4.2.10, the spatial accuracy of each orthomosaic was measured and a summary of the spatial errors and RMSE is provided in Table 4.2. The RMSE ranges in general from 1 to 2.6 pixels, which means that all the mosaics exhibit a comparable level of spatial accuracy. The ASPA135 visible mosaic has the lowest RMSE, which can be attributed to the fact that it is a relatively small site with limited geomorphological variability, whereas the other two test sites are larger in spatial extent and have more diverse terrain morphology.

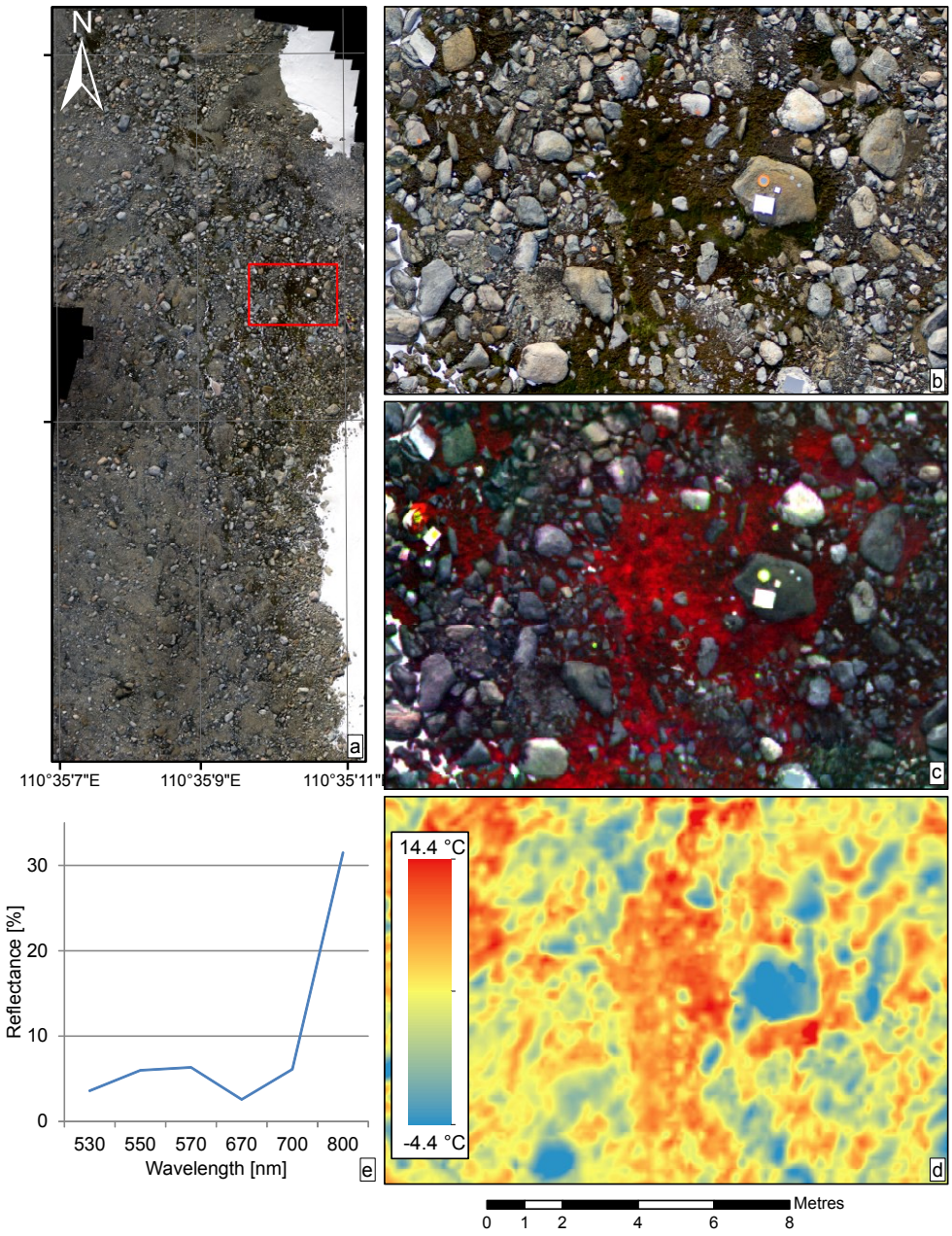

Figure 4.4 - Robinson Ridge study site: (a) visible mosaic of entire area, (b) RGB image subset, (c) multispectral image subset, (d) thermal infrared image subset, and (e) typical multi-spectral reflectance function of a healthy Antarctic moss turf.

Table 4.2 - Spatial accuracy of orthomosaics for each sensor as measured against check points.

Site	Type	Minimum Error (pixel/cm)	Maximum Error (pixel/cm)	Standard Deviation (pixel/cm)	RMSE (pixel/cm)	Number of Check Points	Number of GCPs Used
Robinson Ridge	Visible (1 cm/pixel)	0.72/0.72	4.65/4.65	1.15/1.15	**2.63**/2.63	25	12
Red Shed	Visible (1 cm/pixel)	0.46/0.46	3.71/3/71	0.82/0.82	**2.04**/2.04	41	24
ASPA 135	Visible (1 cm/pixel)	0.00/0.00	2.09/2.09	0.58/0.58	**0.95**/0.95	39	15
Robinson Ridge	mini-MCA (3 cm/pixel)	0.97/2.91	3.27/9.81	0.74/2.22	**2.14**/6.42	13	-
Red Shed	mini-MCA (3 cm/pixel)	0.87/2.61	3.95/11.85	0.99/2.97	**2.43**/7.29	19	-
ASPA 135	mini-MCA (3 cm/pixel)	0.98/2.94	3.54/10.62	0.63/1.89	**1.87**/5.61	12	-
Robinson Ridge	TIR (10 cm/pixel)	0.84/8.4	3.84/38.4	0.84/8.4	**1.83**/18.3	11	14
Red Shed	TIR (10 cm/pixel)	0.75/7.5	2.30/23.0	0.38/3.8	**1.48**/14.8	24	24
ASPA 135	TIR (10 cm/pixel)	1.90/19.0	4.04/40.4	0.76/7.6	**2.03**/20.3	19	14

4.3.2 Co-Registration Accuracy

Large GCPs were used as cross-comparison check points for the co-registration accuracy assessment, since they were the only features clearly identifiable in all three datasets. The location of the comparison points in the visible mosaic was considered to be the reference position. The co-registration errors of these GCPs in the mini-MCA and TIR mosaics are summarized in Table 4.3. The RMSEs are generally around 2 pixels, which matches the absolute RMSE that was obtained for all the mosaics listed in Table 4.2.

Table 4.3 - Co-registration accuracy of mini-Multi Camera Array (mini-MCA) and Thermal Infrared (TIR) mosaics as compared to the visible mosaic.

Site	Mini-MCA Mosaic		TIR Mosaic		Number of Compare Points
	Standard Deviation (pixel/cm)	RMSE (pixel/cm)	Standard Deviation (pixel/cm)	RMSE (pixel/cm)	
Robinson Ridge	0.71/2.13	**1.88**/5.64	0.81/8.1	**1.66**/16.6	10
Red Shed	0.94/2.82	**1.75**/5.25	0.39/3.9	**1.30**/13.0	15
ASPA 135	0.76/2.28	**2.15**/6.45	0.88/8.8	**1.98**/19.8	12

4.3.3 Assessing Health of Antarctic Moss from Multisprectral Imagery

To demonstrate sufficient spatial accuracy of these geocoded mosaics and the ability of the multispectral imagery to assess the actual health state of Antarctic mosses, we computed the MTVI2 optical vegetation index from the mini-MCA imagery collected at the Robinson Ridge test site (see Section 4.2.9). The Robinson Ridge data was selected as the most suitable of the three available datasets, because it has the least snow cover, it was acquired under optimal light conditions (bright, but diffuse irradiation), and ground observations of actual moss health are available for this site. Since reflectance signatures of stressed mosses and agro-systems with low leaf density (*i.e.*, low leaf area index) are spectrally similar, we could apply MTVI2 to assess the spatial distribution of the health state of moss bed at Robinson Ridge.

Comparing the moss health measured in summer 2012 and mean MTVI2 values derived from the mini-MCA mosaic we found a strong quadratic relationship between the two (see Figure 4.5). MTVI2 is insensitive to moss health in the driest lichen community quadrats due to the low abundance of photosynthetically active moss. MTVI2 does, however, show a statistically significant positive relationship for quadrats with a significant and/or dominant presence of bryophytes ($R^2 = 0.636$). Such a strong correlation provides evidence of a good co-registration agreement between mini-MCA and DGPS localization of quadrats and georectification of the mini-MCA image mosaic.

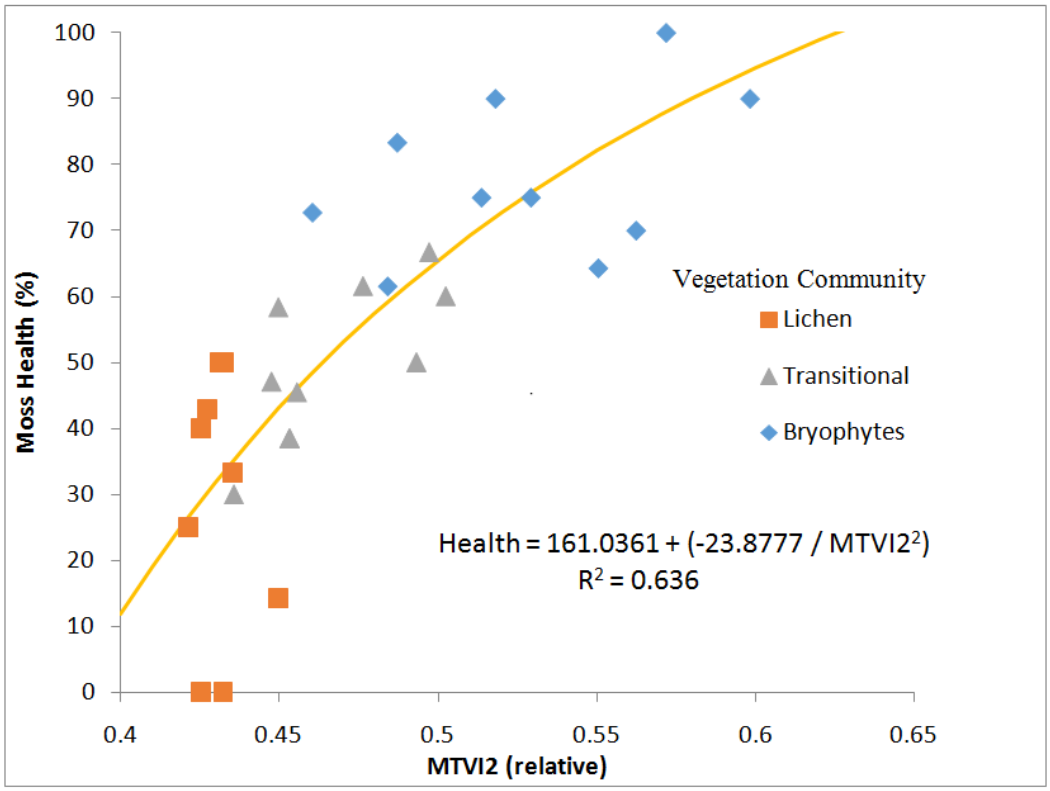

Figure 4.5 - Statistical relationship between the ground-measured moss health and the MTVI2 index computed from mosaic of multispectral mini-MCA images obtained at Robinson Ridge test site.

The statistical relationship shown in Figure 4.5 allowed us to approximate per-pixel moss health of the whole moss bed captured in the mini-MCA mosaic. Unfortunately, a considerable number of erroneous pixels were identified after a close inspection of the moss health map. These were caused, for instance, by high sensor noise combined with low light in shadows that produced incorrect spectral signatures of rock surfaces, mimicking high MTVI2 values of healthy moss. To prevent false moss health estimates, we applied the following rules: (i) the calculated per-pixel value of the Normalized Difference Vegetation Index (NDVI) must always be positive, (ii) the reflectance value of the 800 nm spectral band must be positive and greater than the reflectance in the shorter wavelengths, *i.e.*, at 550, 570 and 700 nm, and finally (iii) to eliminate negative estimates, moss health is assessed only if the MTVI2 value is greater than 0.4. The final map of moss health with these rules applied is displayed in Figure 4.6b.

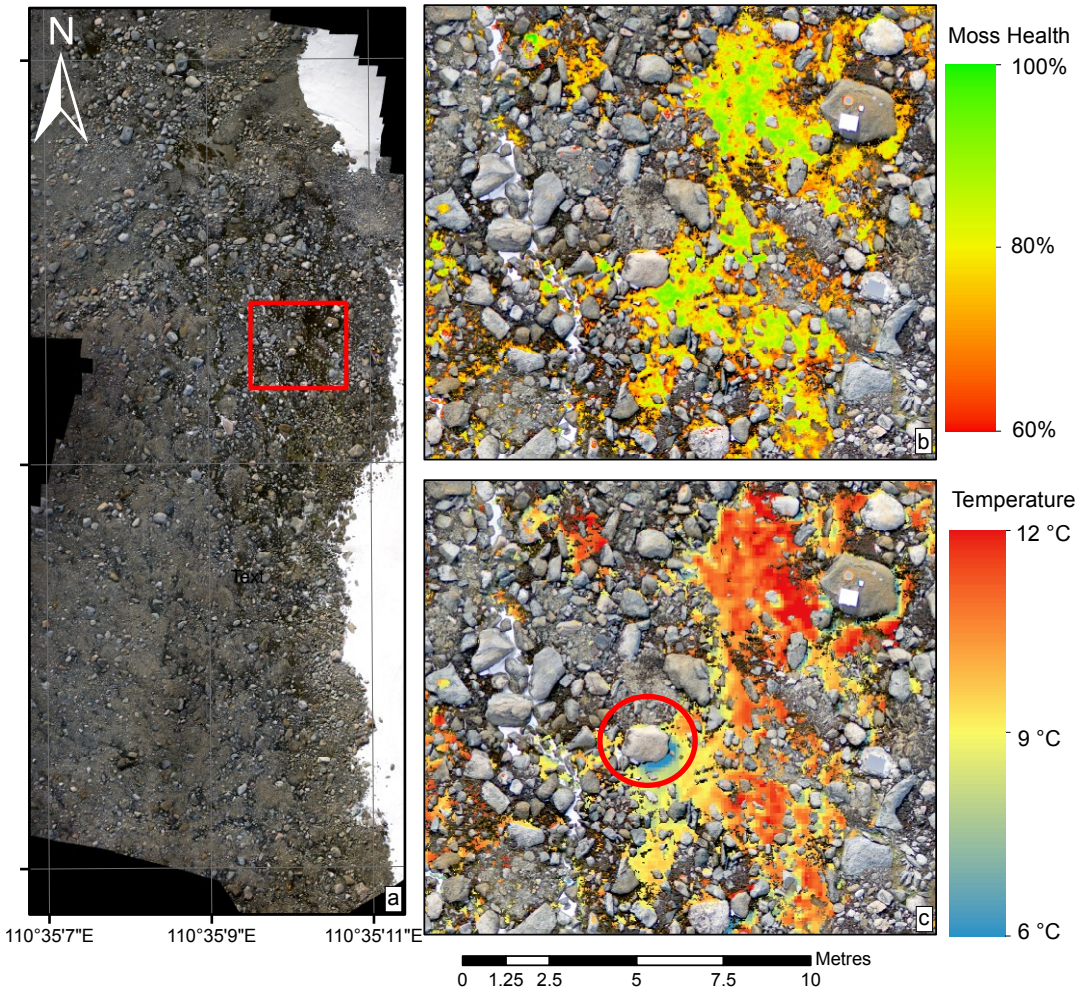

Figure 4.6 - Spatially co-registered thematic maps; (a) Overview; (b) Moss health derived from MTVI2 vegetation index and (c) Moss surface temperature at ultra-high spatial resolution (a red circle highlights thermal shadow cast by a large boulder).

4.3.4 Assessing Temperature of Healthy Moss from Thermal Infrared Image Mosaic

Simultaneously with the UAV flight over the Robinson Ridge study site, ground measurements of surface temperature were carried out with a handheld infrared thermometer at various locations recorded with DGPS. The corresponding DN value at each of the ground sample points was extracted from the georeferenced TIR mosaic and compared to the ground temperature measurements. A strong linear relationship established between both datasets was used to convert the TIR DN values to indicative surface temperatures (see Figure 4.7), providing a map of indicative surface temperature for the whole study site. Applying the moss health

map as a mask for the TIR imagery produced the surface temperature map of only moss pixels. The resulting surface temperature map of moss with a relative health score greater than 60% is shown in Figure 4.6c.

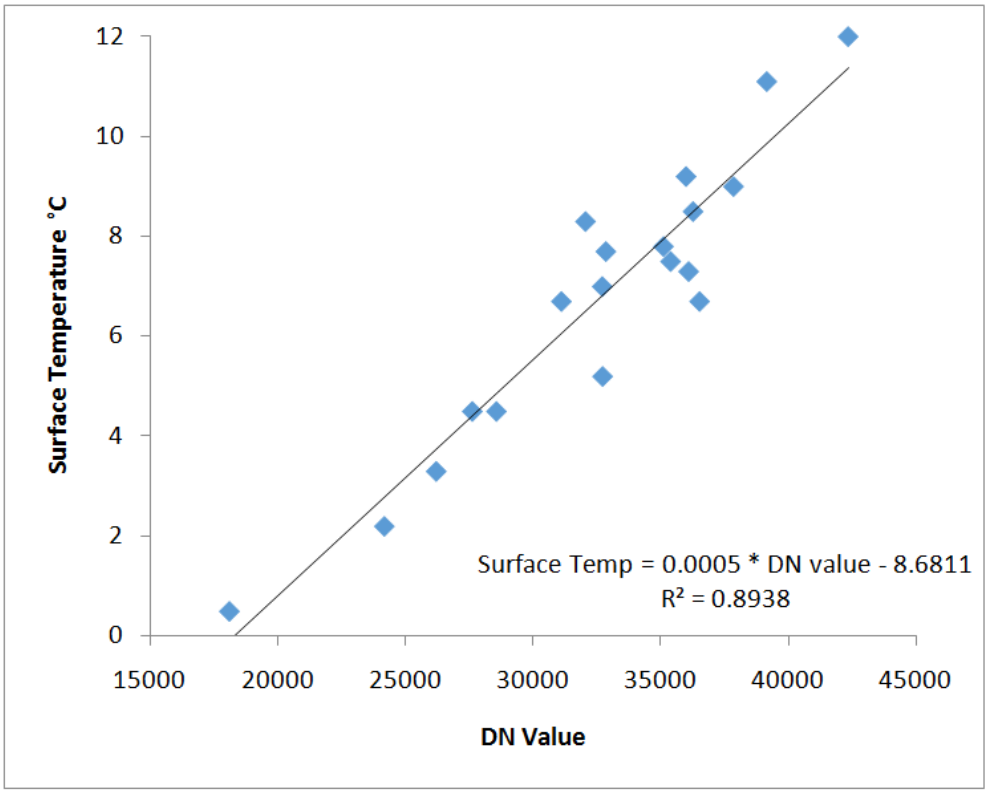

Figure 4.7 - Statistical relationship between thermal infrared DN values from UAV imagery and ground measured surface temperature for 19 sample points at the Robinson Ridge test site.

4.4 Discussion

The primary aim of this study is to demonstrate that our image co-registration workflow is able to produce sufficiently accurate georectified mosaics from images collected by three sensors during three separate flights at ultra-high spatial resolution (1–10 cm/pixel). It is important to note that each mosaic is produced with its own fully independent workflow and that none of them has been cross adjusted to improve the co-registration result. The mean accuracy of the co-registration (1.78 pixels) is regarded as satisfactory and acceptable for mapping of Antarctic moss beds, as verified by the statistically significant agreement with moss health ground observations (Figure 4.5). Unfortunately, there are currently no similar studies of co-registration of UAV imagery, to which our results could be compared.

Nevertheless, the thematic maps of moss health and moss surface temperature could only be created because of accurate co-registration of the three independent datasets.

The actual moss health map does not provide estimates below 60% (Figure 4.6b), which is mostly populated by desiccated (or moribund) plants. The spectral signature of such moss is similar to signatures of surrounding rocks and bare soil in the area, therefore, MTVI2 is unable to distinguish between these surfaces. In Lucieer *et al.* (2014) a correlation between moss health and water availability was established based on local point measurements. Occurrences of high moss health (health > 90%) were shown to coincide with areas of high water flow accumulation. Geostatistical analysis of the moss health map produced in this study has potential to quantify the statistical significance of this relationship spatially at the scale of the whole study area, but such an analysis is beyond the scope of this paper.

The map of moss surface temperature shows subtle variations across the moss beds. These variations do not seem to be related to moss health, but rather reflect the local micro-topography, shadowing effects, and local moss moisture (water availability) variability. The phenomenon can be clearly seen in the areas of cooler moss occurring south of the large boulders (Figure 4.6c). These areas are shadowed from the sun, which at the time of image collection had an azimuth of 350 degrees and an elevation of 35 degrees. Thus the areas to the south of the boulders are cooler due to the microclimatic differences between the sunlit and shaded sides of the boulders. It is unlikely that the apparent zones of lower moss temperatures are caused by inaccurate spatial co-registration of multispectral and thermal mosaics, as the marked thermal shadow of a large boulder in the centre of Figure 4.6c is too large to be attributed wholly to co-registration errors.

The creation of the visible of thermal mosaics was straightforward with the use of the Photoscan software, however, significant work was required to mosaic the multispectral imagery as it was not compatible with Photoscan. The SIFT algorithm provided the innovation required, allowing the multispectral imagery to be matched to the already georeferenced visible imagery. Matching of ultra-high resolution UAV multispectral imagery with visible imagery using the SIFT algorithm provides a new method to co-register UAV imagery. It should be noted that the methodology needs to

be tested with more topologically variable terrain to validate its performance with datasets collected over steep terrain.

Although the co-registration techniques described in this study have proven to be robust and accurate, an elimination of GCPs and implementation of a direct georeferencing system such as described in Turner *et al.* (2014b) would certainly be a significant future improvement. There are also some limitations to the mini-MCA camera, in particular the rolling shutter and the sensor noise, which need further attention.

4.5 Conclusions

In this study, we have developed a semi-automated workflow for accurate spatial co-registration of image datasets acquired from a Micro Unmanned Aerial Vehicle (MUAV) platform equipped with three different sensors: visible, multispectral, and thermal. We demonstrated that the methodology can achieve a mean co-registration accuracy of 1.78 pixels. A significant achievement of this study was a method to georectify and mosaic a large number of multispectral images acquired by the TetraCam mini-MCA, which could not be previously achieved with available image processing software. The study is also the first to present a detailed analysis of co-registration accuracy of three UAV image datasets acquired at an ultra-high spatial resolution. The benefit of accurate co-registration of UAV sensors was demonstrated through a case study assessing moss plant health and estimating moss surface temperature at a permanent study site in Eastern Antarctica. Both thematic maps, created from the accurately co-registered image mosaics, provide important spatial insights into the dynamic environment and growing conditions of the Antarctic mosses. In this study, we have shown that UAVs carrying multiple sensors can be used to accurately map vegetation canopies. Although future applications will likely deploy all such sensors simultaneously in order to eliminate changes caused by flight time delays, a similar co-registration methodology will still be required.

4.6 Thesis Context

This chapter addressed the third and fourth objectives that were to accurately co-register multi-sensor data collected with an MUAV and to show that the data from these specialised sensors could be related to real-world biophysical parameters. The high accuracy of co-registration that was shown to be achievable is essential if multi-sensor data is to be used to monitor vegetation health.

Chapter 5

Time series analysis of landslide dynamics using an Unmanned Aerial Vehicle (UAV)

Chapter 5 describes the change detection methodology that was used to monitor a highly dynamic landslide over a period of four years and has been published in Remote Sensing 5th February 2015.

Turner, D., A. Lucieer and S. M. de Jong (2015). "Time Series Analysis of Landslide Dynamics Using an Unmanned Aerial Vehicle (UAV)." Remote Sensing **7**(2): 1736-1757.

Abstract

In this study, we used an Unmanned Aerial Vehicle (UAV) to collect a time series of high-resolution images over four years at seven epochs to assess landslide dynamics. Structure from Motion (SfM) was applied to create Digital Surface Models (DSMs) of the landslide surface with an accuracy of 4–5 cm in the horizontal and 3–4 cm in the vertical direction. The accuracy of the co-registration of subsequent DSMs was checked and corrected based on comparing non-active areas of the landslide, which minimized alignment errors to a mean of 0.07 m. Variables such as landslide area and the leading edge slope were measured and temporal patterns were discovered. Volumetric changes of particular areas of the landslide were measured over the time series. Surface movement of the landslide was tracked and quantified with the COSI-Corr image correlation algorithm but without ground validation. Historical aerial photographs were used to create a baseline DSM, and the total displacement of the landslide was found to be approximately 6630 m^3. This study has demonstrated a robust and repeatable algorithm that allows a landslide's dynamics to be mapped and monitored with a UAV over a relatively long time series.

5.1 Introduction

Landslides are a worldwide phenomenon that can have dramatic economic impact and sometimes tragically result in fatalities (Schuster, 1996). There are multiple factors that can make an area prone to landslide formation. Human factors such as drainage and land clearing (removal of vegetation) are some that can be controlled, and may expedite but not necessarily directly cause a landslide. Other environmental factors such as topography and the shear strength of the slope material are more difficult to control. Landslides are typically triggered by heavy rainfall events or sometimes by earthquakes (Pesci *et al.*, 2011; Nadim *et al.*, 2006). The collection of data about existing landslides in a given area is important for predicting future landslides in that region (Bell *et al.*, 2012).

Landslide monitoring requires continued assessment of the extent, rate of displacement, surface topography, and detection of fissure structures that could be related to fracture processes (Niethammer *et al.*, 2010). Measurements of vertical and horizontal displacements improve the understanding of landslide mechanisms (Akca, 2013; Dewitte *et al.*, 2008). Three dimensional (3D) measurements of landslides, such as the creation of Digital Surface Models (DSMs), allow volume displacements to be calculated. These displacements are related to the distance travelled by the landslide, which can improve our understanding of the mechanisms responsible for landslide dynamics and are useful for predicting future movements (Martha *et al.*, 2010). Technologies such as Differential GPS (DGPS), robotic total stations, airborne Light Detection and Ranging (LiDAR), and Terrestrial Laser Scanners (TLS) have revolutionised the periodic collection of DSM data since the early 2000s (Westoby *et al.*, 2012). However, ground surveys with DGPS are time-consuming and have sparse spatial coverage, which results in the omission of fine-scale terrain structure in the resulting DSM (Martha *et al.*, 2010). TLS can suffer from line-of-sight issues, and airborne LiDAR is often cost-prohibitive for individual landslide studies (Westoby *et al.*, 2012). However, none of these methods are suitable for real-time or near-real-time landslide monitoring.

There are many studies that have assessed the ability of various remote sensing techniques and data sources to monitor landslides. Large-scale landslides, such as

those found in the Indian Himalayas, were monitored with satellite data from Cartosat (spatial resolution 2.5 m / pixel) by Martha *et al.* (2010). Several techniques, such as vegetation filtering and the use of GCPs were applied to improve the accuracy of the data, and analysis of multi-temporal imagery allowed Martha *et al.* (2010) to measure the movement of 550,000 m^3 of material from the upper landslide areas. An example of using LiDAR is provided by Bell *et al.* (2012), who mapped hundreds of landslides in Austria and Germany to study their persistence. A TLS was used by Pesci *et al.* (2011) to map the crater of Mt. Vesuvius in Italy in 2005 and 2009. To obtain accurate results, careful analysis of the errors in the TLS data and point cloud alignment techniques were required (Pesci *et al.*, 2011).

Akca (2013) used four fixed cameras to monitor a slope on which an artificially generated landslide was triggered. Photogrammetric techniques were then used to monitor the movement of the landslide, aided by a network of pre-measured Ground Control Points (GCPs); it was found that 103 m^3 of material moved down the slope in the initial landslide event (Akca, 2013).

A new method for monitoring landslides is to utilise Unmanned Aerial Vehicles (UAVs), also known as Unmanned Aircraft Systems (UAS), to collect ultra-high resolution imagery. The use of UAVs for research purposes has become more commonplace in recent times due to technological developments such as autopilot systems, quality digital cameras, miniature GPS, and advances in lightweight carbon fibre airframes (Nebiker *et al.*, 2008). Several recent studies have also demonstrated the power of Structure from Motion (SfM) algorithms for landslide mapping and monitoring (Lucieer *et al.*, 2013; Niethammer *et al.*, 2009; Niethammer *et al.*, 2010; Niethammer *et al.*, 2011).

Immerzeel *et al.* (2014) demonstrated that UAVs and SfM also provide a powerful tool for monitoring glacier movement and change, which in many respects are similar to landslides from a measurement and monitoring perspective. SfM is a relatively new image processing technique based on computer vision algorithms that were first developed in the 1990s. It allows the reconstruction of a photographed surface without the need for GCPs or complex pre-calibration of the camera (Westoby *et al.*, 2012). This is possible because the position and the orientation of

the camera are solved in an arbitrary space simultaneously with a highly redundant, iterative bundle adjustment that is based on thousands of extracted image features (Westoby *et al.*, 2012). The resulting point cloud created by intersecting the matched features can then be transformed into a real-world coordinate system with a small number of GCPs. The mapping of three-dimensional terrain with SfM techniques has been demonstrated by authors such as Harwin and Lucieer (2012), James and Robson (2012), Ragg and Fey (2013), Turner and Lucieer (2013), Lucieer *et al.* (2013), Lucieer *et al.* (2014), and Westoby *et al.* (2012).

Some studies, such as Chou *et al*. (2010) and Bendea *et al*. (2008), have taken advantage of the ability of UAVs to access unsafe landslide areas for the purposes of disaster management. Chou *et al*. (2010) produced a 5 m resolution DSM from imagery, but this required GCPs, terrestrial photography, and camera calibration. Bendea *et al*. (2008) collected imagery with a fixed-wing UAV and processed the data with specialised software (Leica Photogrammetry Suite) to produce georeferenced data to support humanitarian aid after natural disasters such as landslides. In both studies, the most significant limitation was that the maps they produced suffered from low accuracy due to the IMU and GPS data used.

In a geomorphological context, Niethammer *et al*. (2010) used a Quadrocopter UAV platform, which is very similar in ability to the UAV platform used in this study (an Oktokopter), to create a map of a the Super-Sauze landslide (France) based on SfM techniques. Later Niethammer *et al.* (2011) collected a second dataset of the same landslide. This allowed surface features to be tracked such that movement vectors could be calculated and comparison of DSMs allowed vertical displacements to be described. Niethammer *et al.* (2011) suggested that UAV-based measurements of changes in landslide structure can provide an excellent data source for landslide modellers. Walter *et al*. (2009) used a different approach, combining seismic monitoring with UAV remote sensing and concluded that each type of sensor or technique mostly compensated for the other's deficiencies. This technique was able to generate an orthomosaic of the landslide area, but suffered the limitation of requiring 199 GCPs.

Current literature and this study show that landslide monitoring with a UAV is a viable method. Previously, we demonstrated that highly accurate models of landslides can be created by the use of SfM techniques (Lucieer *et al*., 2013). Other authors such as Niethammer *et al.* (2011) have also proven the utility of UAVs combined with SfM for monitoring landslides. In this study, we build on our previous research by increasing the temporal coverage of our study and thus demonstrate that the methodology is repeatable and robust enough to be applied to a substantial time series of UAV datasets. The aim of this study is to accurately co-register multi-temporal UAV datasets, and to determine landslide surface dynamics and calculate volumetric differences from the multi-temporal DSMs. In addition, we examine and measure details such as change in slope and area of the landslide in the time series. Finally, this study aims to apply the image correlation techniques for surface motion detection that we first described in Lucieer *et al.*, (2013) to a multi-temporal dataset of UAV imagery.

5.2 Methods

5.2.1 Platform

Multi-rotor UAVs are becoming more commonplace and are frequently used for commercial and recreational aerial photography. For this study we used an Oktokopter (eight rotors) multi-rotor micro-UAV (see Figure 5.1) with a DroidWorx carbon fibre airframe, a Mikrokopter autopilot (www.mikrokopter.com), and a Photoship One camera gimbal. The Oktokopter has a payload capacity of around 2 kg, a flight duration of 5 – 10 mins (with a typical payload), and a stabilised camera mount to maintain nadir photos during the flight. Mikrokopter flight electronic systems are used to automatically maintain level flight, control the altitude, log system data at 1 Hz (including airframe position as measured with the on-board navigation grade GPS), and autonomously fly the UAV through a series of predefined, three-dimensional GPS waypoints.

Flights were pre-planned using a Google earth image to lay out a grid of waypoints spaced such that a high overlap (60 – 80%) was maintained. Using previous ground survey data, a height profile was used to set the altitude of the waypoints such that a constant altitude was maintained above the landslide surface.

Figure 5.1 – Oktokopter in flight, fitted with Canon 550D camera

5.2.2 Sensor

To collect visible imagery, we used a Canon 550D Digital Single Lens Reflex (DSLR) camera (see Figure 5.1) (18 Megapixel, 5184 x 3456 pixels, with Canon EF-S 18-55 mm F/3.5-5.6 IS lens). Image capture rate was controlled by the UAV's flight control board, which can be programmed to emit a trigger pulse at a desired frequency. The flight control board was connected to a custom-made cable that triggers the remote shutter release of the camera. The camera was operated in shutter priority mode (a fast shutter speed is required to minimise motion blur), in which the desired shutter speed (typically 1/1250 - 1/1600 sec) was set before flight and exposure was controlled by the camera automatically by varying its aperture. Images were captured in RAW format and stored on the memory card in the camera for subsequent download post flight.

5.2.3 Field Site

In 1996 a landslide formed on the western slopes of the Huon valley in southern Tasmania, 35 km southwest of the capital city of Hobart (see Figure 5.2). The landslide formed on a steep slope in a cleared agricultural field next to the Home Hill

vineyard and is approximately 125 m long and 60 m wide at an average elevation of around 80 m above sea level. McIntosh *et al.* (2009) described the landslide as having developed in strongly weathered, layered fine colluviums, which are the remains of underlying Permian mudstone and siltstone that are estimated to be 4 - 5 m deep. The upper areas of the landslide are described as a rotational earth slide, which develops into an earth flow in the lower areas (McIntosh *et al.*, 2009). We have completed seven separate aerial surveys of the site, details of which can be found in Table 5.1.

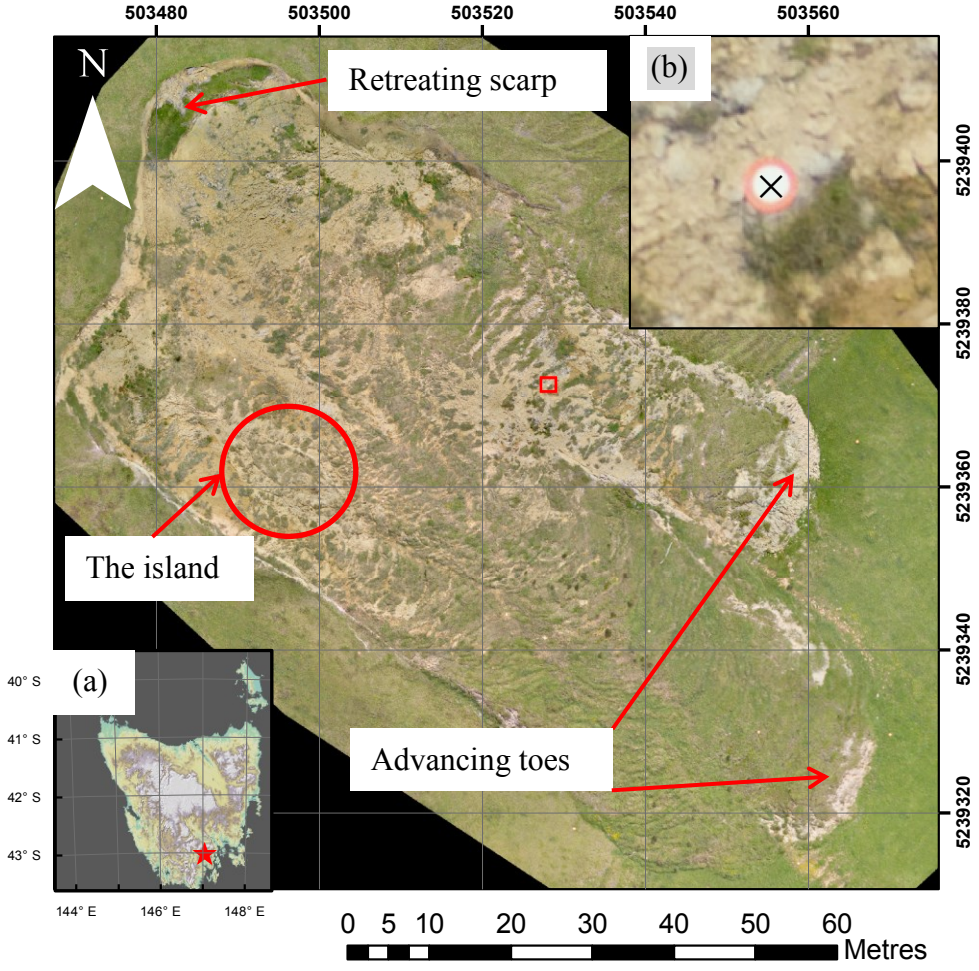

Figure 5.2 – December 2011 ortho-mosaic of Home Hill landslide area highlighting the main features. (a) location map, (b) example of GCP with actual location marked with a black cross giving a typical example of absolute spatial errors (coordinate system: GDA94 UTM55S).

Table 5.1 - Details of aerial surveys of Home Hill landslide

Survey name	Date	Interval (days)	Weather conditions
2010A	20th July 2010	-	Sunny, light winds
2011A	19th July 2011	364	Overcast, light rain and wind
2011B	10th Nov 2011	114	Sunny, moderate winds
2012A	27th July 2012	260	Sunny, light winds
2013A	5th April 2013	252	Sunny, moderate winds
2013B	29th July 2013	115	Sunny, moderate winds
2014A	25th July 2014	361	Sunny, no wind

5.2.4 Three-dimensional model generation

Images collected during each aerial campaign were processed with commercial software, Photoscan Professional (Agisoft, 2012), that uses SfM techniques to reconstruct the scene based on a large number of overlapping photos. The flight path was pre-programmed into the UAVs autopilot to fly a grid pattern over the landslide at approximately 40 m above ground level. As the landslide varies in height by approximately 40 m from top to bottom, the UAV had to descend as it moved down the landslide to maintain a constant height above the landslide surface and thus maintain a constant spatial resolution.

Prior to flight, the camera's internal clock was synchronised with GPS time, which allows the images to be geo-tagged with approximate coordinates from the on-board navigation-grade GPS. Images were collected at a rate of 0.75 Hz which oversamples the study area and provides a high level of redundancy in the dataset. It also allows images with excessive blur or tilt to be excluded. Blurry images were detected and removed via a blur metric as developed by Crete *et al.* (2007), and a further description of its implementation can be found in Turner *et al.* (2014b). Using the positional information for each image, it was also possible to remove the images captured during the UAVs ascent and descent. Furthermore, the positional information was used to find images taken from spatially similar positions, i.e. within close proximity. Images with close to 100% overlap do not provide a significant amount of extra data and thus were also removed.

Detailed descriptions of the Photoscan workflow can be found in Turner *et al.* (2014b), Lucieer *et al.* (2013), and Lucieer *et al.* (2014). However, in summary, Photoscan initially detects tens of thousands of features in each image, which are then matched between the images. Using the matched features it is then possible to use an iterative bundle adjustment to estimate the positions of the matched features, positions, orientations, and lens distortion parameters of the cameras. This information is used for dense multi-view reconstruction of the scene geometry from the aligned images.

These processing steps are carried out in a real-world coordinate system based on the camera positions as supplied in the EXIF header, i.e. the geo-tagged positions as recorded by the UAVs on-board data logger. These positions are only recorded with a navigation-grade GPS receiver and hence are quite inaccurate (5 – 10 m absolute geometric accuracy). To improve the accuracy we manually identify GCPs within the imagery. The GCPs consist of metal discs spray-painted with fluorescent orange paint, scattered around the landslide area and then measured with a dual frequency RTK DGPS, providing GCP coordinates with an absolute accuracy of 2 – 4 cm. Based on these GCPs, Photoscan optimises the bundle adjustment, which is followed by a dense geometry reconstruction. The final step is to export a DSM and orthophoto based on the dense 3D geometry (see Lucieer *et al.* (2013) for a detailed description of the Photoscan workflow).

5.2.5 Alignment of Digital Surface Models

To prepare the DSMs for change detection, it is necessary to check the co-registration of each DSM pair. As each DSM has been georeferenced by separate workflows there is the potential for some minor mis-alignments, the most important of which are any differences in the Z-axis (or height). There is a possibility that there are also rotational or scale differences between a pair of DSMs. To check for such errors, the dense point clouds (from which the DSMs are created) for each model were exported from Photoscan and then imported into the Cloud Compare software package (Girardeau-Montaut, 2012).

Using Cloud Compare, each pair of dense point clouds were initially masked for two reasons; firstly to ensure that both clouds covered the same extent, i.e. they were

fully overlapping; and secondly the active landslide area was removed such that only the points in the surrounding non active areas were considered. An Iterative Closest Point (ICP) algorithm was then run with Cloud Compare on each pair of point clouds, and transformation matrices were estimated. These matrices include rotational parameters, translation parameters, and a scale parameter. For all the point cloud pairs, there was no rotational correction required and the scale factor was 1.0, implying that there were no rotational or scale differences between the point cloud pairs and thus the DSMs. Unfortunately, the translation parameters were inconsistent, as the ICP algorithm would in some cases suggest shifts of 20 - 30 cm in one or more of the three axis. This is theoretically due to the ICP converging to a local minimum in which a large translation minimised the error. Hence, it was necessary to develop another method to determine if there was any remaining constant translational bias between the datasets.

Immerzeel *et al.* (2014), Lucieer *et al.* (2013), and Martha *et al.* (2010) employed a technique to validate the co-registration of multi-temporal DEMs by analysing areas of the DEMs that were not subject to change. Similarly, in this study, we selected four separate areas from outside the active landslide zone, totalling 4,578,868 pixels (approximately 1830 m^2), to further validate the alignment of the DSM pairs. These areas were then compared for each pair and the Root Mean Squared Error (RMSE) and volume difference were calculated (see Table 5.2). As these areas should not be changing, these values should theoretically be close to zero and have a preferably narrow Gaussian distribution of uncertainty/noise inherent to the image. To identify whether there was a constant bias between the DSMs, an offset was iteratively applied, and the corresponding RMSE and volume difference recorded until the optimal offset was found (see Table 5.2). Factors such as differing vegetation height, i.e. the grass may have been longer in one dataset than another, along with errors in the absolute positioning of the model, can contribute to this constant bias. Measurement of volume change does not require an accurate absolute location; an accurate co-registration of the pair of DSMs is of greater importance (Martha *et al.*, 2010). For our calculations, we considered the first dataset of each pair to be the reference landslide and then applied the offset to the second dataset to bring it in line with the first before volume change measurements were made.

Table 5.2 – Evaluation of relative elevation accuracy for each pair of DSMs before and after offsets were applied, and differences between the DSMs were measured over 4,578,868 pixels (1830 m^2) outside the active landslide area.

DSM Pair	Prior to offset application		Offset applied (m)	After offset application	
	Volume difference (m^3)	RMSE (m)		**Volume difference (m^3)**	**RMSE (m)**
2010A – 2011A	153	0.109	0.10	**114**	**0.077**
2011A – 2011B	88	0.061	0.00	**88**	**0.061**
2011B – 2012A	98	0.074	0.00	**98**	**0.074**
2012A – 2013A	134	0.108	0.09	**115**	**0.085**
2013A – 2013B	148	0.101	0.13	**102**	**0.087**
2013B – 2014A	76	0.059	0.00	**76**	**0.059**

5.2.6 Measurement of landslide area and volume change

To measure the overall mass displacement of the landslide, two co-registered DSMs were subtracted from one another. Before these measurements were made, however, an offset was applied to correct for the mismatch in height (Section 5.5). Once the DSM difference is calculated, areas of particular interest, e.g. advances of the landslide toes or retreat of the scarp, were segmented and the volume for each area was calculated. The height difference per pixel was multiplied by the area of a pixel (0.0004 m^2 for the 0.02 m resolution DSMs used in this study) and summed, thus giving a total volume in cubic metres.

The total area of the landslide was measured with the use of GIS software in which the active landslide area was manually digitised by visually identifying the landslide edge within the orthophoto that was generated by the Photoscan software (see Section 5.4). The area was then calculated by multiplying the number of pixels in the polygon by the area of a pixel, which was 0.01 m^2 for the orthophotos generated in this study.

5.2.7 Tracking of landslide surface movement

Lucieer *et al.* (2013) demonstrated that image correlation techniques can be used to track surface features between two DSMs of the landslide. In Lucieer *et al.* (2013) we used an image correlation method developed by Leprince *et al.* (2007) and Leprince (2008). The correlation method is implemented in the ENVI image

processing environment (ITTVIS, 2011) and is referred to as COSI-Corr: Co-registration of Optically Sensed Imaged and Correlation (Ayoub *et al.*, 2009; CalTech, 2011). In Lucieer *et al.* (2013) we experimented with various forms of input images and parameters for COSI-Corr and found that a hillshaded DSM was best for tracking surface features. COSI-Corr performed better on the hillshaded DSM than the colour orthophotos due to large changes in illumination and vegetation colouring and structure between survey events.

This study builds onto our previous work in Lucieer *et al.* (2013) by processing and analysing a time series of seven UAV acquisitions of the Home Hill landslide. ENVI was used to initially produce hillshaded images from the DSMs for each of the seven dates with an input sun elevation of 45° and azimuth of 315°. These settings emulate the lighting conditions that are typical for a summer afternoon in the area and highlight the main terrain features as the azimuth is aligned with the main orientation of the landslide. COSI-Corr has a number of parameters to be selected. In this study, we used the same settings in Lucieer *et al.* (2013), i.e., the statistical correlator with a window size of 64 pixels, a step size of 8 pixels and a search radius of 50 pixels (5 m), as these proved superior in motion detection.

5.3 Results

5.3.1 Accuracy of DSMs and orthophotos

To assess the accuracy of the DSMs and the orthophotos created by Photoscan we typically used around 30% of the GCPs as check points (see Table 5.3). This means that approximately 70% of the GCPs were used for the bundle adjustment and the transformation to an accurate real-world coordinate system. The remaining GCPs were used as check points to assess the accuracy of the model, which was done by measuring the distance between GCPs in the orthophoto (for the x,y position) and the DSM (for the z position), and its correct location (as measured by RTK DGPS). For all the check points, an RMSE was calculated, and a summary of the results is presented in Table 5.3. Due to limited resources, we only had 23 GCPs for the 2011B dataset and thus all of these were required to transform the model. It can be seen that typical RMSE values are around 4 – 5 cm in the horizontal direction (XY) and 3 - 4 cm in the vertical direction (Z). The largest, RMSE 0.076 m and 0.09 m in XY

and Z directions respectively, occurred in the 2013B dataset, which is possibly due to poorly measured GCPs and/or excessive shadowing on the landslide surface.

Table 5.3 - Summary of spatial errors for Home Hill landslide DSMs and orthophotos

Name	Date	Number Photos used in model	GCPs	Checkpoints	XY RMSE (m)	Z RMSE (m)
2010A	20th July 2010	62	56	19	0.046	0.031
2011A	19th July 2011	116	41	20	0.045	0.042
2011B	10th Nov 2011	194	23	23*	0.021	0.025
2012A	27th July 2012	170	66	17	0.047	0.039
2013A	5th April 2013	179	29	22	0.058	0.078
2013B	29th July 2013	241	23	21	0.076	0.090
2014A	25th July 2014	415	16	10	0.031	0.031

* GCPs also used as check points due to limited resources

5.3.2 Area and slope analysis

The main area of change is the advancement of the two toes at the bottom and the retreat of the scarp at the top of the landslide (see Figure 5.2). The changes in landslide area are presented in Table 5.4. There were five events of the little toe advancing (a total of 554 m^2 during the whole monitoring period) and three scarp retreat events. There was no noticeable change in area between the 2013A and 2013B datasets, possibly because much of the movement occurs in surges rather than a gradual creep, and/or because movement during this short time period was too small to be measured.

The slope of the leading edge of the toes was measured by calculating the slope from the DSM and taking a mean of all the pixels in the leading edge area (see Table 5.4). The steepness of the leading edge gradually builds up, particularly of the large toe, as material flows down from above until eventually the leading edge collapses and the toe surges forward. This surge effect can be seen graphically in Figure 5.3. There was little or no forward movement of the large toe between the 2010A and 2012A surveys, but internal shear stress was building up; then, sometime before the 2013A measurement, the leading edge gave way and the large toe advanced around 1 - 2 m (contributing to the 126 m^2 of area increase at this time) and the slope reduced in steepness. It can be seen in 2014 that the slope is beginning to steepen again, and it is likely the cycle will continue as material continues to flow down the slope. The trend

is not quite so obvious for the small toe, most likely because this area underwent some large changes during the monitoring period (it advanced around 12 m between 2010 and 2011) and has thus not settled into the same pattern as the large toe, i.e. the deformation pattern is more chaotic. In 2014 the slope is becoming steep again and apparently internal pressure and stress are building up. Based on past dynamics, it is likely that the toe will surge forward again soon.

The other significant changes in landslide area came from the three retreats of the scarp, of which the first occurred between July 2011 and November 2011 when there was a large collapse (162 m^2) of the northern part of the scarp. Much of this material seems to have flowed down the slope and contributed to the major advance of the small toe. Between July 2012 and July 2013, a further 95 m^2 of the northern part of the scarp collapsed, followed by a further collapse of 47 m^2 in 2014, making this a highly dynamic area of the landslide. There were no significant collapses in the southern area of the scarp during the monitoring period, despite the fact that it is also a near vertical face of similar height.

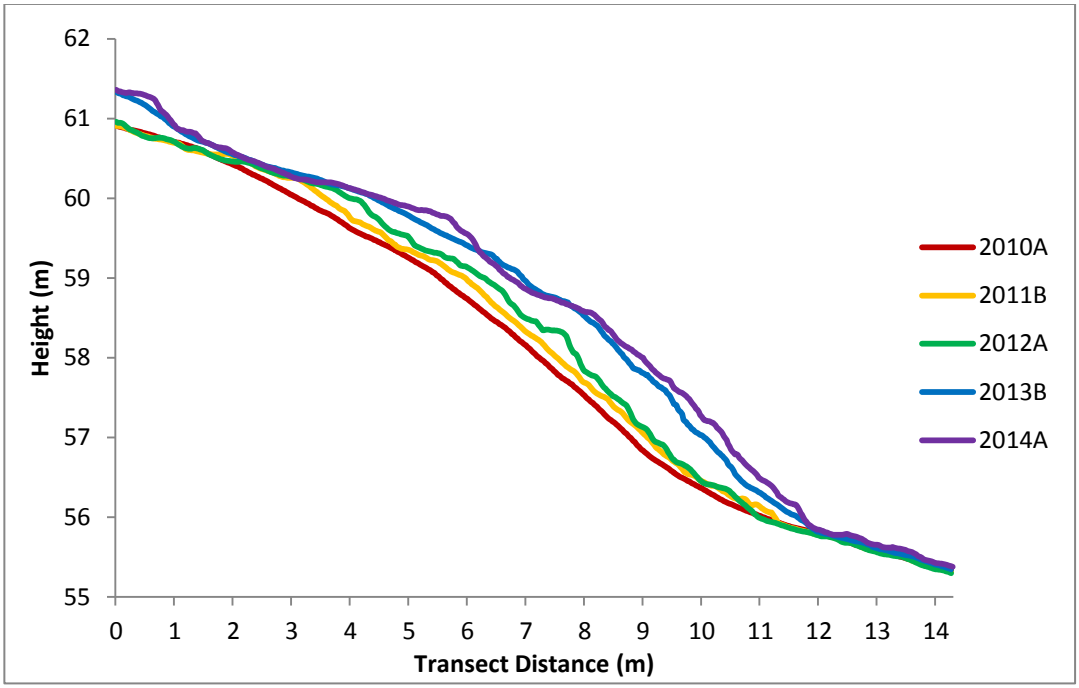

Figure 5.3 - Transects through leading edge of the large toe

Table 5.4 - Changes in area and leading edge slope of Home Hill landslide

Name	Total area (m^2)	Slope of large toe (deg)	Slope of small toe (deg)	Area of toe advance (m^2)	Area of scarp retreat (m^2)
2010A	4887	31.05	36.26	-	-
2011A	5168	33.72	34.92	281	-
2011B	5435	34.37	34.06	105	162
2012A	5455	39.98	36.22	20	-
2013A	5675	34.17	34.78	126	95
2013B	5675	33.17	34.54	-	-
2014A	5744	33.87	37.63	22	47

5.3.3 DSM volumetric changes

An example of the DSM change is presented in Figure 5.4, highlighting typical changes on the Home Hill landslide. There was a loss of material where the scarp has collapsed (see Figure 5.4 near (a)) and an accumulation of material at the leading edges of the toes (see Figure 5.4 near (b)). The spatial pattern of mass losses and gains on the landslides matches intuitive expectations of movements on such a landslide. The pattern is typical and can be found for most of the DSM comparisons where the scarp has collapsed and/or the toes have advanced. Subsequent comparisons were then made for the other DSMs. From these maps, areas of interest (e.g. the collapsed scarp, see Figure 5.4a for an example) were selected and volumetric change was calculated as described in Section 5.2.6. A summary of the volumetric changes for the small toe of the landslide is presented in Table 5.5, which also presents the bulking factor, the ratio of the volume gain to volume loss. For the first two comparisons the bulking factors are typical of what might be found on other landslides with similar characteristics (Martha *et al.*, 2010). However, in the remaining comparisons, the values are higher than one would expect.

Table 5.5 - Volumetric changes in m^3 for the small toe of Home Hill landslide, including estimated errors at one sigma; also reported is the bulking factor, the ratio of accumulated material to lost material.

Name	Toe accumulation and estimated error (m^3)	Loss above toe and estimated error (m^3)	Bulking factor
2010A -> 2011A	572 ± 24	340 ± 14	1.68
2011A -> 2011B	249 ± 21	124 ± 17	2.00
2011B -> 2012A	88 ± 19	24 ± 10	3.66
2012A -> 2013A	175 ± 21	41 ± 9	4.27
2013A -> 2013B	no change	no change	-
2013B -> 2014A	85 ± 17	22 ± 8	3.86

There are likely to be some inaccuracies in the volumetric measurements due to minor misalignments of the DSMs and environmental differences between datasets, such as the length of the grass. The alignment processes described in Section 5.2.5 minimised these alignment errors, but we wanted to quantify the error of the volumetric measurements. The average RMSE of the difference between the non-active areas of the landslide was 0.07 m (see Table 5.2), and the mean standard deviation of these differences was also 0.07 m. The errors expressed in Table 5.5 are thus expressed as +/- 0.07 m (one sigma).

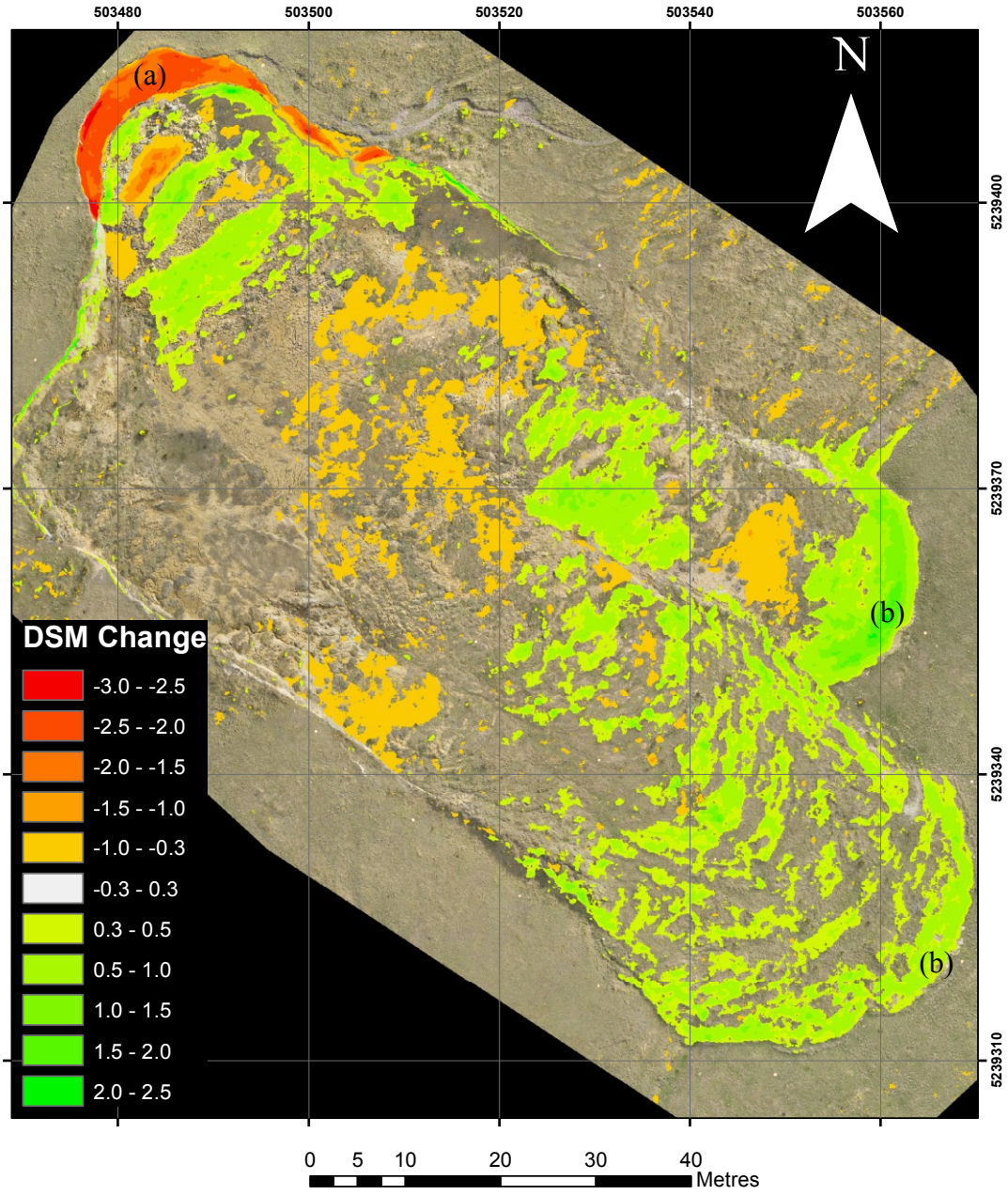

Figure 5.4 – 2012A to 2013A DSM change; (a) area of scarp collapse, (b) areas of toe advance (coordinate system: GDA94 UTM55S).

5.3.4 Historical DSM

To model the terrain before the landslide occurred, we obtained a pair of overlapping historical aerial photographs of the Home Hill area from the archives at the Department of Primary Industries, Parks, Water and Environment (www.dpipwe.tas.gov.au). The images were collected in 1984 and had a scale of 1:15,000. The images were scanned at 2000 dots per inch, which gave a ground

resolution of approximately 20 cm/pixel. The digital scans were imported into Photoscan and a 3D model was constructed (see Figure 5.5). Ground features that were identifiable in the 1984 images and in the latest Google Earth imagery (e.g. edges of roads, corners of roofs, and corners of fence lines) were used as GCPs to enable georeferencing of the model.

Figure 5.5 – 3D model of the Home Hill landslide as constructed from 1984 aerial photography. The landslide area is circled in red.

The georeferencing accuracy of the Google Earth imagery is insufficient for the 1984 model to be accurately co-registered with the recent UAV datasets. In a similar manner to the method used to align the DSMs (Section 5.2.5), we aligned the 1984 model with a recent dataset from July 2013. The alignment was carried out on the point cloud data rather that the DSMs, because both horizontal and vertical misalignments had to be corrected. Cloud Compare (Girardeau-Montaut, 2012) was used for the point cloud co-registration using the ICP algorithm (Besl and McKay, 1992), which minimises the distance between two point clouds. This process considered the 2013 dataset the true one and moved the 1984 point cloud as close to the 2013 point cloud as possible. Once a visual validation of the results was completed, the LAStools software suite (Isenburg, 2012) was used to interpolate the 1984 point cloud into a DSM.

The 1984 DSM is based on much lower resolution imagery than the data captured with the UAV and thus the final 1984 DSM only had a resolution of 50 cm/pixel,

requiring the 2013 dataset to be resampled to match this resolution. Using the methods described in Section 5.2.6, volumetric calculations were made. The approximate values for total amount of material moving down the landslide are 6630 m^3 of accumulation in the lower areas of the landslide and 3300 m^3 of material lost from the upper areas, producing a bulking factor of 2.02 which is typical for this type of landslide (Martha *et al.*, 2010).

5.3.5 Surface movement

As described in Section 5.2.6 the COSI-Corr image correlation software was used to compare DSM datasets to track the movement of surface features. In Lucieer *et al.* (2013), COSI-Corr was applied to the 2011A and 2011B datasets to create one map of surface movement. We now have three more data sets (2012A, 2013A, and 2014A) to which COSI-Corr was applied, expanding the dataset to four maps of surface movement (see Figure 5.6A to D).

Figures 5.6A to D illustrate the irregular behaviour of the landslide movements between the different image acquisition dates even if one accounts for the variable numbers of days between image takes (Table 5.1). These observations may confirm the 'surge behaviour' of the landslide. The small toe at the north-east side of the landslide is clearly the most active part. Registered displacement range up to 7m for the 2012A – 2013A data taken with an interval of 252 days as shown in Figure 5.6B. The large toe, situated in the southern part of the landslide is less dynamic and only shows a major displacement in Figure 5.6C for the 2013A to 2013B image period. Displacements range up to 4 m. Displacement registration at the scar is difficult for the COSI-Corr algorithm since the movements are nearly vertical, which makes them difficult to identify in UAV-based horizontal images. Furthermore, scar movements often show rotational movement hampering the identification of surface features required by COSI-Corr to compute the displacements. The scar shows clear signs of surface instability and movements in Figure 5.6B and 5.6C. Detached material at the scar is required to activate or re-activate the movements of the toes.

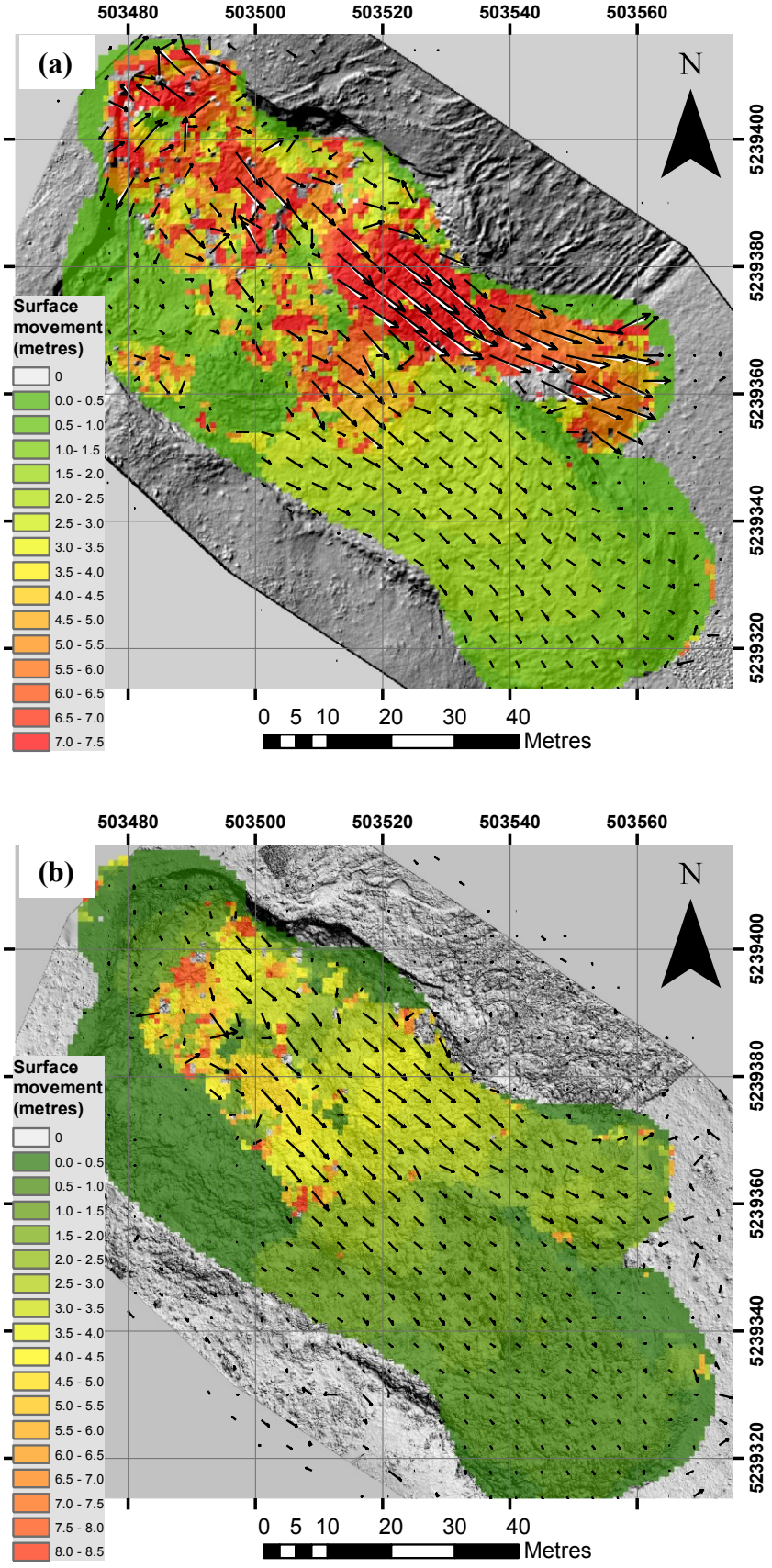

Figure 5.6 ***Cont.***

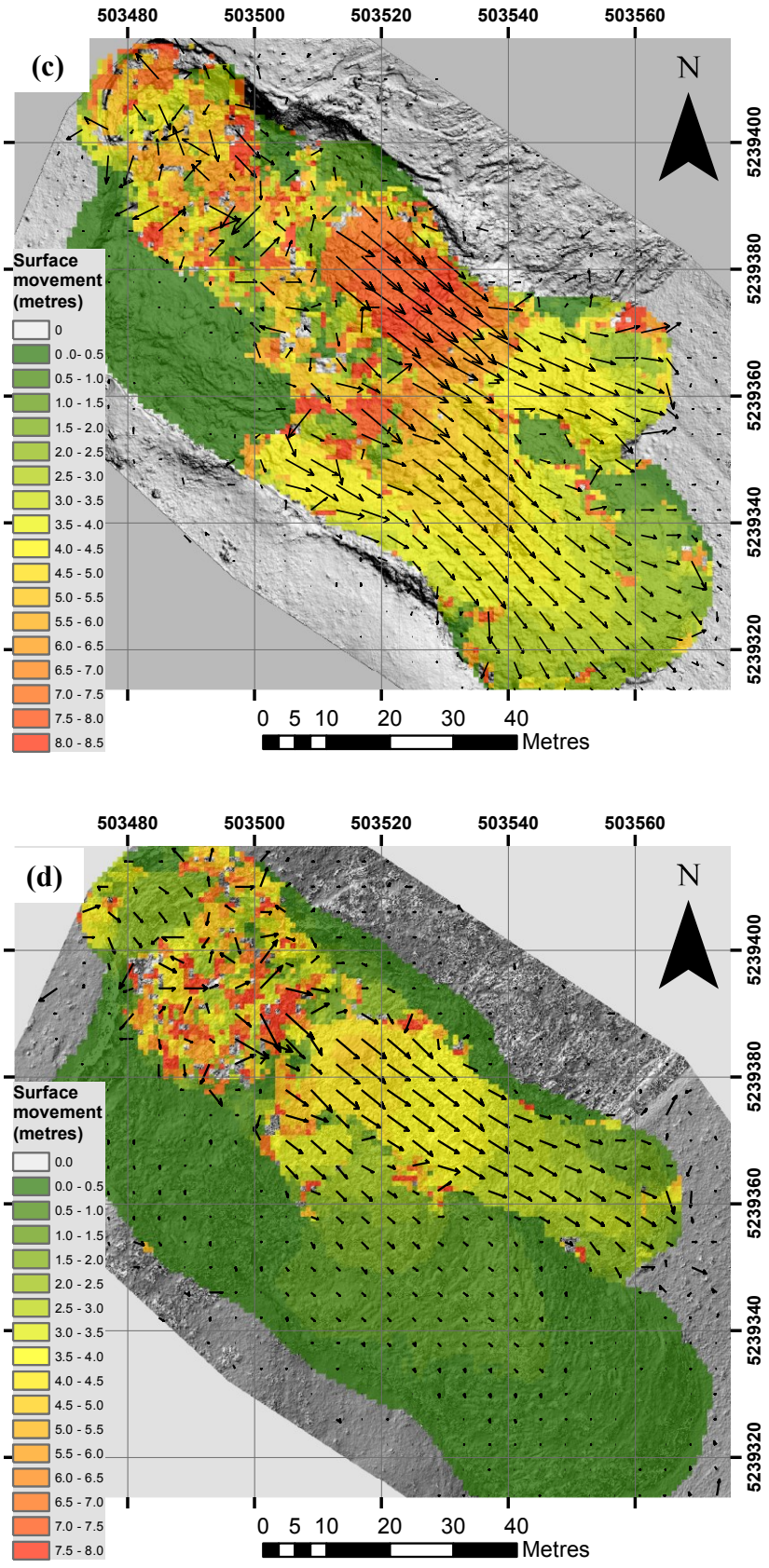

Figure 5.6 – Cosi-Corr surface movement maps; a) 2011B – 2012A, b) 2012A – 2013A, c) 2013A – 2013B, and d) 2013B – 2014A (coordinate system: GDA94 UTM55S).

5.3.6 Comparison of landslide movement with rainfall

The lower areas of the Home Hill landslide are described as an earth flow by McIntosh *et al.* (2009), and we have hypothesised that movement of the landslide is triggered by extreme rainfall events, as precipitation is one of the main landslide triggering factors (Scaioni *et al.*, 2014). We also hypothesise that the rate of the earth flow may be partially related to the amount of rainfall that the landslide receives in the preceding days or weeks. To test this hypothesis, rainfall data from the two nearest rainfall stations, Huonville (3.8 km away to the south) and Grove (4.75 km away to the north) were analysed. The total annual rainfall between each July landslide dataset, i.e. 2010A, 2011A, 2012A, 2013B, and 2014A was calculated and averaged across the two rainfall stations and then translated into a mean daily rainfall for that year. The annual rainfall rate was then compared with mean daily volume of movement for the small toe area (see Figure 5.7).

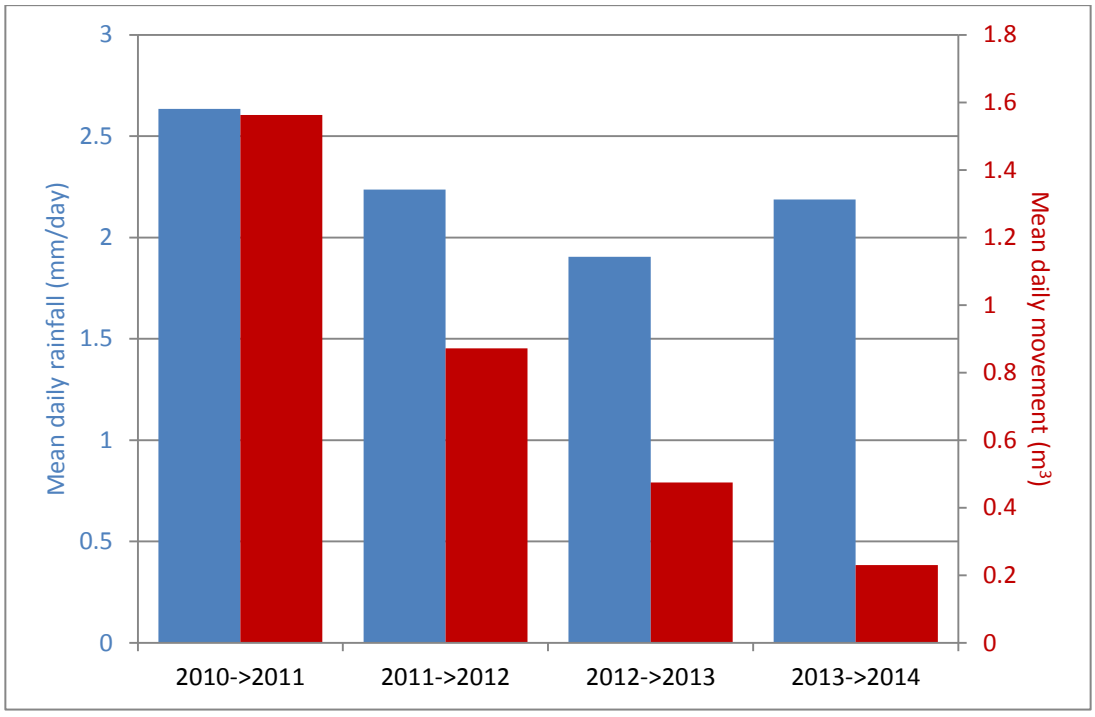

Figure 5.7 – Comparison of annual rate of rainfall and annual rate of accumulation of material for the little toe area of the Home Hill landslide

5.4 Discussion

To allow accurate and detailed comparisons of landslide changes and movement, it is important that the errors in the alignment of all the datasets be minimised. The creation of 3D models from UAV imagery has a limitation in that it does not create a true Digital Elevation Model (DEM) of the surface; instead it created a DSM. This is because the technique is based on a passive optical sensor that cannot penetrate the vegetation and find the true surface height, as a LiDAR system might. However, we have implemented a method to minimise the alignment error between datasets caused by factors such as the variable height of the grass.

Simple measurements, such as change in area and slope of the landslide, can be informative. These data can be used to infer patterns of movement, such as the cycle of leading edge slope change (see Section 5.3.2). Increasing the temporal coverage of the dataset, i.e. increasing the frequency of measurement and continuing to collect regular datasets into the future, could confirm the validity of these cycles.

From the data collected, the actual calculation of volumetric change was a trivial matter; however, it does suffer from a degree of uncertainty. This is caused by multiple factors that contribute to the absolute accuracy of the models, resulting in an error in the Z-axis. However, when areas of volumetric change are large, these inaccuracies will result in volumetric errors that only represent a small percentage of the total volume measured (see Table 5.5). Conversely, when measuring subtle changes, these errors will represent a high percentage of the total volume measured (see Table 5.5), i.e. the absolute error is small but the relative error is large.

Applying the same surface reconstruction methods to historical aerial photography can provide an approximate baseline dataset for the original landform prior to the formation of the landslide. Acquisition of further aerial photographs from the past has the potential to increase the temporal coverage of this landslide monitoring study.

Advanced image correlation techniques provide an automated method for tracking surface movements of the landslide, giving us an insight into the rate at which various areas of the landslide are moving and also which areas remain static. There is one area, denoted as “the island” (see Figure 5.6a), which does not move at all.

Inspection of the surface material in this area revealed a conglomerate of rocks which is likely to be holding this area together while the landslide flows around it (like a nunatak in a glacier). The large toe is clearly steadily flowing down hill (see Figure 5.6) and seems to have settled into a pattern of the leading edge building up until it collapses and surges forward (see Figure 5.3). However, the little toe area is more dynamic (see Figure 5.6), with major forward surges. These surges seem to have reduced the material supporting the northern part of the scarp and thus it has collapsed on two separate occasions, providing more material to flow downhill on the little toe.

When measuring volumetric changes, we also calculated the bulking factor for accumulation areas of the landslide. Bulking factors up to a value of 2.0 are known to be typical for landslides of this type (Martha *et al.*, 2010). However, some very high values (up to 4.3) were found, for example the 2013A comparison (see Table 5.5), and the COSI-Corr movement maps can help explain these high values. The surface changes between 2012A and 2013A (see Figure 5.6c) shows a great deal of movement above the small toe, so it is likely the area of loss was filled from above. This would reduce the measurement of volume loss and result in a high value for the bulking factor.

Analysis of rainfall data and comparison with landslide movement (see Figure 5.7) has shown a strong relationship for the first three annual comparisons. However, the relationship is not evident in the fourth comparison, and this may be due to several factors. The leading edge of the little toe in the 2014 dataset was very steep (see Table 5.4), implying that it is likely to surge forward again soon. The small toe has now extended to a similar part of the slope as the large toe, that is, an area that is not as steep, and it is also starting to fan out in a similar fashion to the large toe; these factors would slow the rate of movement (compared to the previous years) and thus reduce the volume of material moving down-slope.

There is further evidence of rainfall being related to landslide movement when we examine the historical records from 1996, the year in which the landslide occurred. In 1996 the monthly rainfall for January was 194% of the long term mean; in February it was 268%; March, 166%; and in April the rainfall was 338% of the long

term mean. It may very well be that this excessive rainfall triggered the landslide. We know from the 1984 imagery that the area had been cleared of vegetation, meaning that for at least the 12 years prior to 1996 the land was cleared. It is thus unlikely that the land clearing alone was the cause of the landslide. Further detailed ground study is required to better understand the structure of the landslide material and to assess its failure characteristics, which will be the subject of future research.

5.5 Conclusions

A significant achievement of this study was to demonstrate that it is possible to generate accurate Digital Surface Models (DSMs) of a landslide with an Unmanned Aerial Vehicle (UAV) and that this technique is robust and repeatable such that a substantial time series of datasets can be routinely collected. Another achievement was the development of a technique to check and correct for any co-registration errors between subsequent DSMs based on comparing non-active areas of the landslide minimizing the alignment error to ±0.07 m on average. Measurements of variables such as landslide area, leading edge slope, and volumetric changes were made over a time series of seven DSMs spanning four years. The COSI-Corr: Co-registration of Optically Sensed Imaged and Correlation (CalTech, 2011; Ayoub *et al.*, 2009) image correlation algorithm was used to track and quantify surface movement vectors of the landslide. It should be noted that there is no ground validation for the movement vectors generated by COSI-Corr; however, we have demonstrated that COSI-Corr is robust and works over a series of datasets collected with the same methodology.

The main new finding of this study was to prove that a time-series of UAV images can be used to map landslide movements with centimetre accuracy. It also found that there can be a cyclical nature to the slope of the leading edge of the landslide, suggesting that the steepness of the slope can be used to predict the next forward surge of the leading edge. It was also discovered that historical aerial photography could be used to create a DSM as a baseline dataset for comparison to the modern DSMs. This revealed that a total of approximately 6630 m^3 of material had moved downslope since the formation of the landslide. Evidence was also found that there is

a relationship between the amount of rainfall that the landslide receives and the volume of material that flows downslope.

The methodology described in this paper advances knowledge in that it allows a series of measurements to be made of landslide variables. These measurements can assist experts in monitoring and understanding landslide movement dynamics. Whilst there have been other studies that have mapped surface movement of landslides and glaciers with UAV imagery (Immerzeel *et al.*, 2014; Lucieer *et al.*, 2013; Niethammer *et al.*, 2009; Niethammer *et al.*, 2010; Niethammer *et al.*, 2011), this study is unique as it has presented a methodology to accurately co-register DSMs and to perform a deformation analysis of a time series consisting of seven separate datasets. It also builds upon our previously published research into the use of image correlation techniques to track surface movement, demonstrating that the technique is robust and can be applied to a longer time series of images.

The way forward for this research will involve continued monitoring of the landslide to further validate the findings in this study, e.g., the relationship between the leading edge slope and movement of the leading edge, and also the relationship between rainfall and volume displacement of material on the landslide. It would be advantageous to be able to sample the landslide at a higher frequency, which will require improvements in the methodology to minimize the time required in the field. This could be achieved by implementing a direct georeferencing system, as described in Turner *et al.* (2014b), to remove the requirement for Ground Control Points (GCPs).

5.6 Thesis Context

This chapter addressed the fifth objective that was to demonstrate that high spatial and temporal resolution UAV datasets can be used for change detection purposes. The case study demonstrated that it was possible to quantify the magnitude and spatial patterns of a highly dynamic landslide. It was shown that this type of study can provide change detection data that can be used to better understand the structural dynamics of the landslide used for the case study.

Chapter 6 Conclusions

This research set out to advance understanding of the use of Unmanned Aerial Vehicles (UAVs) as tools for environmental remote sensing. Specifically, the aim of the work was to develop that image processing workflows and algorithms to enable micro-UAVs (MUAVs) to be effective tools in the context of environmental remote sensing. A series of impediments to the adoption of MUAVs by the remote sensing scientific community were uncovered which provided the objectives of the thesis. Each chapter of this thesis contributes to one or more of these objectives, and has been published in the peer reviewed literature. Here, each objective is restated, and how well each was achieved is discussed.

6.1 Ortho-mosaic creation

Objective 1 – To assess existing methods to georectify and mosaic UAV imagery, and subsequently develop an algorithm that overcomes limitations in traditional approaches and enhances existing techniques to enable automated and accurate georectification and mosaicking of UAV imagery.

Existing methods based on traditional aerial photography algorithms were found not to be suitable or sufficiently robust to successfully process imagery collected from low altitude platforms such as MUAVs. At the time of addressing this objective (2010 – 2012) there were no commercial-off-the-shelf (COTS) software packages specifically designed for mosaicking and georeferencing large sets of MUAV imagery in a semi-automated fashion.

To address this objective, an approach was successfully developed and implemented that made use of new Computer Vision (CV) and Structure-from-Motion (SfM) algorithms such that images collected by an MUAV could be mosaicked and georeferenced without significant input from the user. It was also discovered that using this technique made it possible to directly georeference the imagery, i.e. without the need for GCPs. However, the geometric accuracy of the ortho-mosaics produced was limited by the accuracy of the GPS receiver on-board the UAV.

Since the achievement of this objective (Turner *et al.*, 2012), software has become commercially available (e.g., Agisoft Photoscan and Pix4D) that can create 3D point clouds and orthomosaics from UAV imagery. These packages use a similar methodology to that

presented in Chapter 2, in that large numbers of points are detected and matched between each of the images, followed by a bundle adjustment to align the images based on these matching points. The methodology in Chapter 2 made use of a Helmert transform to convert the arbitrary coordinate locations derived from the bundle adjustment into real world coordinates. In contrast, commercial software such as Photoscan uses a similar technique, but perhaps more robust. In summary, this objective was initially met by the technique presented in Turner *et al.* (2012), and then subsequent developments in the rapidly changing commercial sector provided software that meets this objective. It should be noted that the technique described in Chapter 2 is based on freely available open source software, whereas the commercial alternatives obviously have a cost associated with them.

6.2 Direct georeferencing of UAV imagery

Objective 2 – To reduce or completely remove the need for GCPs when collecting a UAV image dataset. To develop a hardware and software solution to accurately synchronise camera exposure with GPS position. To assess the accuracy of direct georeferencing in several Structure from Motion (SfM) processing approaches.

Whilst developing the methodology to address the first objective it was found that it was possible to directly georeference UAV imagery datasets based on the location of the camera at the time of image capture. However, the accuracy was limited by two factors: 1) the accuracy of the GPS positions measured on-board the UAV (typically only navigation-grade GPS), and 2) the synchronisation of the camera exposure time with the GPS trajectory (typically based on manually setting camera time before flight).

To address these issues hardware was designed to make use of a single frequency carrier-phase differential GPS to improve the accuracy of the recorded airframe position during flight. Accurate synchronisation with camera exposure time was achieved via a cable that used the pulse emitted on the camera's flash hotshoe to mark the exposure time in the GPS log with a precision of ± 0.001 sec. In Chapter 3 the delay between the actual shutter release and the hotshoe pulse was discussed and hypothesised that even in a worse-case scenario the delay would translate to errors in actual versus flagged position of < 0.05 m, which is within the precision of the GPS trajectory estimates. Since then, the delay has been further analysed by setting an oscilloscope to be triggered at the time of shutter release. The oscilloscope display was photographed with the camera and the position of the trace on the oscilloscope

display was measured to quantify the delay at a given shutter speed. It was found that at the shutter speeds typically used during UAV flight (faster that 1/1000th sec), the delay is extremely short (less than a millisecond,). Hence, in relation to the accuracy of the GPS position recorded (0.1 - 0.2 m) and the slow flight speed of the platform (< 3 m/s), the delay can be considered to be negligible (at this speed 1 millisecond only represents 3 mm of movement).

In assessing the accuracy of the direct georeferencing system, two pre-processing algorithms were developed to select the best images to be used based on image blur and optimal spacing. MUAV RGB imagery was processed with i) the technique developed in Chapter 2, ii) the commercial software Photoscan Professional (http://www.agisoft.com/), and iii) with an online data processing service Pix4D (http://pix4d.com/). Photoscan produced orthomosaics with the best geometric accuracy of around 11 cm which is comparable to the absolute accuracy that is achieved by the single frequency DGPS used to record platform and thus camera position. This shows that the dominant contribution to uncertainty in the final mapping product for the direct georeferencing approach is uncertainty in the recorded camera positions.

6.3 Co-registration of multi sensor data

Objective 3 – To develop a technique to co-register multiple datasets that have been collected during separate UAV flights with multiple sensors. To develop a co-registration workflow that is semi-automated with minimal user-input and without manual co-registration. To assess the spatial accuracy of co-registration between the separate sensors.

The amount of payload that can be carried on an MUAV is a limiting factor, in many cases resulting in the necessity to carry each required sensor on separate flights. It is thus essential the data collected is accurately co-registered once mosaicked and georeferenced. A case study using data collected with visible, multispectral, and thermal infrared sensors was used to demonstrate the accuracy of the algorithms developed.

Data collected with the visible and the thermal infrared sensors can be mosaicked and georeferenced with the Photoscan SfM workflow as demonstrated in Chapter 3. The multispectral imagery could not be processed with Photoscan, most likely due to noise in the

imagery and the use of a rolling shutter which leads to geometric distortions in the imagery that are not parameterised as part of the SfM algorithms. Thus new algorithms were developed to process these data using the Scale Invariant Feature Transform (SIFT). SIFT was used to automatically detect thousands of features within the multispectral imagery that could be matched with SIFT features from the already georeferenced visible mosaic, thus providing GCPs for the multispectral data. Once data from each sensor was processed into an orthomosaic, the co-registration accuracy was assessed and found to have an RMSE of 1.78 pixels. The approach developed achieves both the co-registration and the automation objectives as the use of the Photoscan SfM workflow and the new multispectral image processing algorithms are semi-automated. However, it should be noted, that whilst semi-automated, the multispectral image processing algorithms do require significant user supervision, for example, checking sufficient control points are being detected for each image.

The methodologies presented in Chapter 3 allow an MUAV to become a high resolution, multi-sensor platform, greatly enhancing their utility as an environmental remote sensing tool. The case study demonstrated that an MUAV could be used to create maps of surface temperature and moss health given accurately co-registered datasets.

Objective 4 – To demonstrate that multispectral and thermal imagery can be related to real-world surface properties such as vegetation health and surface temperature.

Data collected with specialised sensors (i.e. other than RGB cameras) has the potential to provide quantitative information about the area being studied. To make use of specialised sensors, an initial step is the conversion of raw data into meaningful measurements through the use of calibration. In the case of the thermal infrared camera, the data was converted from raw digital numbers into temperature values by relating the raw data to ground-based *in situ* measurements. The multispectral data was calibrated by the use of ground calibration panels, which had their spectral signatures measured *in situ*. An empirical line correction was used to convert the raw data into reflectance values. The reflectance values were then used to generate a vegetation index (modified triangular vegetation index 2) which in turn was related to ground measurements of moss health. A strong relationship was found expressed by an R^2 of 0.64 for the non-linear regression. The co-registration of the three sensors enabled these results to be presented as maps of moss health and moss temperature, and thus

demonstrate that multi-sensor data can be used to derive real-world environmental conditions. This case study demonstrated the ability of multi-sensor UAV remote sensing to capture a spatial scale niche that bridges field observations and full-scale airborne or satellite observations by capturing ultra-high resolution imagery (<10 cm pixel size) over a significant study area (1 – 2 ha).

The main limitation of relating the raw data to *in situ* observations of vegetation health and temperature is the quality of the sensors. Small sensors for UAV remote sensing tend to have a high signal to noise ratio, which is caused by their limited size, weight, and cost. As MUAVs become more commonly used for environmental remote sensing, the market will hopefully drive vendors to produce lightweight cameras with higher quality sensors.

6.4 Multi-temporal studies

Objective 5 – To demonstrate that the combination of high spatial and temporal resolution UAV datasets provide sufficiently accurate data such that change detection can be undertaken across the datasets. To measure the accuracy of the changes quantified, and to minimise any errors in the co-registration of the temporal datasets.

Highly overlapping MUAV images can be used to create a high resolution DSM from which it is possible to generate derivatives such as slope and volume changes. The ability to easily revisit a site of interest and collect data at a high temporal resolution is another advantage of an MUAV. Monitoring a highly dynamic landslide was considered as a case study in order to address this objective (Chapter 5). A total of seven MUAV datasets collected over four years were investigated.

The case study clearly demonstrated that the methodology used to survey the landslide is robust and repeatable (the methodology was successfully applied to seven datasets). DSMs were the primary product derived from the UAV RGB photography, allowing measurements of volumetric change to be made. Several other products were extracted from the time series of DSMs such as changes in area and slope, along with the automated tracking of surface features, allowing movement vectors to be calculated.

Co-registration inaccuracies must be considered as a limitation of this methodology. In the case study, these inaccuracies were quantified (mean error estimated to be $\pm$ 0.07 m) and given as error margins for any volume measurements presented. The relationship between the

total volume change measured and the error is directly related to the area over which the changes occurred. The magnitude of the volume error varied from around 10 m^3 to 20 m^3, whilst the total volume change measured varied from 20 m^3 to 570 m^3.

This case study would not have been possible without the high spatial and temporal resolution of the data that can be collected with an MUAV. Other methods such as terrestrial laser scanning would have had difficulty achieving the same coverage as this method and it would have been prohibitively expensive to collect such a time series covering seven epochs.

6.5 Contributions to knowledge

The development of MUAV hardware (data logging, sensor integration and synchronisation) and software components (image processing algorithms and workflows) presented in this thesis demonstrate significant progress in the field of UAV remote sensing. The primary contributions of this thesis to knowledge in this area of research can be summarised by the following points:

- This study demonstrated that a low-cost system (less than AU$10,000) can be used to efficiently collect optical images and that these images can be mosaicked and georeferenced in a robust fashion.
- This study developed a novel direct georeferencing system that achieved an accurate exposure time synchronisation, and produced orthophotos with an accuracy of around 0.11 m.
- This study developed a semi-automated methodology for accurately co-registering data collected from multiple sensors during separate flights.
- This study demonstrated that NIR and TIR sensors can collect data on vegetation health and surface temperature that can be related to real-world conditions quantitative measurements.
- This study collected and analysed a multi-temporal dataset (spanning four years with seven datasets) for monitoring landslide deformation at an unprecedented level of detail and with a high temporal resolution.

6.6 Limitations and future research directions

This thesis has brought to light some of the limitations of remote sensing with a UAV, in particular around the airframe and the sensors. An MUAV can only fly for a relatively short time (5 – 10 min.) and thus can only transit over a comparatively small area. As a result of the limited flight duration, an MUAV can only map small areas; typically up to 10 ha in a day is feasible. Mapping areas larger than this becomes impractical due to: time taken to collect the data; quantity of data required to be collected; difficulties with processing large datasets. MUAVs are really suited only to environmental remote sensing projects that fall into a niche in which ultra-high resolution data is required, but the area to be mapped is not too large. However, with advances in airframe and computing technology these limitations may soon

become irrelevant, flight times are already increasing and computers capable of handling the large quantities of data collected are likely to soon be available at an affordable cost.

A relatively small payload capacity is another limitation of an MUAV airframe, which restricts the size and weight of any sensors that can be carried. This often results in the necessity to carry each sensor on separate flights. In addition, the quality of the specialised sensors that are small and light enough to be carried by an MUAV can result in a poor signal to noise ratio, in particular multispectral and thermal infrared sensors. Presently, there is a limited market for this type of sensor, resulting in the technology being relatively immature.

Future research into UAV remote sensing will address some of the limitations that have been identified. New and improved airframes are being developed and coming onto the market at an ever increasing rate as the civilian use of UAVs rapidly grows. These new airframes are lighter and stronger, allowing them to carry more batteries and larger sensor payloads. For example, there are currently some airframes that claim to be able to carry a 7 kg payload for over 20 minutes. Another solution for mapping larger areas is to use a fixed wing airframe rather than a multi-rotor. A fixed wing platform can fly longer and faster, thus giving it greater coverage. Future research will look at verifying that the methodologies and data collection systems presented in this thesis are also applicable to data collected by a fixed wing platform. With fixed wing platforms, image overlap is generally less as a fixed wing airframe does not have the ability to fly very slowly (< 3 m/s) and issues such as image blur that is induced by a faster moving platform will need to be addressed.

It is hoped that the new commercial UAV industry, claiming to be able to assist with industries such as precision agriculture, will drive research into improved specialised sensors and robust image processing workflows. Specific sensors such as multispectral sensors will become more compact, have a higher resolution, and have an improved signal to noise ratio. Reduction of sensor noise is particularly important when trying to collect surface reflectance across a narrow range of wavelengths (essential for true plant health measurement) where the amount of light reaching the sensor is minimal and thus hard to measure with a “noisy” sensor. As new sensors become available, future research can look at their ability to quantify biophysical and biochemical variables in a similar manner to the methodology presented in Chapter 4.

Future research will look into further improving the direct georeferencing system (as described in Chapter 3) by replacing the single frequency DGPS with a dual frequency unit, thus improving the accuracy of the recorded camera positions (dual frequency accuracy is around 2 – 4 cm). This will in turn improve the spatial accuracy of the orthomosaics that can be produced without the need for the collection of GCPs. There are now commercially available systems (Applanix, 2015) that work in a similar fashion to the direct georeferencing system described in this thesis, in particular with a focus on fixed wing platforms. The direct georeferencing system could also be implemented on a fixed wing platform as a subject of further research. Finally, different flight path configurations could be tested for both fixed wing and VTOL aircraft to find which are the most efficient and accurate.

6.7 Final remarks

MUAVs are now proving to be a useful tool for environmental remote sensing to the scientific community. This thesis identified several key issues in the data processing workflow that can prevent an MUAV from being efficient and productive in practical applications. The new methods and techniques presented in this thesis address some of these issues, demonstrating that MUAVs, in particular, can be a powerful remote sensing tool. MUAVs are particularly suited for certain niche mapping tasks, such as very high resolution mapping of small areas that have complex terrains and/or vegetation that is too small to be accurately mapped via conventional means. The case study presented in Chapter 4 provides an example of the type of niche environmental remote sensing project for which MUAV are perfectly suited. Also, there are clearly other tasks for which UAVs are highly suited, such as precision agriculture, in particular, for smaller area, high value crops.

The technology in the area of UAV airframe and autopilot development is advancing and changing at a rapid rate. As civilian use increases, the market for specialised sensors will grow and so too will the quality of such sensors, further enhancing the utility for UAVs for environmental remote sensing.

References

Agisoft. (2012). "Agisoft Photoscan Professional." from http://www.agisoft.ru/products/photoscan/professional/.

Akca, D. (2013). "Photogrammetric Monitoring of an Artificially Generated Shallow Landslide." Photogrammetric Record **28**(142): 178-195.

Anderson, K. and K. J. Gaston (2013). "Lightweight unmanned aerial vehicles will revolutionize spatial ecology." Frontiers in Ecology and the Environment **11**(3): 138-146.

Applanix. (2015). "APX-15 UAV Direct georeferencing sensor." Retrieved 28/01/2015, from http://www.applanix.com/products/airborne/apx15uav.html.

Asner, G. P. (1998). "Biophysical and Biochemical Sources of Variability in Canopy Reflectance." Remote Sensing of Environment **64**(3): 234-253.

Astre, H. (2012). "SFM Toolkit." Retrieved 25/09/2012, 2012, from http://www.visual-experiments.com/demos/sfmtoolkit/.

Ayoub, F., S. LePrince and L. Keene (2009) "User's guide to COSI-Corr: Co-registration of O**p**tically sensed images and correlation." 38.

BAE_SYSTEMS. (2012). "SOCET SET." Retrieved 25/09/2012, 2012, from http://www.socetgxp.com/content/products/socet-set.

Barazzetti, L., F. Remondino and M. Scaioni (2010a). Automation in 3D reconstruction: results on different kinds of close-range blocks. International Archives of Photogrammetry, Remote Sensing and Spatial Information Sciences, Vol. XXXVIII, Part 5 Commission V Symposium, Newcastle upon Tyne, UK.

Barazzetti, L., F. Remondino, M. Scaioni and R. Brumana (2010b). Fully automatic UAV image-based sensor orientation. International Archives of Photogrammetry, Remote Sensing and Spatial Information Sciences, Vol. XXXVIII, Part 5 Commission V Symposium, Newcastle upon Tyne, UK.

Bell, R., H. Petschko, M. Rohrs and A. Dix (2012). "Assessment of Landslide Age, Landslide Persistence and Human Impact Using Airborne Laser Scanning Digital Terrain Models." Geografiska Annaler Series a-Physical Geography **94A**(1): 135-156.

Bendea, H., P. Boccardo, S. Dequal, F. Giulio Tondo, D. Marenchino and M. Piras (2008). Low Cost UAV for Post-Disaster Assessment. The International Archives of the Photogrammetry, Remote Sensing and Spatial Information Sciences, Beijing, China, IPRS.

Bendig, J., A. Bolten and G. Bareth (2012). Introducing a Low-Cost Mini-UAV for Thermal- and Multispectral-Imaging. International Archives of the Photogrammetry, Remote Sensing and Spatial Information Sciences. Melbourne, Australia, XXII ISPRS Congres. **XXXIX-B1**.

Berni, J., P. J. Zarco-Tejada, L. Suarez and E. Fereres (2009). "Thermal and Narrowband Multispectral Remote Sensing for Vegetation Monitoring From an Unmanned Aerial Vehicle." Ieee Transactions on Geoscience and Remote Sensing **47**(3): 722-738.

Besl, P. J. and N. D. McKay (1992). "A Method for Registration of 3-D Shapes." IEEE Transactions on Pattern Analysis and Machine Intelligence, **14**(2): 239-256.

Bláha, M., H. Eisenbeiss, D. Grimm and P. Limpach (2011). Direct Georeferencing of UAVs. UAV-g 2011, Conference on Unmanned Aerial Vehicle in Geomatics Zurich, Switzerland, International Archives of the Photogrammetry, Remote Sensing and Spatial Information Sciences.

Broge, N. H. and E. Leblanc (2000). "Comparing prediction power and stability of broadband and hyperspectral vegetation indices for estimation of green leaf area index and canopy chlorophyll density." Remote Sensing of Environment **76**: 156-172.

Bryson, M., M. Johnson-Roberson, R. J. Murphy and D. Bongiorno (2013). "Kite aerial photography for low-cost, ultra-high spatial resolution multi-spectral mapping of intertidal landscapes." PLoS One **8**(9): e73550.

Bryson, M., A. Reid, F. Ramos and S. Sukkarieh (2010). "Airborne Vision-Based Mapping and Classification of Large Farmland Environments." Journal of Field Robotics **27**(5): 632-655.

CalTech. (2011). "COSI-Corr: Co-registration of Optically Sensed Images and Correlation." Retrieved 30 November 2011, from www.tectonics.caltech.edu.

CASA (2014). Civil Aviation Safety Regulations 1998 - Part 101—Unmanned aircraft and rockets. CASA, Australian Government, Com Law. **2015**.

CASA. (2015). "Civial Aviation Safety Authority - List of UAS operator certificate holders." from http://www.casa.gov.au/scripts/nc.dll?WCMS:STANDARD::pc=PC_100959.

Chiang, K.-W., M.-L. Tsai and C.-H. Chu (2012). "The Development of an UAV Borne Direct Georeferenced Photogrammetric Platform for Ground Control Point Free Applications." Sensors **12**(12): 9161-9180.

Chou, T.-Y., M.-L. Yeh, Y.-C. Chen and Y.-H. Chen (2010). Disaster monitoring and management by the Unmanned Aerial Vehicle technology. ISPRS TC VII Symposium – 100 Years ISPRS, Vienna, Austria, IAPRS.

References

Clarke, L. J., S. A. Robinson, Q. Hua, D. J. Ayre and D. Fink (2012). "Radiocarbon bomb spike reveals biological effects of Antarctic climate change." Global Change Biology **18**(1): 301-310.

Colomina, I. and P. Molina (2014). "Unmanned aerial systems for photogrammetry and remote sensing: A review." ISPRS Journal of Photogrammetry and Remote Sensing **92**: 79-97.

Convey, P., R. Bindschadler, G. di Prisco, E. Fahrbach, J. Gutt, D. A. Hodgson, P. A. Mayewski, C. P. Summerhayes, J. Turner and A. Consortium (2009). "Antarctic climate change and the environment." Antarctic Science **21**(6): 541-563.

Crete, F., T. Dolmiere, P. Ladret and M. Nicolas (2007). The blur effect: perception and estimation with a new no-reference perceptual blur metric. Proceedings of the SPIE - Human Vision and Electronic Imaging XII., San Jose : États-Unis d'Amérique.

Dandois, J. P. and E. C. Ellis (2010). "Remote Sensing of Vegetation Structure Using Computer Vision." Remote Sensing **2**(4): 1157-1176.

Defence, U. D. o. (2008). Global Positioning System standard positioning service performance standard. D. o. Defence. Washington, USA, US Government.

Dewitte, O., J. C. Jasselette, Y. Cornet, M. Van Den Eeckhaut, A. Collignon, J. Poesen and A. Demoulin (2008). "Tracking landslide displacements by multi-temporal DTMs: A combined aerial stereophotogrammetric and LIDAR approach in western Belgium." Engineering Geology **99**(1-2): 11-22.

Digitalglobe. (2011). "DigitalGlobe Core Imagery Products Guide." Retrieved 13/01/2011, from http://www.digitalglobe.com/file.php/811/DigitalGlobe_Core_Imagery_Products_Guide.pdf.

Dunford, R., K. Michel, M. Gagnage, H. Piegay and M. L. Tremelo (2009). "Potential and constraints of Unmanned Aerial Vehicle technology for the characterization of Mediterranean riparian forest." International Journal of Remote Sensing **30**(19): 4915-4935.

Eisenbeiss, H. (2004). A Mini Unmanned Aerial Vehicle (UAV): System Overview and Image Acquisition. International Workshop on "PROCESSING AND VISUALIZATION USING HIGH-RESOLUTION IMAGERY". Pitsanulok, Thailand.

Eisenbeiss, H. (2009). UAV Photogrammetry. Doctor of Sciences, ETH ZURICH.

Eugster, H. and S. Nebiker (2007). Geo-Registration of video sequences capruted from mini UAVs – Approaches and accuracy assesment. Approaches and Accuracy Assessment, 5th International Symposium on Mobile Mapping Technology, Padua.

Everaerts, J. (2008). "The use of unmanned aerial vehicles (UAVs) for remote sensing and mapping." International Archives of the Photogrammetry, Remote Sensing and Spatial Information Sciences **37**: 1187-1192.

Fischler, M. A. and R. C. Bolles (1981). "Random Sample Consensus - a Paradigm for Model-Fitting with Applications to Image-Analysis and Automated Cartography." Communications of the Acm **24**(6): 381-395.

Furukawa, Y. and J. Ponce (2009). "Accurate, Dense, and Robust Multi-View Stereopsis." IEEE Trans. on Pattern Analysis and Machine Intelligence **32**(8): 1362-1376.

Girardeau-Montaut, D. (2012). "Cloud Compare v2.3." from http://www.danielgm.net/cc/.

Grenzdörffer, G. J., A. Engelb and B. Teichertc (2008). The Photogrammetric Potential of Low-Cost Uavs in Forestry and Agriculture. The International Archives of the Photogrammetry, Remote Sensing and Spatial Information Sciences, Beijing.

Haboudane, D., J. R. Miller, E. Pattey, P. J. Zarco-Tejada and I. B. Strachan (2004). "Hyperspectral vegetation indices and novel algorithms for predicting green LAI of crop canopies: Modeling and validation in the context of precision agriculture." Remote Sensing of Environment **90**(3): 337-352.

Hakala, T., J. Suomalainen and J. I. Peltoniemi (2010). "Acquisition of Bidirectional Reflectance Factor Dataset Using a Micro Unmanned Aerial Vehicle and a Consumer Camera." Remote Sensing **2**(3): 819-832.

Hardin, P. J. and R. R. Jensen (2011). "Small-Scale Unmanned Aerial Vehicles in Environmental Remote Sensing: Challenges and Opportunities." Giscience & Remote Sensing **48**(1): 99-111.

Harwin, S. and A. Lucieer (2012). "Assessing the Accuracy of Georeferenced Point Clouds Produced via Multi-View Stereopsis from Unmanned Aerial Vehicle (UAV) Imagery." Remote Sensing **4**(6): 1573-1599.

Horcher, A. and R. J. M. Visser (2004). Unmanned Aerial Vehicles: Applications for Natural Resource Management and Monitoring. Council on Forest Engineering (COFE) Conference Proceedings: “Machines and People, The Interface”, Arkansas, USA.

Hruska, R. C., G. D. Lancaster, J. L. Harbour and S. J. Cherry (2005). Small UAV-Acquired, High-Resolution, Georeferenced Still Imagery. Wildlife Society 12th Annual Conference.

Hu, S., C. Haiyang, C. Coopmans, H. Jinlu, M. McKee and C. YangQuan (2010). Low-cost UAV-based thermal infrared remote sensing: Platform, calibration and applications. Mechatronics and Embedded Systems and Applications (MESA), IEEE/ASME International Conference on Mechatronic and Embedded Systems and Applications.

References

Hunt, E. R., W. D. Hively, S. J. Fujikawa, D. S. Linden, C. S. T. Daughtry and G. W. McCarty (2010a). "Acquisition of NIR-Green-Blue Digital Photographs from Unmanned Aircraft for Crop Monitoring." Remote Sensing **2**(1): 290-305.

Hunt, E. R. J., W. D. Hively, C. S. T. Daughtry, G. W. McCarty, G. W. Fujikawa, T. L. Ng, M. Tranchitella, D. S. Linden and D. W. Yoel (2008). Remote Sensing of Crop Leaf Area Index using Umanned Airborne Vehicles. Pecora 17 – The Future of Land Imaging…Going Operational, Denver, Colorado.

Hunt, J., E. Raymond, W. D. Hively, S. J. Fujikawa, D. S. Linden, C. S. T. Daughtry and G. W. McCarty (2010b). "Acquisition of NIR-Green-Blue Digital Photographs from Unmanned Aircraft for Crop Monitoring." Remote Sensing **2**(1): 290-305.

Immerzeel, W. W., P. D. A. Kraaijenbrink, J. M. Shea, A. B. Shrestha, F. Pellicciotti, M. F. P. Bierkens and S. M. de Jong (2014). "High-resolution monitoring of Himalayan glacier dynamics using unmanned aerial vehicles." Remote Sensing of Environment **150**: 93-103.

Intergraph. (2012). "LPS." Retrieved 25/09/2012, 2012, from http://geospatial.intergraph.com/products/LPS/LPS/Details.aspx.

Isenburg, M. (2012). "LAStools: converting, filtering, viewing, gridding, and compressing LIDAR data." Retrieved 27th March, 2012, from http://www.cs.unc.edu/~isenburg/lastools/.

ITTVIS. (2011). "ENVI Software - Image Processing and Analysis Solutions." from http://www.ittvis.com/envi.

James, M. R. and S. Robson (2012). "Straightforward reconstruction of 3D surfaces and topography with a camera: Accuracy and geoscience application." Journal of Geophysical Research-Earth Surface **117**(F03017): 17.

Johnson, L. F., S. R. Herwitz, S. E. Dunagan, B. M. Lobitz, D. Sullivan and R. Slye (2003). Collection of Ultra High Spatial and Spectral Resolution Image Data over California Vineyards with a Small UAV. International Symposium on Remote Sensing of Environment, Honolulu, HI, USA.

Kaneko, T., T. Koyama, A. Yasuda, M. Takeo, T. Yanagisawa, K. Kajiwara and Y. Honda (2011). "Low-altitude remote sensing of volcanoes using an unmanned autonomous helicopter: an example of aeromagnetic observation at Izu-Oshima volcano, Japan." International Journal of Remote Sensing **32**(5): 1491-1504.

Kelcey, J. and A. Lucieer (2012). "Sensor Correction of a 6-Band Multispectral Imaging Sensor for UAV Remote Sensing." Remote Sensing **4**(5): 1462-1493.

Knoth, C., B. Klein, T. Prinz and T. Kleinebecker (2013). "Unmanned aerial vehicles as innovative remote sensing platforms for high-resolution infrared imagery

to support restoration monitoring in cut-over bogs." Applied Vegetation Science **16**(3): 509-517.

Kung, O., C. Strecha, A. Beyeler, J.-C. Zufferey, D. Floreano, P. Fua and F. Gervaix (2011). The accuracy of automatic photogrammetric techniques on ultra-light UAV imagery. Conference on Unmanned Aerial Vehicle in Geomatics. R. S. a. S. I. S. International Archives of the Photogrammetry. Zurich, Switzerland, UAV-g 2011. **XXXVIII-1/C22**.

Laliberte, A. S., M. A. Goforth, C. M. Steele and A. Rango (2011a). "Multispectral Remote Sensing from Unmanned Aircraft: Image Processing Workflows and Applications for Rangeland Environments." Remote Sensing **3**(11): 2529-2551.

Laliberte, A. S., J. E. Herrick, A. Rango and C. Winters (2010). "Acquisition , Orthorectification , and Object-based Classification of Unmanned Aerial Vehicle (UA V) Imagery for Rangeland Monitoring." Photogrammetric Engineering & Remote Sensing **76**: 661-672.

Laliberte, A. S. and A. Rango (2009). "Texture and scale in object-based analysis of subdecimeter resolution unmanned aerial vehicle (UAV) imagery." IEEE Transactions on Geoscience and Remote Sensing **47**(3): 1-10.

Laliberte, A. S. and A. Rango (2011). "Image Processing and Classification Procedures for Analysis of Sub-decimeter Imagery Acquired with an Unmanned Aircraft over Arid Rangelands." Giscience & Remote Sensing **48**(1): 4-23.

Laliberte, A. S., C. Winters and A. Rango (2008). A procedure for orthorectification of sub-decimeter Resolution Imagery Obtained with an Unmanned Aerial Vehicle (UAV). ASPRS 2008 Annual Conference. Portland, OR**:** 9.

Laliberte, A. S., C. Winters and A. Rango (2011b). "UAS remote sensing missions for rangeland applications." Geocarto International **26**(2): 141-156.

Lelong, C. C. D., P. Burger, G. Jubelin, B. Roux, S. Labbe and F. Baret (2008). "Assessment of Unmanned Aerial Vehicles Imagery for Quantitative Monitoring of Wheat Crop in Small Plots." Sensors **8**(5): 3557-3585.

Leprince, S. (2008). "Monitoring Earth Surface Dynamics With Optical Imagery." Eos, Transactions American Geophysical Union **89**(1): 1-2.

Leprince, S., S. Barbot, F. Ayoub and J. P. Ayouac (2007). "Automatic and precise orthorectification, co-registration, and sub-pixel correlation of satellite images, application to ground deformation measurements." IEEE Transactions on Geoscience and Remote Sensing **46**(6): 1529-1558.

libsift. (2012). "Fast SIFT Image Features Library." Retrieved 25/09/2012, 2012, from http://libsift.sourceforge.net/.

References

Lingua, A., D. Marenchino and F. Nex (2009). "Performance Analysis of the SIFT Operator for Automatic Feature Extraction and Matching in Photogrammetric Applications." Sensors (Basel) **9**(5): 3745-3766.

Lovelock, C. E. and S. A. Robinson (2002). "Surface reflectance properties of Antarctic moss and their relationship to plant species, pigment composition and photosynthetic function." Plant, Cell & Environment **25**(10): 1239-1250.

Lowe, D. (2005). "SIFT Keypoint Detector." from http://www.cs.ubc.ca/~lowe/keypoints/.

Lowe, D. G. (1999). Object recognition from local scale-invariant features. International Conference on Computer Vision. Corfu, Greece.

Lucieer, A., S. M. de Jong and D. Turner (2013). "Mapping landslide displacements using Structure from Motion (SfM) and image correlation of multi-temporal UAV photography." Progress in Physical Geography: 1-20.

Lucieer, A., S. Robinson and D. Turner (2011). Unmanned Aerial Vehicle (UAV) Remote Sensing for Hyperspatial Terrain Mapping of Antarctic Moss Beds based on Structure from Motion (SfM) point clouds. 34th International Symposium for Remote Sensing of the Environment (ISRSE), Sydney Australia.

Lucieer, A., D. Turner, D. H. King and S. A. Robinson (2014). "Using an Unmanned Aerial Vehicle (UAV) to capture micro-topography of Antarctic moss beds." International Journal of Applied Earth Observation and Geoinformation **27**(April): 53-62.

Luhmann, T., S. Robson, S. Kyle and I. Harley (2006). Close Range Photogrammetry, Whittles Publishing, Caithness, Scotland, UK.

Marchbank, M. (2009a). To Boldly go where no man can. Flight Safety Australia.

Marchbank, M. (2009b). UAS - the story continues. Flight Safety Australia.

Martha, T. R., N. Kerle, V. Jetten, C. J. van Westen and K. V. Kumar (2010). "Landslide Volumetric Analysis Using Cartosat-1-Derived DEMs." IEEE Geoscience and Remote Sensing Letters **7**(3): 582-586.

McIntosh, P. D., D. M. Price, R. Eberhard and A. J. Slee (2009). "Late Quaternary erosion events in lowland and mid-altitude Tasmania in relation to climate change and first human arrival." Quaternary Science Reviews **28**(9-10): 850-872.

Mikrokopter. (2011). "Mikrokopter Wiki." Retrieved 17/01/2011, 2011, from www.mikrokopter.com.

Nadim, F., O. Kjekstad, P. Peduzzi, C. Herold and C. Jaedicke (2006). "Global landslide and avalanche hotspots." Landslides **3**(2): 159-173.

Nagai, M., T. Chen, R. Shibasaki, H. Kumagai and A. Ahmed (2009). "UAV-Borne 3-D Mapping System by Multisensor Integration." IEEE Transactions on Geoscience and Remote Sensing **47**(3): 701-708.

Nagai, M., R. Shibasaki, D. Manandhar and H. Zhao (2004). Development of Digital Surface Model and Feature Extraction by Integrating Laser Scanner and CCD Sensor with IMU. ISPRS Congress, Geo-Imagery Bridging Continents, Istanbul, Turkey.

Nebiker, S., A. Annen, M. Scherrer and D. Oesch (2008). A Light-weight Multispectral Sensor for Micro UAV - Opportunities for very high resolution airborne remote sensing. The International Archives of the Photogrammetry, Remote Sensing and Spatial Information Sciences, Beijing.

Niethammer, U., S. Rothmund, M. R. James, J. Travelletti and M. Joswig (2010). UAV-Based Remote Sensing of Landslides. International Archives of Photogrammetry, Remote Sensing and Spatial Information Sciences, Commission V Symposium, Newcastle upon Tyne, UK.

Niethammer, U., S. Rothmund and M. Joswig (2009). UAV-based remote sensing of the slow-moving landslide Super-Sauze. Proceedings of the International Conference on Landslide Processes: from geomorpholgic mapping to dynamic modelling, Strasbourg, CERG Editions.

Niethammer, U., S. Rothmund, U. Schwaderer, J. Zeman and M. Joswig (2011). Open source image-processing tools for low-cost UAV-based landslide investigations. International Archives of the Photogrammetry, Remote Sensing and Spatial Information Sciences, Zurich, Switzerland.

Novatel. (2012). "GrafNav GNSS Post-Processing Software " Retrieved 12/9/2012, from http://www.novatel.com/products/software/waypoint-products/post-processing-software/grafnav.

Oleire-Oltmanns, S., I. Marzolff, K. Peter and J. Ries (2012). "Unmanned Aerial Vehicle (UAV) for Monitoring Soil Erosion in Morocco." Remote Sensing **4**(11): 3390-3416.

Pesci, A., G. Teza, G. Casula, F. Loddo, P. De Martino, M. Dolce, F. Obrizzo and F. Pingue (2011). "Multitemporal laser scanner-based observation of the Mt. Vesuvius crater: Characterization of overall geometry and recognition of landslide events." ISPRS Journal of Photogrammetry and Remote Sensing **66**(3): 327-336.

Pfeifer, N., P. Glira and C. Briese (2012). Direct georeferencing with on board navigation components of light weight UAV platforms. International Archives of the Photogrammetry, Remote Sensing and Spatial Information Sciences. Melbourne, Australia, XXII ISPRS Congres. **XXXIX-B7:** 487-492.

Pix4D. (2012). "Next-Generation Aerial Image Processing Software." Retrieved 14-09-2012, 2012, from http://pix4d.com/.

References

Ragg, H. and C. Fey (2013). UAS in the Mountains. GIM International. **27:** 3.

Rango, A., A. Laliberte, J. E. Herrick, C. Winters, K. Havstad, C. Steele and D. Browning (2009). "Unmanned aerial vehicle-based remote sensing for rangeland assessment, monitoring, and management." Journal of Applied Remote Sensing **3**(033542): 1-15.

Rango, A., A. Laliberte, C. Steele, J. E. Herrick, B. Bestelmeyer, T. Schmugge, A. Roanhorse and V. Jenkins (2006). "Using unmanned aerial vehicles for rangelands: current applications and future potentials." Environmental Practice **8**(3): 159-168.

Rango, A. and A. S. Laliberte (2010). "Impact of flight regulations on effective use of unmanned aircraft systems for natural resources applications." Journal of Applied Remote Sensing **4**: 043539-043512.

Remondino, F., L. Barazzetti, F. Nex, M. Scaioni and D. Sarazzi (2011). UAV photogrammetry for mapping and 3D modeling - current status and future perspectives. International Archives of the Photogrammetry, Remote Sensing and Spatial Information Sciences. Zurich, Switzerland. **XXXVIII-1/C22 UAV-g:** 6.

Robinson, S. A., J. Wasley and A. K. Tobin (2003). "Living on the edge–plants and global change in continental and maritime Antarctica." Global Change Biology **9**(12): 1681-1717.

Rosnell, T. and E. Honkavaara (2012). "Point cloud generation from aerial image data acquired by a quadrocopter type micro unmanned aerial vehicle and a digital still camera." Sensors (Basel) **12**(1): 453-480.

Rufino, G. and A. Moccia (2005). Integrated VIS-NIR Hyperspectral / Thermal-IR Electro-Optical Payload System for a Mini-UAV. AIAA 2005-7009, Arlington, Virginia, USA, American Institute of Aeronautics and Astronautics.

Sauerbier, M., E. Siegrist, H. Eisenbeiss and N. Demir (2011). The practical application of UAV-Based Photogrammetry under Economic Aspects. International Archives of the Photogrammetry, Remote Sensing and Spatial Information Sciences. Zurich, Switzerland. **XXXVIII-1/C22 UAV-g:** 6.

Scaioni, M., L. Barazzetti, R. Brumana, B. Cuca, F. Fassi and F. Prandi (2009). RC-Heli and Structure & Motion Techniques for the 3-D reconstruction of a Milan Dome Spire Proceedings of the 3rd ISPRS International Workshop 3D-ARCH 2009: "3D Virtual Reconstruction and Visualization of Complex Architectures" Trento, Italy.

Scaioni, M., L. Longoni, V. Melillo and M. Papini (2014). "Remote Sensing for Landslide Investigations: An Overview of Recent Achievements and Perspectives." Remote Sensing **6**(10): 9600-9652.

Schuster, R. L. (1996). Scoioeconomic significance of lanslides. Landslides - Investigation and Mitigation. A. K. Turner and R. L. Schuster. Washington D.C., National Research Council**:** 12-35.

Scopus. (2015). "Scopus - Document search." Retrieved 4th Feb 2014, 2015, from www.scopus.com.

Smith, G. M. and E. J. Milton (1999). "The use of the empirical line method to calibrate remotely sensed data to reflectance." International Journal of Remote Sensing **20**(13): 2653-2662.

Snavely, N. (2010). Bundler: Structure from Motion (SfM) for Unordered Image Collections.

Snavely, N., S. M. Seitz and R. Szeliski (2008). "Modeling the World from Internet Photo Collections." International Journal of Computer Vision **80**(2): 189-210.

Sugiura, R., N. Noguchi and K. Ishii (2005). "Remote-sensing Technology for Vegetation Monitoring using an Unmanned Helicopter." Biosystems Engineering **90**: 369-379.

Thrun, S., M. Diel and D. Hähnel (2003). Scan Alignment and 3-D Surface Modeling with a Helicopter Platform. The 4th International Conference on Field and Service Robotics.

Tsai, M. L., K. W. Chiang, Y. W. Huang, Y. S. Linb, J. S. Tsaib, C. F. Loc, Y. S. Linc and C. H. Wud (2010). The Development of a Direct Georeferencing Ready UAV based photogrammetry platform. Commission I, ICWG I/V Unmanned Vehicle Systems (UVS) for Mapping and Monitoring Applications.

Turner, D. and A. Lucieer (2013). Using a Micro Unmanned Aerial Vehicle (UAV) for Ultra High Resolution Mapping and Monitoring of Landslide Dynamics. IEEE International Geoscience and Remote Sensing Symposium. Melbourne, Australia.

Turner, D., A. Lucieer and S. M. de Jong (2015). "Time Series Analysis of Landslide Dynamics Using an Unmanned Aerial Vehicle (UAV)." Remote Sensing **7**(2): 1736-1757.

Turner, D., A. Lucieer, Z. Malenovský, D. King and S. Robinson (2014a). "Spatial Co-Registration of Ultra-High Resolution Visible, Multispectral and Thermal Images Acquired with a Micro-UAV over Antarctic Moss Beds." Remote Sensing **6**(5): 4003-4024.

Turner, D., A. Lucieer and L. Wallace (2014b). "Direct Georeferencing of Ultrahigh-Resolution UAV Imagery." IEEE Transactions on Geoscience and Remote Sensing **52**(5): 2738-2745.

Turner, D., A. Lucieer and C. Watson (2012). "An Automated Technique for Generating Georectified Mosaics from Ultra-High Resolution Unmanned

Aerial Vehicle (UAV) Imagery, Based on Structure from Motion (SfM) Point Clouds." Remote Sensing **4**(12): 1392-1410.

Verhoeven, G. (2011). "Taking computer vision aloft - archaeological three-dimensional reconstructions from aerial photographs with photoscan." Archaeological Prospection **18**(1): 67-73.

Verhoeven, G., M. Doneus, C. Briese and F. Vermeulen (2012). "Mapping by matching: a computer vision-based approach to fast and accurate georeferencing of archaeological aerial photographs." Journal of Archaeological Science **39**(7): 2060-2070.

Walter, M., U. Niethammer, S. Rothmund and M. Joswig (2009). "Joint analysis of the Super-Sauze (French Alps) mudslide by nanoseismic monitoring and UAV-based remote sensing." First Break **27**(August): 8.

Wasley, J., S. A. Robinson, J. D. Turnbull, D. H. King, W. Wanek and M. Popp (2012). "Bryophyte species composition over moisture gradients in the Windmill Islands, East Antarctica: development of a baseline for monitoring climate change impacts." Biodiversity **1**(13): 257-264.

Watts, A. C., V. G. Ambrosia and E. A. Hinkley (2012). "Unmanned Aircraft Systems in Remote Sensing and Scientific Research: Classification and Considerations of Use." Remote Sensing **4**(6): 1671-1692.

Westoby, M. J., J. Brasington, N. F. Glasser, M. J. Hambrey and J. M. Reynolds (2012). "'Structure-from-Motion' photogrammetry: A low-cost, effective tool for geoscience applications." Geomorphology **179**(0): 300-314.

Wilson, R. (2010). Manning UAS. Flight Safety Australia. **May-Jun:** 2.

Wischounig-Strucl, D. and B. Rinner (2010). Resource-Aware Image Mosaicking on Networks of Small-Scale UAVs. ICDSC 2010, Atlanta, GA, USA.

Wolf, P. R. and B. A. Dewitt (2000). Elements of Photogrammetry with Applications in GIS, McGraw-Hill.

Wong, K. C. (2001). "Survey of Regional Developments : Civil Applications." from http://www.aeromech.usyd.edu.au/wwwuav/papers/UAV_civil_app.PDF.

Wong, K. C. and C. Bil. (2006). "UAVs over Australia - Market And Capabilities." from http://www.aeromech.usyd.edu.au/wwwdocs/uavs_over_australia_0398.pdf.

Wu, C. (2012). "VisualSFM : A Visual Structure from Motion System." Retrieved 25/09/2012, 2012, from http://homes.cs.washington.edu/~ccwu/vsfm/.

Yamaguchi, Y., A. B. Kahle, H. Tsu, T. Kawakami and M. Pniel (1998). "Overview of Advanced Spaceborne Thermal Emission and Reflection Radiometer (ASTER)." IEEE Transactions on Geoscience and Remote Sensing. **36**(4): 1062-1071.

Zarco-Tejada, P. J., M. L. Guillén-Climent, R. Hernández-Clemente, A. Catalina, M. R. González and P. Martín (2013). "Estimating leaf carotenoid content in vineyards using high resolution hyperspectral imagery acquired from an unmanned aerial vehicle (UAV)." Agricultural and Forest Meteorology **171–172**(2013): 281– 294.

Zhang, Y., J. Xiong and L. Hao (2011). "Photogrammetric processing of low-altitude images acquired by Unpiloted Aerial Vehicles." The Photogrammetric Record **26**(134): 190-211.

Zhou, G., V. Ambrosia, A. J. Gasiewski and G. Bland (2009). "Foreword to the Special Issue on Unmanned Airborne Vehicle (UAV) Sensing Systems for Earth Observations." IEEE Transactions on Geoscience and Remote Sensing **47**(3): 687-689.